Dynamics and performance optimization of spin-torque switching in magnetic tunnel junctions

A THESIS
SUBMITTED TO THE FACULTY OF THE GRADUATE SCHOOL
OF THE UNIVERSITY OF MINNESOTA
BY

Thomas Edward Dunn

IN PARTIAL FULFILLMENT OF THE REQUIREMENTS
FOR THE DEGREE OF
DOCTOR OF PHILOSOPHY

Alex Kamenev

October, 2013

Acknowledgments

This research would not have been possible without the support and help of my advisor, Alex Kamenev. In my years working with him, Alex has given me guidance when I needed it and the freedom to pursue my research wherever it took me. To this end he has shown remarkable patience with me. When I think of the path it took for me to get to this point, I find myself astonished that I was lucky enough to have an advisor of his caliber.

I would also like to acknowledge and thank the University of Minnesota and the Physics Department for accepting me and supporting me through my years as a teaching assistant and research assistant.

There have been many fellow graduate students who have helped me over the years. Specifically, I would like to thank Michael Albright, JJ Nelson, and Matt Parker for their friendship and their willingness to listen to me ramble on about my research when I needed a sounding board to bounce an idea or result off of.

Lastly I would like to thank my friends and family for their love and support. I could not have made it to graduate school, let alone finish, without them. They have all helped me in ways far too numerous to list. I am eternally grateful for having them in my life.

Dedication

For my mother and father for always loving and encouraging me, and for the ten-year-old kid who thought it would be cool to get a Ph.D.

Abstract

Spin-torque induced switching of the free layer in magnetic tunnel junctions has been a subject of significant research over the last decade. This focus is due to its potential as a universal non-volatile memory element. Much of early spin-torque research focused on understanding and quantifying the underlying mechanism of the switching process. More recent research, however, has focused on optimizing and integrating spin-torque based memory and logical elements into practical devices. While this research has shown promising results, significant reductions in switching times and energy costs are needed before such devices are competitive with existing commercial products.

For MTJs with pinned layer and free layer easy-axes parallel to one another, the most efficient prescription has been shown both theoretically and experimentally to be a DC current pulse roughly twice the critical current. Recent experimental research, however, has shown MTJs with a second pinned layer — polarized perpendicular to the free layer easy-axis, along the free layer easy-plane axis — can produce switching much faster and more efficiently than similar co-linear devices. These devices take advantage of the large initial angle between the free layer magnetization and the magnetization of the perpendicular polarizer to produce a spin-torque orders of magnitude larger than that of the parallel polarizing layer alone.

Unlike parallel spin-torque MTJs, where switching speed and efficiency is controlled by the magnetic damping acting on the free layer, perpendicular MTJs are limited by the GHz precessional frequency of the free layer magnetization about the effective field. This precession causes the perpendicular spin-torque to self-cancel for currents below a certain critical threshold, which greatly inhibits switching. This limitation can be overcome by applying an AC spin-current with frequency near the free layer precessional frequency, producing a resonant response in the free layer magnetization. Such AC strategies have been shown theoretically to significantly reduce the switching energy and critical current for certain device geometries, e.g. free layers with strong easy-plane anisotropy. However, this improvement comes at the cost of longer switching times.

For MTJs with weak easy-plane anisotropy, purely AC spin-current methods are ineffective, requiring currents well above the DC critical current to produce switching.

This is a result of the magnetization spending more time at large azimuthal angles through the switching process, where the spin-torque from the perpendicular pinned layer is weak. In contrast, as the magnetization spends more time at large azimuthal angles, the strength of the spin-torque from the parallel pinned layer gets larger when DC currents are used. For some cases the strengths of the AC and DC ST may intersect, allowing the AC ST to dominate for low energy orbits and the DC ST for high energy orbits. For these devices, switching may be optimized by applying an initial AC spin-current immediately followed by a DC current pulse.

In this thesis I present a theoretical description for spin-torque switching using AC and DC spin-currents. This description builds from the standard Landau-Lifshitz-Gilbert equation with Slonczewski spin-torque. By exploiting a separation in time-scales between the fast precessional motion of the free layer magnetization about the effective field and the slow drift of the free layer towards higher or lower energies that results from ST and damping, I reduce the free layer switching dynamics to that of a one dimensional system. Using this description I characterize certain current and frequency values important to switching, such as the DC critical current and the AC upper bifurcation frequency. Finally, using this description I show how to optimize the efficiency of AC, DC, and combination AC/DC spin-current strategies to minimize the Joule heat loss associated with switching. This leads to a well-defined range of spin-current polarization and free layer anisotropy values where each spin-current strategy is optimal.

Contents

Acknowledgments **i**

Dedication **ii**

Abstract **iii**

List of Tables **viii**

List of Figures **ix**

1 Introduction **1**

2 Model **5**

2.1 Introduction 5

2.2 Conservative Landau-Lifshitz torque: $\mathbf{\Gamma}_{\mathrm{LL}}$ 6

2.3 Dissipative Gilbert damping torque: $\mathbf{\Gamma}_{\mathrm{GD}}$ 8

2.4 Slonczewski spin-torque: $\mathbf{\Gamma}_{\mathrm{ST}}$ 10

2.5 Stochastic dynamics 11

2.6 Numerical simulations 13

3 DC spin-torque **15**

3.1 Introduction 15

3.2 Numerical simulations of DC switching 16

3.3 Theoretical description: energy/angle coordinates 21

3.4 Theoretical description: time-scale separation 24

3.4.1 φ-averaged energy dynamics 25

3.4.2 Equilibrium condition and critical current 26
3.4.3 Switching time 29
3.5 Joule heat minimization 30
3.5.1 Optimal DC spin-current protocol: analytic 31
3.5.2 Practical solutions 34
3.6 DC switching with easy-plane polarized spin-currents 37

4 AC spin-torque **41**
4.1 Introduction 41
4.2 Numerical simulations of AC ST 42
4.2.1 Free layer response: non-switching events 43
4.2.2 AC ST switching 46
4.3 Theoretical description: energy/angle coordinates 50
4.4 Theoretical description: φ-averaged equations of motion 51
4.4.1 Critical frequency 54
4.4.2 Critical current 59
4.5 Joule heat minimization 60
4.5.1 Optimal AC spin-current protocol: analytic 61
4.5.2 Practical solutions 64

5 AC/DC spin-torque **66**
5.1 Introduction 66
5.2 Numerical simulations of AC/DC ST 67
5.3 Joule heat minimization 70
5.3.1 Optimal AC/DC spin-current protocol: analytic 72
5.3.2 Practical solutions 74

6 Discussion **78**
6.1 Optimization 79
6.2 Effects of thermal noise during switching 80
6.3 Limitations on φ-averaging technique 81

7 Conclusion **86**

References **88**

Appendix A LLGS equation **97**

A.1 Energy equation 97

A.2 Conservation of M_s 97

A.3 Landau-Lifshitz damping 98

Appendix B Energy/angle equations **99**

B.1 Full equations 99

B.2 Approximations 101

B.3 Upper and lower critical current 103

Appendix C Glossary and acronyms **104**

C.1 Glossary 104

C.2 Acronyms 106

List of Tables

C.1 Acronyms 106

List of Figures

1.1 Schematic diagram of a magnetic tunnel junction. 2

2.1 Several Stoner-Wohlfarth orbits for a free layer with uniaxial anisotropy and a free layer with strong easy-plane anisotropy. 7

2.2 Relaxation trajectory of the magnetization for a free layer under the effects of Gilbert damping and the conservative LL torque. 9

2.3 Relaxation trajectory for the magnetization of a free layer under the effects of Gilbert damping, the conservative LL torque, and stochastic thermal noise. 12

3.1 Cartoon of a collinearly configured MTJ and a perpendicularly configured MTJ. 16

3.2 Several switching trajectories for collinear MTJ. 17

3.3 Several switching trajectories for MTJ with canted pinned layer 18

3.4 Several switching trajectories for perpendicular MTJ 19

3.5 Generalized ST energy force $V(E, \varphi)$ vs. energy for free layer with uniaxial anisotropy. 23

3.6 Generalized ST energy force $V(E, \varphi)$ vs. energy for free layer with strong easy-plane anisotropy. 24

3.7 Free layer energy $E(t)$ vs. time under the effect of a DC spin-current. . . 26

3.8 $\dot{E}$ vs. energy for various strengths of $\overline{\mathcal{I}}_{\mathrm{s}}$ for a free layer with strong easy-plane anisotropy 27

3.9 Local critical spin-current as a function of energy for a free layer with uniaxial anisotropy and a free layer with strong easy-plane anisotropy . 28

3.10 Critical current $\overline{\mathcal{I}}_{\mathrm{c}}$ as a function of $h = H_{\mathrm{z}}/H_{\mathrm{x}}$ 29

3.11 Minimum JHL in arbitrary units vs. H_{z}. 34

3.12 Simulated JHL vs. spin-current strength for various confidence levels p. 36
3.13 Optimal switching time as a function of switching confidence level, p. . . 37
3.14 Switching probability as a function of spin-current strength and inverse pulse time for free layers with various anisotropy configurations and spin-current polarizations. 38
3.15 JHL as a function of spin-current strength for free layers with various anisotropy configurations and spin-current polarizations. 39
3.16 Pulse times corresponding to the optimal JHL values shown in Fig. 3.15 as a function of spin-current strength. 40
4.1 Simulated optimal Joule heat lost as a function of spin-current strength for DC and AC spin-current methods. 43
4.2 Free layer energy vs. time under the influence of several AC spin-currents. 44
4.3 Free layer energy vs. time under the effect of AC spin-currents for three different AC frequencies 46
4.4 Switching probability of perpendicular MTJ as a function of AC spin-current amplitude and applied frequency. 47
4.5 Composite switching probability created by overlaying the highest switching probabilities in Fig. 4.4. 49
4.6 Switching probability as a function of pulse time for an AC spin-current. 50
4.7 Generalized φ-averaged ST energy and phase forces, $\widetilde{V}$ and $\widetilde{W}$, as functions of energy. 52
4.8 Free layer energy vs. phase under the effect of an AC spin-current. . . . 53
4.9 Free layer energy vs. phase under the effect of an AC spin-current along with $\mathcal{H} = 0$ trajectory. 55
4.10 Several contours of constant $\mathcal{H}$ for free layer under the effect of an AC spin-current. 56
4.11 Equilibrium energy as a function of AC spin-current frequency. 57
4.12 Switching probability as a function of spin-current strength and driving frequency along with critical frequency. 59
4.13 Switching probability as a function of spin-current strength and driving frequency along with critical frequency and AC critical current. 60

4.14 AC local critical current $\widetilde{\mathcal{I}}_{\mathrm{c}}(E)$ associated with the optimal AC frequency $\omega_{\mathrm{opt}} = \Omega(E)$ as a function of free layer energy. 63
5.1 Free layer energy as a function of time for DC , AC , and AC/DC spin-current pulses. 68
5.2 Optimal JHL as a function of spin-current amplitude $\mathcal{I}_{\mathrm{s}}$ for DC and AC/DC spin-current strategies. 69
5.3 Calculated spin-current efficiency as a function of energy for an AC spin-current and a DC spin-current. 73
5.4 Free layer energy E_{c} where the spin-current should be changed from AC to DC in order to minimize the JHL as a function of free layer relative anisotropy and the spin-current polarization. 74
5.5 Optimal JHL vs. spin-current strength $\mathcal{I}_{\mathrm{s}}$ for DC and AC/DC spin-current strategies. 75
5.6 Simulated AC and DC pulse times vs. spin-current strength $\mathcal{I}_{\mathrm{s}}$ which correspond to the optimal JHL in Fig. 5.5. 76
6.1 First order correction to energy trajectory, E_1, as a function of energy for free layers under the effect of DC spin-currents. 84
6.2 First order correction to energy trajectory, E_1, as a function of energy for free layers under the effect of AC spin-currents. 85

Chapter 1

Introduction

Over the last quarter century, the field of spintronics, where the electron spin degree of freedom is used to manipulate and probe ferromagnetic structures, has exploded from a field of novel academic research to a billion-dollar industry and the backbone of today's non-volatile data storage industry. It has even garnered a Nobel Prize for one of its earliest discoveries, giant magnetoresistance (GMR), which was awarded to Albert Fert [1] and Peter Grünberg [2]. One of the most recent advancements in the field of spintronics to show promise in practical applications is that of spin-transfer torque where spin-polarized currents are used to manipulate the magnetic moments of ferromagnetic structures.

First proposed in 1996 by both Slonczewski [3] and Berger [4], spin-transfer torque (STT), or spin-torque (ST), occurs when a current of spin-polarized electrons travels through a ferromagnetic material and deposits angular momentum via an exchange interaction with the ferromagnet's macroscopic magnetization. Due to the conservation of the total angular momentum in this interaction, the net change in the angular momentum of the current flowing through the ferromagnetic layer must be equal and opposite to the net change in angular momentum of the ferromagnetic layer. Since angular momentum is proportional to magnetization, with a conversion factor given by the gyromagnetic ratio, γ, the absorption of the angular momentum results in a change in the magnetization direction of the ferromagnet, i.e., a torque on the ferromagnet. The existence of ST was confirmed experimentally shortly after Slonczewski and Berger's proposals [5, 6].

Since its experimental confirmation, the study of ST has grown into a thriving field of both experimental [7, 8, 9, 10, 11, 12] and theoretical research [13, 14, 15, 16, 17, 18, 19]. Over the last decade ST has shown tremendous practical potential as a data storage technology via its ability to quickly read and write information into high density, non-volatile memory structures by reversing the orientation of magnetic bits. It has also shown promise in its ability to drive magnetic spin-torque oscillators (STO) at GHz frequencies with narrow linewidths, which has a variety of uses [20, 21, 22, 23, 24, 25, 26, 27], as well as its ability to move magnetic domain walls, which may have uses in magnetic data storage and logic devices [28, 29, 30, 31, 32, 33, 34].

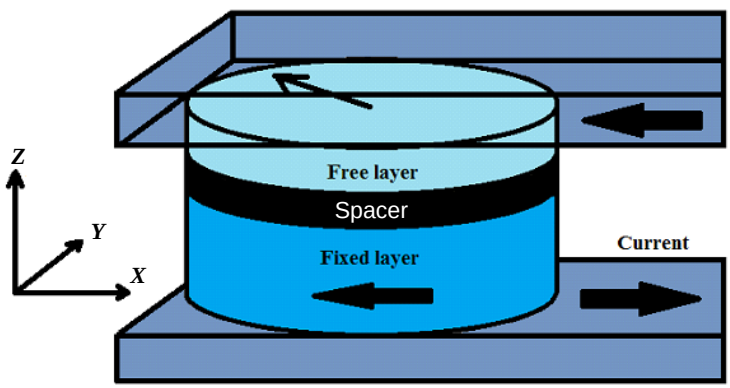

Figure 1.1: Schematic diagram of a magnetic tunnel junction (MTJ). Electrons run clockwise through the device, first passing through the bottom "fixed" layer where they become partially polarized in the $-\hat{\mathbf{e}}_x$-direction. They then pass through the "free" layer, where they impart some angular momentum. The MTJ has its easy-axis along the $\hat{\mathbf{e}}_x$-axis with the easy-plane normal to the $\hat{\mathbf{e}}_z$-axis.

For data storage applications, ST is applied to magnetic nano-structures known as magnetic tunnel junctions (MTJs). These MTJs typically consist of two thin magnetic layers and one non-magnetic layer (e.g., a tunneling-transparent insulator or a metal) that are sandwiched in a pillar between two ohmic contacts, Fig. 1.1. The two ferromagnetic layers, hereafter referred to as the "free" and the "fixed" layers, differ significantly

in their coercive fields, with the fixed layer being pinned along its preferred orientation much more strongly than the free layer. The higher coercivity in the fixed layer can be achieved through a number of means, such as increasing the thickness [35, 36], annealing to an adjacent antiferromagnetic layer [37], picking a harder magnetic material [38, 39], or using a synthetic antiferromagnet (SAF) structure where two adjacent ferromagnets are aligned opposite one another via strong RKKY coupling [40, 41].

When an electric current, with electrons flowing in the $\hat{\mathbf{e}}_z$-direction, passes through the fixed layer in Fig. 1.1, it becomes spin-polarized along the direction of the fixed layer's magnetization [42, 43, 44]. When this transmitted spin-current encounters the free layer it induces a ST on the free layer which tries to align the free and fixed layers' magnetizations. Alternatively, by applying an electric current in the opposite direction, i.e., with electrons flowing in the -$\hat{\mathbf{e}}_z$-direction, the direction of this ST can is reverse. Here the electrons reflected off the insulating barrier, which have a net spin-polarization opposite the direction of the fixed layer's magnetization, induce the ST on the free layer. This ST tries to anti-align the free and fixed layers' magnetization [45, 18]. These applications of ST allow for a number of dynamic regimes.

One such regime involves using ST to switch the orientation of the free layer in a MTJ from one stable state to another. This use of ST was confirmed shortly after its theoretical prediction [46, 47] with much of the early research focusing on understanding the effects of internal anisotropy [48, 49], temperature [50, 51, 52], and spin-current strength [53, 54] on the switching dynamics. With the development of high tunneling magnetoresistance MTJs [55] that have switching times in the sub-nanosecond regime [56, 57], ST memory has become a very attractive candidate for universal non-volatile memory. While development of ST memory has moved forward, recent research has also focused on more exotic switching strategies [58, 59]. Some of these strategies include using high-frequency AC spin-currents to excite resonant spin modes to assist the switching process [60, 61], as well as using spin-current polarized perpendicular to the interface to increase energy efficiency and reduce switching times [62, 63, 64].

Much of the research into these novel switching current strategies has focussed on experimental and micromagnetic simulations [65]. While these works have shown such strategies may improve switching efficiency for AC pulses and other exotic strategies,

a simple theoretical model for describing under what conditions these methods outperform their more generic counterparts has been lacking. In this thesis I present such a theoretical model. This model is used to optimize the switching efficiency of MTJs with arbitrary easy-plane and easy-axis anisotropy using purely DC and purely AC current pulses, as well as currents consisting of an initial AC pulse followed immediately by a DC pulse.

The structure of this thesis is as follows. In chapter 2 I present a macromagnetic model used to describe the dynamics of the free layer's magnetization throughout this thesis. This model serves as the underpinning for both the theoretical methods used as well as the numerical simulations shown thereafter. In chapter 3 I discuss switching using DC spin-currents for MTJs with various free layer anisotropy and spin-current polarizations. A time-scale separation and averaging technique is employed to reduce the switching behavior to a one-dimensional description for the time evolution of the free layer energy. This is then used to determine the optimal DC spin-current protocols for inducing switching in MTJ with arbitrary anisotropy and spin-polarization. In chapter 4 I discuss switching using AC spin-currents. Employing a time-scale separation and averaging technique similar to the one presented in chapter 3 for DC spin-currents, the free layer motion is reduced to a two-dimensional phase-space evolution for the free layer energy and the relative phase between the free layer and the AC signal. Using this description, spin-current strategies that minimize the switching energy are discussed and calculated for MTJs of arbitrary anisotropy and spin-polarization. In chapter 5 the AC and DC spin-current strategies discussed in the previous two chapters are combined to optimize switching strategies where an AC spin-current is used to excite a resonant response in the free layer, followed immediately by a DC current pulse that switches the free layer the rest of the way. Finally, in chapter 6 I discuss the results from chapters 3, 4, and 5, including the limitations of the averaging techniques used, and how one might incorporate the effects of thermal fluctuations into the theoretical description shown.

Chapter 2

Model

2.1 Introduction

In this chapter I review the dynamics of magnetic thin films via a macromagnetic formalism. In other words, the free layer is treated as a single magnetic domain with uniform magnetization $\mathbf{M}$ characterized by the saturation magnetization M_{s} and unit vector of the magnetization $\mathbf{m}$ such that $\mathbf{M} = M_{\mathrm{s}}\mathbf{m}$. The model presented here forms the basis for both the numerical simulations performed throughout this thesis and the theoretical proceedings which are covered in the following chapters. The full dynamics of the free layer presented here is broken up into four parts. Sections 2.2, 2.3, and 2.4 cover the deterministic dynamics of the free layer, which is governed by three torques

$$\dot{\mathbf{M}} = \mathbf{\Gamma}_{\mathrm{LL}} + \mathbf{\Gamma}_{\mathrm{GD}} + \mathbf{\Gamma}_{\mathrm{ST}} \,. \tag{2.1}$$

These represent, respectively, the conservative Landau-Lifshitz torque, the dissipative Gilbert damping torque, and the Slonczewski spin-torque terms. In Sec. 2.5 I discuss the effects of noise coming from thermal fluctuations and non-equilibrium sources. Finally, in Sec. 2.6 I provide a brief description of the various numerical simulation methods used.

2.2 Conservative Landau-Lifshitz torque: $\mathbf{\Gamma}_{\mathrm{LL}}$

For a single spin particle described by the Heisenberg spin operator $\mathbf{S}$ in an external magnetic field $\mathbf{H}_{\mathrm{ext}}$, the exchange Hamiltonian is given by the Zeeman energy

$$\mathcal{H}_{\mathrm{ex}} = -\frac{g\mu_{\mathrm{B}}}{\hbar}\mathbf{H}_{\mathrm{ext}} \cdot \mathbf{S}\,, \tag{2.2}$$

where μ_{B} is the Bohr magneton and g is the appropriate dimensionless g-factor for the particle. The time evolution of $\mathbf{S}$ is given by the Heisenberg equation of motion

$$\frac{\partial \mathbf{S}}{\partial t} = \frac{i}{\hbar}\left[\mathcal{H}_{\mathrm{ex}}, \mathbf{S}\right]\,. \tag{2.3}$$

Using the single spin commutation relation $\left[\mathbf{S}^i, \mathbf{S}^k\right] = i\,\hbar\,\epsilon^{ijk}\mathbf{S}^k_\alpha$, where i, j, and k are the Cartesian indices and ϵ^{ijk} is the Levi-Civita permutation tensor, this reduces to

$$\frac{\partial \mathbf{S}}{\partial t} = \mathbf{S} \times \mathbf{H}_{\mathrm{ext}}\,. \tag{2.4}$$

From Eqn. (2.4) it is clear the magnitude of the spin is conserved ($\mathbf{S} \cdot \dot{\mathbf{S}} = 0$) thus the spin precesses about the external field at a fixed angle from the external field direction.

For a magnetic material with magnetic moment $\mathbf{M}$, related to the average spin density per unit volume $\mathbf{M} = \frac{g\mu_{\mathrm{B}}}{\hbar}\langle\mathbf{S}\rangle$, this dynamic was first proposed by Landau and Lifshitz [66] as

$$\dot{\mathbf{M}} = \mathbf{\Gamma}_{\mathrm{LL}} = -\gamma\mathbf{M} \times \mathbf{H}_{\mathrm{eff}}\,, \tag{2.5}$$

hereafter known as the Landau-Lifshitz (LL) torque. Here γ is the gyromagnetic ratio and $\mathbf{H}_{\mathrm{eff}}$ is the effective magnetic field given by the gradient of the magnetic energy density $E(\mathbf{M})$ with respect to the magnetization,

$$\mathbf{H}_{\mathrm{eff}} = -\nabla_{\mathbf{M}} E(\mathbf{M})\,. \tag{2.6}$$

That $\mathbf{H}_{\mathrm{eff}}$ comes from the energy gradient means the motion of the magnetization described by Eqn. (2.5) preserves the energy of the free layer (or a detailed derivation see appendix A.2). This means under the effect of the LL torque the magnetization $\mathbf{M}$ travels along closed contours of constant energy known as StonerWohlfarth (SW) orbits. Figure 2.1 shows several SW orbits for two different anisotropy configurations.

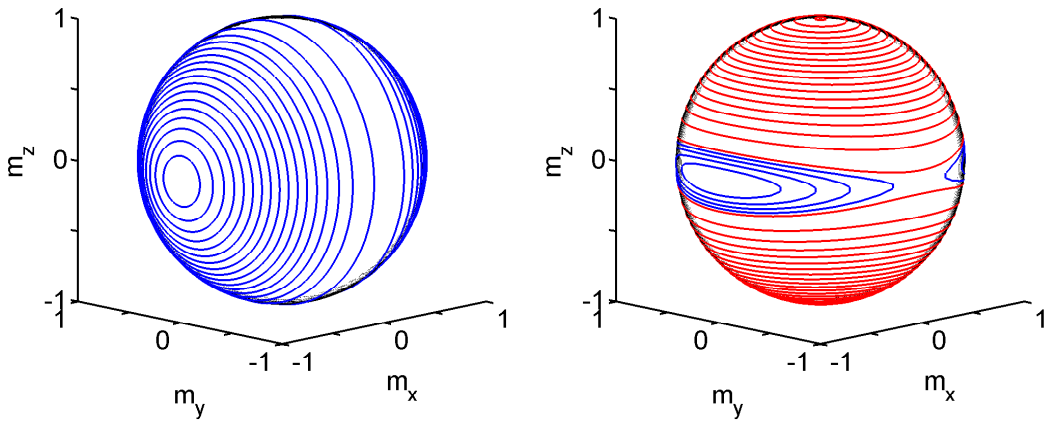

Figure 2.1: Several SW orbits for free layers with uniaxial anisotropy, $H_\mathrm{x} = 0.5M_\mathrm{s}$ (left), and strong easy-plane anisotropy, $H_\mathrm{x} = 0.033M_\mathrm{s}$ and $H_\mathrm{z} = M_\mathrm{s}$ (right). For both, $\mathbf{H}_\mathrm{ext} = 0$. Blue contours represent low energy orbits($E < E_\mathrm{b}$) and red contours represent high energy orbits ($E > E_\mathrm{b}$).

The energy density for the free layer in a MTJ can be written in terms of two shape anisotropy energy terms and the Zeeman energy from an applied external field:

$$E(\mathbf{m}) = \frac{M_\mathrm{s}}{2}\left[H_\mathrm{x}\left(1-(\mathbf{m}\cdot\hat{\mathbf{e}}_\mathrm{x})^2\right) + H_\mathrm{z}\left(\mathbf{m}\cdot\hat{\mathbf{e}}_\mathrm{z}\right)^2 - \mathbf{H}_\mathrm{ext}\cdot\mathbf{m}\right]. \tag{2.7}$$

Here $\mathbf{H}_\mathrm{ext}$ is the applied external field, H_x is the strength of the easy-axis anisotropy (chosen in the $\hat{\mathbf{e}}_\mathrm{x}$ direction), and H_z is the strength of the easy-plane anisotropy field (chosen along the $\hat{\mathbf{e}}_\mathrm{z}$ direction). These two shape anisotropy fields typically include contributions from the crystalline anisotropy, which comes from the crystal structure of the magnetic material used in the free layer, as well as anisotropy from the demagnetization field. Appendix A.1 shows how to construct H_x and H_z from these two contributions. The relative strengths of H_x and H_z can very greatly and depend on the material used and the shape of the free layer. The examples shown in Fig. 2.1 represent two of the limiting cases which will be used as examples throughout this thesis, namely a free layer with uniaxial anisotropy and one with strong easy-plane anisotropy. For simplicity, E is referred to as the energy for the remainder of this thesis.

The easy-axis anisotropy field in Eqn. (2.7) gives rise to two low-energy valleys, illustrated in Fig. 2.1 as regions with blue SW orbits. These valleys are separated by an energy barrier with height $E_{\mathrm{b}} = H_{\mathrm{x}} M_{\mathrm{s}}/2$. The minima of these valleys determine the orientation of the two stable states for the magnetization. For free layers with easy-plane anisotropy, these valleys are accompanied by two high-energy hills, illustrated in Fig. 2.1 as regions with red SW orbits. External fields $\mathbf{H}_{\mathrm{ext}}$ are sometimes used to force the magnetization to align in a specific direction or to allow one of the energy minima to be lower than the other [53]. This balance can also be accomplished by using a SAF with appropriately sized pinned and reference layers such that their respective dipole fields cancel at the free layer [46]. As a result, the external field will be set equal to zero ($\mathbf{H}_{\mathrm{eff}} = 0$) in the examples shown throughout this thesis. The theoretical mechanisms developed can still be easily applied to systems with applied external fields.

2.3 Dissipative Gilbert damping torque: $\mathbf{\Gamma}_{\mathrm{GD}}$

It has long been observed experimentally, for instance in hysteresis curve measurements, that applying a sufficiently strong magnetic field to a magnetic material causes the magnetization to saturate along the direction of the applied field. This is contrary to the simple precessional motion described by the LL torque in Eqn. (2.5), which conserves the energy of the magnetization, and indicates the presence of dissipation in the dynamics of the magnetization. Many mechanisms have been predicted theoretically to contribute to this observed damping, such as magnon-induced currents [67], magnon-magnon scattering [68, 69], spin-orbit coupling [70], and spin-shot noise [71, 72]. The simplest phenomenological way to incorporate these effects into the magnetization dynamics was suggested by Gilbert [73]:

$$\mathbf{\Gamma}_{\mathrm{GD}} = \frac{\alpha}{M_{\mathrm{s}}} \left[\mathbf{M} \times \dot{\mathbf{M}}\right]. \tag{2.8}$$

This Gilbert damping (GD) torque term in the equation of motion leads to the decay of the LL precessions and aligns the magnetization along the effective magnetic field. The strength of the Gilbert dissipation is proportional to the phenomenological dimensionless damping constant α. In modern nanomagnetic devices its value is typically taken to be as small as $\alpha = 0.01$ [5, 46, 50], allowing for dozens of precession cycles of the magnetization

about the effective field prior to equilibration. A sample relaxation trajectory is shown in Fig. 2.2.

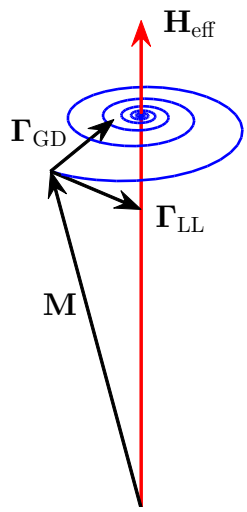

Figure 2.2: Relaxation trajectory of the magnetization for a free layer under the effects of Gilbert damping and the conservative LL torque. The magnetization is initially in a state with $E > 0$ and allowed to relax over several cycles.

In certain limits Eqn. (2.8) can also be written as the vector triple product

$$\mathbf{\Gamma}_{\text{GD}} = -\frac{\gamma}{M_{\text{s}}}\alpha\mathbf{M} \times [\mathbf{M} \times \mathbf{H}_{\text{eff}}] \tag{2.9}$$

in order to move all time derivatives to the LHS of Eqn. (2.8). This formalism for the damping torque is known as the Landau-Lifshitz damping torque, as it was first proposed by Landau and Lifshitz in 1935 [66]. In this form, the damping torque clearly is always perpendicular to the LL torque and thus the SW orbits of constant energy. For $\alpha \ll 1$, these two descriptions are equivalent so long as $\gamma \to \gamma/\left(1+\alpha^2\right)$ is substituted in Eqs. (2.5) and (2.8) (for a detailed derivation see Appendix A). Throughout this thesis Eqn. (2.9) is used to represent damping. To avoid confusion with the conservative LL torque, the damping torque is still referred to as the Gilbert damping torque.

2.4 Slonczewski spin-torque: $\mathbf{\Gamma}_{\mathrm{ST}}$

In 1996 both Slonczewski [3] and Berger [4] proposed a novel way of manipulating the magnetization of nanoscale magnetic objects by passing a spin-polarized current through the magnetic layer. The resulting effect has become known as spin-torque (ST), or spin-transfer torque (STT), due to the spin-angular momentum that is transferred from the spin-polarized current to the magnetic moment. A simple explanation for this effect is as follows. Entering the free layer, spin-polarized electrons find themselves either aligned (with the amplitude $\propto \cos\theta/2$), or antialigned (with the amplitude $\propto \sin\theta/2$) with the free layer magnetization direction, where θ is an angle between polarizations of the fixed and free layers. In the latter case strong exchange interactions cause a rapid spin-flip of the electron, transferring $\hbar$ angular momentum from the itinerant electron to the macroscopic magnetization of the free layer.

The corresponding non-conservative term in the macroscopic equation of motion takes the form

$$\mathbf{\Gamma}_{\mathrm{ST}} = \frac{\gamma}{M_{\mathrm{s}}}\mathcal{I}_{\mathrm{s}}\left[\mathbf{M}\times\left[\mathbf{m}_{\mathrm{p}}\times\mathbf{M}\right]\right], \tag{2.10}$$

which tends to align the magnetization along the spin-polarization of the electric current. Here the spin-current is represented by the effective magnetic moment $\vec{\mathcal{I}}_{\mathrm{s}} = \mathcal{I}_{\mathrm{s}}\mathbf{m}_{\mathrm{p}}$, where $\mathbf{m}_{\mathrm{p}}$ is a unit vector pointing along the direction of the pinned layer magnetization (see Fig. 1.1), and $\mathcal{I}_{\mathrm{s}}$ has units of magnetization and is proportional to the difference between the spin-up and spin-down electrons in the electrical current $\mathcal{I}_{\mathrm{s}} \propto (I_{\uparrow} - I_{\downarrow})\,\hbar/2e$. For simplicity, from this point forward $\vec{\mathcal{I}}_{\mathrm{s}}$ will be referred to as the spin-current. The magnitude of the spin-current can also be expressed in terms of the spin-conductances

$$\mathcal{I}_{\mathrm{s}} = \frac{\hbar V}{4eM_{\mathrm{s}}\mathcal{V}}\left(G_{++} - G_{-+} + G_{+-} - G_{--}\right) \tag{2.11}$$

where $G_{\sigma,\sigma'}$ are the partial conductances between the spin-polarized bands of the two ferromagnets [15, 74], V is the voltage across the tunneling barrier, and $\mathcal{V}$ is the volume of the free layer. This exchange of angular momentum can act to pump energy into the system (negative damping) or pull energy out of the system (positive damping), depending on the polarization of the spin-current in relation to the easy-axis of the free layer.

The form of the ST given in Eqn. (2.11) is most appropriate when using the Gilbert damping torque given in Eqn. (2.8). Converting to the LL formulism for the damping

given by Eqn. (2.9) gives rise to an additional "field like" torque

$$\mathbf{\Gamma}'_{\mathrm{ST}} = \gamma\,\alpha\,\mathcal{I}_{\mathrm{s}}\left[\mathbf{M}\times\mathbf{m}_{\mathrm{p}}\right]\,, \tag{2.12}$$

which acts like an applied external field pointed along the direction of the spin-current polarization. Due to the leading factor of α in Eqn. (2.12) this torque typically is small and can be ignored in certain limits.

An additional "field like" torque may result from non-equilibrium spin-accumulation in the free layer

$$\mathbf{\Gamma}_{\mathrm{FST}} = \gamma\,\beta\,\mathcal{I}_{\mathrm{s}}\left[\mathbf{M}\times\mathbf{m}_{\mathrm{p}}\right]\,, \tag{2.13}$$

which causes the free layer magnetization to precess about the direction of the spin-current polarization $\mathbf{m}_{\mathrm{p}}$. Here β represents the relative strength of the "field like" torque compared to the ST. This spin-accumulation comes from the fact that the transverse components of the spin-current persist with a characteristic relaxation length $\lambda_{\mathcal{I}}$, which may vary from only a few angstroms to several nanometers [75]. While some experimental [76] and theoretical works [77] have suggested the strength of this additional "field like" torque can be comparable in strength to the ST given by Eqn. (2.10), most have found $\beta \ll 1$ [74, 78, 79, 80]; thus it has been excluded from the remainder of this thesis.

2.5 Stochastic dynamics

The deterministic description of the previous sections is incomplete, especially for small enough magnetic domains. The reason is the stochastic part of the magnetic torque. The fact that noise must accompany Gilbert damping to satisfy the equilibrium fluctuation-dissipation theorem (FDT) was first realized by W. F. Brown [81]. Brown introduced the noise by adding a stochastic component to the effective magnetic field in Eqn. (2.5), $\mathbf{H}_{\mathrm{eff}} \to \mathbf{H}_{\mathrm{eff}} + \mathbf{h}_{\mathrm{th}}(t)$, where $\mathbf{h}_{\mathrm{th}}(t)$ is an isotropic Gaussian random field. Its amplitude may be uniquely determined from FDT and is given by

$$\langle \mathbf{h}_{\mathrm{th},i}(t)\mathbf{h}_{\mathrm{th},j}(t')\rangle = 2\frac{\alpha k_{\mathrm{B}}T}{\gamma M_{\mathrm{s}}\mathcal{V}}\delta_{ij}\delta(t-t')\,, \tag{2.14}$$

where T is the temperature of the free layer, $\mathcal{V}$ is the volume of the free layer, and k_{B} is the Boltzman constant. This thermal noise manifests as random fluctuation of the magnetization away from the deterministic trajectory, as shown in Fig. 2.3. At low

energies it acts to push the magnetization away from the easy-axis, giving the free layer positive average initial energy and average initial deviation from the easy-axis. This effect will be critical in some of the switching dynamics discussed in later chapters.

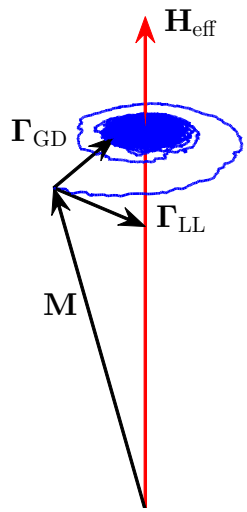

Figure 2.3: Relaxation trajectory for the magnetization of a free layer under the effects of Gilbert damping, the conservative LL torque, and stochastic thermal noise. The magnetization is initially in a state with $E > 0$ and allowed to relax over several cycles.

Noise may also be introduced by the spin-current through shot noise [82] $\vec{\mathcal{I}}_{\mathrm{s}} \rightarrow \vec{\mathcal{I}}_{\mathrm{s}} + \delta\vec{\mathcal{I}}_{\mathrm{sh}}$ where $\delta\vec{\mathcal{I}}_{\mathrm{sh}}(t)$ is isotropic Gaussian random component of the spin-current with

$$\langle \delta\mathcal{I}_{\mathrm{sh,i}}(t)\delta\mathcal{I}_{\mathrm{sh,j}}(t')\rangle = 2D_{\mathrm{sh}}(\theta)\delta_{i,j}\delta(t-t'). \tag{2.15}$$

While in the previous case the noise correlator was coordinate independent, here D_{sh} depends on the angle θ between the fixed and free layers. This noise correlator D_{sh} is calculated in Ref. [16] as

$$D_{\mathrm{sh}}(\theta) = \frac{\hbar\mathcal{I}_{\mathrm{sf}}(\theta)}{2M_{\mathrm{s}}\mathcal{V}} \coth\left(\frac{eV}{2k_{\mathrm{B}}T}\right), \tag{2.16}$$

where V is the voltage bias between the fixed and free layers and $\mathcal{I}_{\mathrm{sf}}(\theta)$ is the spin-flip current given by

$$\mathcal{I}_{\mathrm{sf}}(\theta) = \frac{\hbar V}{4eM_{\mathrm{s}}\mathcal{V}}\left[G_{\mathrm{p}}\sin^2\left(\frac{\theta}{2}\right) + G_{\mathrm{ap}}\cos^2\left(\frac{\theta}{2}\right)\right]. \tag{2.17}$$

Here

$$G_{\mathrm{p}} = G_{++} + G_{--}\,; \qquad G_{\mathrm{ap}} = G_{+-} + G_{-+}\,, \tag{2.18}$$

are the conductances for the electrons with spin parallel and antiparallel to the free layer, respectively, and $G_{\sigma,\sigma'}$ are the partial conductances between the spin bands of the two ferromagnets. Since the parallel conductance is always larger than the anti-parallel conductance, $G_{\mathrm{p}} > G_{\mathrm{ap}}$, the spin-shot noise is strongest when the fixed and free layers are anti-aligned.

Together, Eqs. (2.14) and (2.15) describe the total noise affecting the free layer $\mathbf{h}(t) = \mathbf{h}_{\mathrm{th}}(t) + \mathbf{h}_{\mathrm{sh}}(t)$ with total correlator

$$D(\theta) = \frac{\alpha k_{\mathrm{B}} T}{\gamma M_{\mathrm{s}} \mathcal{V}} + \frac{\hbar \mathcal{I}_{\mathrm{sf}}(\theta)}{2 M_{\mathrm{s}} \mathcal{V}} \coth\left(\frac{eV}{2k_{\mathrm{B}}T}\right)\,, \tag{2.19}$$

where $\mathbf{h}_{\mathrm{sh}}(t) = \delta\vec{\mathcal{I}}_{\mathrm{sh}}(t)$. For MTJs operating below approximately 20K and for currents on the order of the minimum current needed to produce switching, the spin-shot noise term in Eqn. (2.19) dominates [83]. However, as most practical applications of spin-torque require room temperature conditions, where thermal noise dominates, only thermal noise is considered hereafter.

2.6 Numerical simulations

Throughout this thesis numerical simulations are used to probe and verify the behavior of the model described above under the influence of different spin-current strategies. These numerical simulations were performed using fourth-order Runge-Kutta integration of Eqn. (2.1) with an adaptive time step to improve simulation speed while confining numerical errors. Thermal noise was included via random number generators along with an inverse Gaussian projection algorithm to produce the Gaussian distributions for each of the three random fields, $h_i(t)$.

Single trajectory simulations (see Fig. 3.2) and some probability-vs-time simulations (see Fig. 4.6) were run using C# with random numbers generated using a Mersenne-Twister algorithm [84]. Two-dimensional switching probability simulations (see Fig. 4.4) were performed using OpenCL via C++ with random numbers generated via a floating-point XorShift algorithm [85].

OpenCL is a programming language that allows numerical calculations to be delegated to graphic processing units (GPU) such as those on a standard computer video card. This approach allows for a high level of parallel calculations without the need for a supercomputer, allowing for much higher resolution in the switching probabilities. This approach can also lead to a significant reduction in computing time with a relatively increase in overhead.

Chapter 3

DC spin-torque

3.1 Introduction

In this chapter I cover ST switching and Joule heat loss (JHL) minimization using DC spin-currents. To begin, I present numerical simulations showing the effect of three different spin-current polarizations: along the easy-axis, along the easy-plane axis, and along the hard axis in the easy-plane. These simulations serve to build our intuition regarding the effects of spin-polarization in DC spin-torque switching and provide justification for certain approximations used hereafter. Next, I present a theoretical description of DC ST switching that approximates Eqn. (2.1), hereafter known as the Landau-Lifshitz-Gilbert-Slonczewski (LLGS) equation, reducing it to a one-dimensional equation of motion for the energy of the free layer. This description is then applied to the task of minimizing the energy loss to dissipation during the switching process, i.e., JHL.

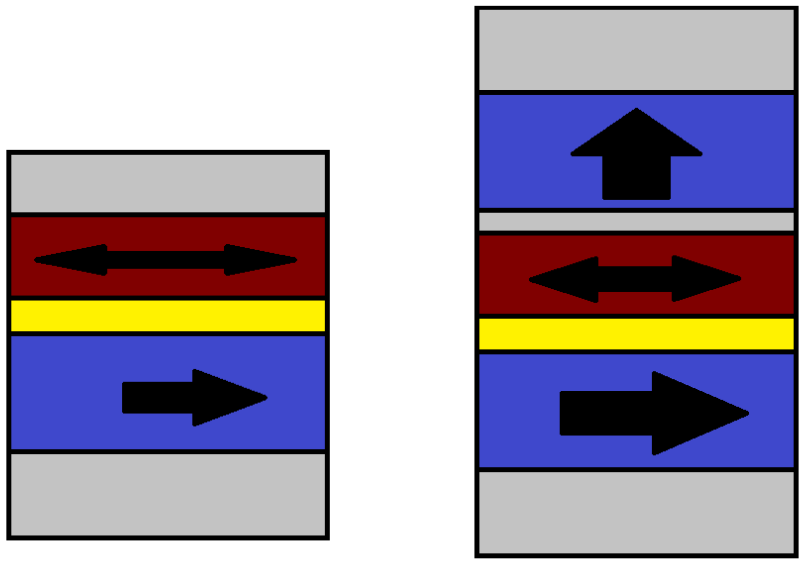

Figure 3.1: Cartoon of a collinearly configured MTJ (left) and a perpendicularly configured MTJ (right).

3.2 Numerical simulations of DC switching

The effect of ST on the free layer of a MTJ depends strongly on the direction the spin-current is polarized. Given that the free layer energy landscape is described in terms of easy-axis $\hat{\mathbf{e}}_{\mathrm{x}}$, hard-axis $\hat{\mathbf{e}}_{\mathrm{y}}$, and easy-plane axis $\hat{\mathbf{e}}_{\mathrm{z}}$, it seems natural to look at the free layer response to spin-currents polarized along these directions as well. In this section I present simulations showing how the magnetization of the free layer responds to two types of MTJ devices that have been studied experimentally and theoretically over the last decade.

Historically, ST switching using DC spin-currents has been broken up into two types of devices, each utilizing different spin-current polarizations to induce switching. The first of these involves ST switching in MTJs with a single polarizing layer whose magnetization is aligned along the easy-axis of the free layer (see Fig. 3.1). The spin-current polarization for these devices, using the notation from chapter 2, is $\mathbf{m}_{\mathrm{p}} = \hat{\mathbf{e}}_{\mathrm{x}}$. This configuration, hereafter known as the collinear configuration, is characterized by relatively

slow switching times, typically on the order of several ns, and broad switching time distributions that depend strongly on temperature.

Several switching trajectories are shown in Fig. 3.2 for collinear MTJs with strong easy-plane anisotropy and with uniaxial anisotropy, i.e., no easy-plane anisotropy. Notice in both cases, and for all spin-current strengths, the switching trajectories spend a significant amount of time very close to the easy-axis direction before switching. This incubation time comes from the fact that the strength of the ST on the free layer goes to zero when the free layer magnetization and spin-current polarization are perfectly collinear. This means at small angles thermal effects dominate the dynamics of the free layer, thus the incubation time is the time needed for thermal noise to push the magnetization to sufficiently large angles where the ST is strong enough to induce switching.

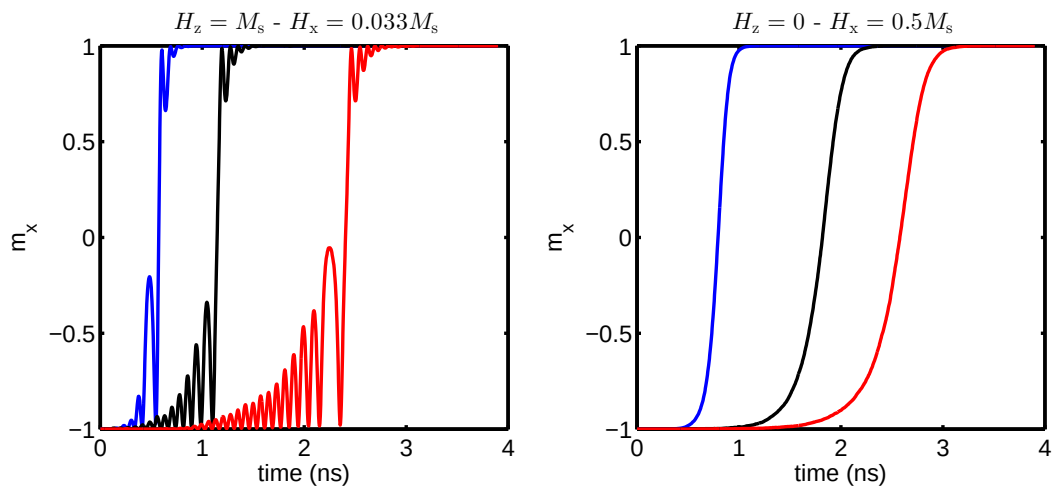

Figure 3.2: Switching trajectories for collinear MTJ with $H_x = 0.033M_s$ and $H_z = M_s$ (Left) and with $H_x = 0.5M_s$ and $H_z = 0$ (right). Spin-currents from left to right in each are $\mathcal{I}_s = 0.037M_s$ (blue), $\mathcal{I}_s = 0.018M_s$ (black), and $\mathcal{I}_s = 0.015M_s$ (red). Here $\alpha = 0.015$, $T = 300$K, and $\mathbf{m}_p = \hat{\mathbf{e}}_z$.

A variant on this type of device cants the magnetization of the polarizing layer away from the free layer easy-axis direction. This canting increases the initial angle between free layer magnetization and the spin-current polarization, which in turn increases the

strength of the ST. The spin-current polarization for such devices also includes a contribution along the hard-axis of the free layer such that $\mathbf{m}_\mathrm{p} = \eta_\mathrm{x}\hat{\mathbf{e}}_\mathrm{x} + \eta_\mathrm{y}\hat{\mathbf{e}}_\mathrm{y}$ where η_x and η_y represent the fraction of the spin-current polarized along the easy-axis and hard-axis directions, respectively.

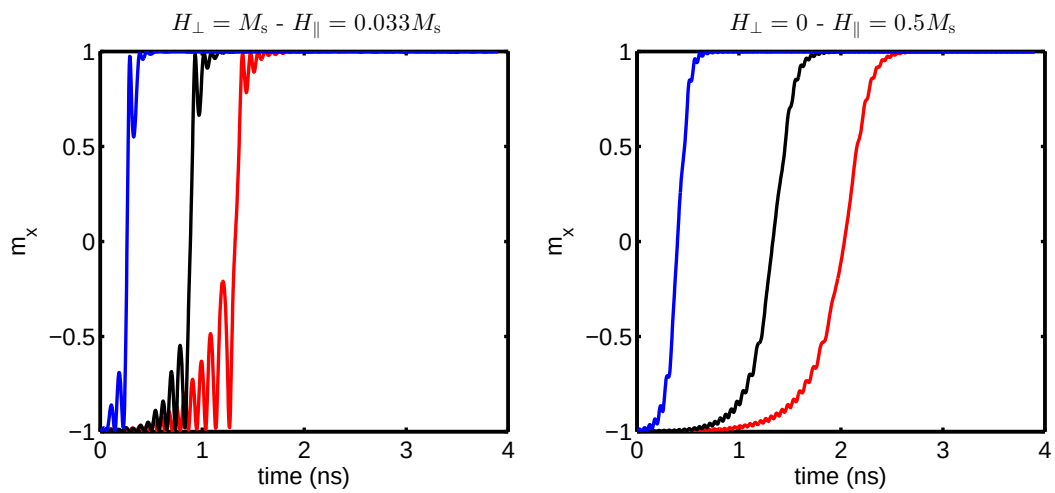

Figure 3.3: Switching trajectories for MTJs with a polarizing layer canted along the free layer hard-axis in the easy-plane. (Left) Free layer with $H_\mathrm{x} = 0.033M_\mathrm{s}$ and $H_\mathrm{z} = M_\mathrm{s}$. (Right) Free layer with $H_\mathrm{x} = 0.5M_\mathrm{s}$ and $H_\mathrm{z} = 0$. Spin-currents from left to right in each are $\mathcal{I}_\mathrm{s} = 0.037M_\mathrm{s}$ (blue), $\mathcal{I}_\mathrm{s} = 0.018M_\mathrm{s}$ (black), and $\mathcal{I}_\mathrm{s} = 0.015M_\mathrm{s}$ (red). Here $\alpha = 0.015$, $T = 300K$, and $\mathbf{m}_\mathrm{p} = \hat{\mathbf{e}}_\mathrm{y} + \hat{\mathbf{e}}_\mathrm{z}$.

Simulations of switching trajectories for such devices are shown in Fig. 3.3 for both of the free layer anisotropy configurations shown previously in Fig. 3.2. One may note that in both examples the resulting switching trajectories look qualitatively similar to those in Fig. 3.2 for the equivalent collinear MTJ. One may also note that the switching times are notably shorter due to a marked shortening of the incubation time. This shortening of the incubation time is the result of the ST from the hard-axis polarized portion of the spin-current being strongest when the free layer magnetization is along the easy-axis. However, as the free layer's magnetization begins to switch the strength of the hard-axis ST decreases. The overall impact of $\hat{\mathbf{e}}_\mathrm{y}$-polarized ST is further limited by the precessional motion of the free layer about the easy-axis. Through half of each

SW orbit the hard-axis ST pushes the free layer to higher energy orbits, and through the other half it pulls the free layer to lower energy orbits. Provided the overall change in free layer energy with each revolution is small, the hard-axis ST exactly cancels; thus the overall switching speed and dynamics remain controlled by the strength of the easy-axis ST.

The second type of DC ST device found in the literature adds an additional polarizing layer to the MTJ mentioned previously that has its magnetization aligned along the easy-plane direction of the free layer (see Fig. 3.1). This type of dual-polarizer MTJ was first proposed by Kent *et al* [57]. Devices with this configuration, hereafter known as the perpendicular configuration, exhibit switching times that are significantly faster than those found in collinear devices (typically less than a ns) with narrow switching time distributions [86, 87, 88, 89]. The spin-polarization for these devices can be expressed as $\mathbf{m}_\mathrm{p} = \eta_\mathrm{x}\hat{\mathbf{e}}_\mathrm{x} + \eta_\mathrm{z}\hat{\mathbf{e}}_\mathrm{z}$ where η_x and η_z are the fraction of the spin-current polarized along the easy-axis and easy-plane directions, respectively.

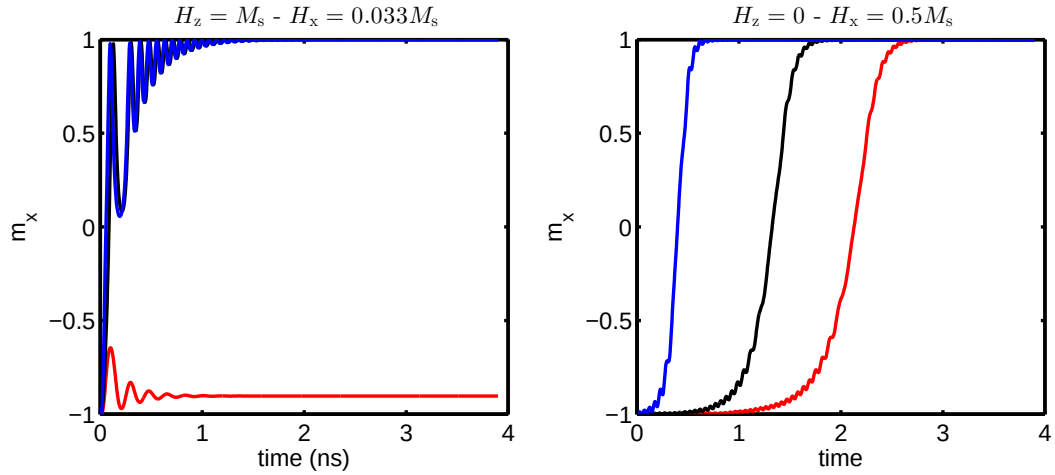

Figure 3.4: Switching trajectories for perpendicular MTJ with $H_\mathrm{x} = 0.033M_\mathrm{s}$ and $H_\mathrm{z} = M_\mathrm{s}$ (left) and with $H_\mathrm{x} = 0.5M_\mathrm{s}$ and $H_\mathrm{z} = 0$ (right). Spin-currents from left to right in each are $\mathcal{I}_\mathrm{s} = 0.037M_\mathrm{s}$ (blue), $\mathcal{I}_\mathrm{s} = 0.018M_\mathrm{s}$ (black), and $\mathcal{I}_\mathrm{s} = 0.015M_\mathrm{s}$ (red). Here $\alpha = 0.015$, $T = 300\mathrm{K}$, and $\mathbf{m}_\mathrm{p} = \hat{\mathbf{e}}_\mathrm{x} + \hat{\mathbf{e}}_\mathrm{z}$.

Figure 3.4 shows several switching trajectories for the free layers of perpendicular

MTJs. From Fig. 3.4 one may immediately notice the dramatic difference in the switching trajectories between the free layer with strong easy-plane anisotropy and the free layer with uniaxial anisotropy. For the uniaxial free layer, the switching trajectories look very similar those of the uniaxial free layer in Fig. 3.3. This is expected given the symmetry of the uniaxial anisotropy free layer about the $\hat{\mathbf{e}}_{\mathrm{x}}$ axis.

For the free layer with strong easy-plane anisotropy in 3.4 the results are starkly different from those seen in any of the parallel devices shown in Figs. 3.2 and 3.3. Most notably the the switching times are dramatically shorter from those of the collinear devices using similar spin-current strengths. This increase in switching speed is understood by noting the shape of the SW orbits in Fig. 2.1 for the free layers with strong easy-plane anisotropy. Here the magnetization is strongly confined close to the easy-plane throughout the switching process where the strength of the perpendicular ST is strongest.

One may also note from Fig. 3.4 that for the lowest spin-current strength shown, switching does not occur despite this same spin-current strength producing switching in both collinear devices shown previously in Figs. 3.2 and 3.3. This abrupt change in switching behavior is due to the precessional motion of the magnetization about the easy-axis. Despite the strong ST on the free layer, the free layer magnetization still precesses about the effective field. This precession causes the perpendicular ST to self-cancel with each full revolution; thus the spin-current must be strong enough such that switching takes place faster than half the precessional period. For the device simulated in Fig. 3.4 this means $t_{\mathrm{sw}} \approxeq 0.1$ns, which is in good agreement with the simulated trajectories shown.

It is important to note that in order to produce the two switching events for the perpendicular MTJ with strong easy-plane anisotropy shown in Fig. 3.4, the spin-current was turned off just after the magnetization crossed the saddle point into the other potential well. Had the spin-current been left on for the duration of the simulations, as was done in all of the other simulations shown in this section, the magnetization would have been driven to an excited orbit about the easy-plane axis. In this way, ST switching of MTJs with strong easy-plane anisotropy is strongly dependent on the pulse duration [90]. This dependence on the current pulse duration is discussed in more detail in Sec. 3.6.

3.3 Theoretical description: energy/angle coordinates

With a basic understanding of how spin-current polarization affect the switching behavior of MTJ free layers, I now present a theoretical description for free layer dynamics under the effect of ST. This description is used in the section that follows, where it is applied directly to the problem of DC switching, and in chapters 4 and 5, where it is applied to AC ST switching and switching using combined AC and DC spin-torque pulses.

In order for any spin-current pulse to switch the magnetization of a MTJ free layer, the ST must first push the magnetization into an excited state, i.e., where $E > E_{\mathrm{b}} = \frac{1}{2}H_{\mathrm{x}}M_{\mathrm{s}}$. In this process the ST is opposed by damping, which pulls the magnetization to lower energy. Since the damping torque $\mathbf{\Gamma}_{\mathrm{GD}}$ always points perpendicular to the SW orbits of constant energy, a natural way of assessing the strength of the ST is to decompose it into components parallel to the SW orbits and perpendicular to them.

To this end, the free layer magnetization can be written in terms of the locally orthogonal coordinates E and φ such that $\mathbf{M} = \mathbf{M}(E, \varphi)$ [91]. Here E is nothing more than the energy of the free layer given by Eqn. (2.7), and $\varphi = 2\pi\tau/P(E)$ is the time τ into the SW orbit with energy E in the absence of spin-torque and damping, normalized to 2π. Here $P(E)$ is the energy-dependent precessional period of the magnetization about the easy-axis in the absence of ST and damping. From Eqn. (2.5), τ and $P(E)$ are given by

$$d\tau = \frac{\mathbf{\Gamma}_{\mathrm{LL}} \cdot d\mathbf{M}}{|\mathbf{\Gamma}_{\mathrm{LL}}|^2}\,; \qquad P(E) = \oint \frac{\mathbf{\Gamma}_{\mathrm{LL}} \cdot d\mathbf{M}}{|\mathbf{\Gamma}_{\mathrm{LL}}|^2}\,. \tag{3.1}$$

Here the integral runs along the SW orbit with energy E. The parametrization $\mathbf{M} = \mathbf{M}(E, \varphi)$ is given implicitly by the following relations:

$$\partial_\varphi \mathbf{M} = \frac{\mathbf{\Gamma}_{\mathrm{LL}}}{\Omega(E)}\,; \qquad \partial_E \mathbf{M} = -\frac{\gamma\big[\mathbf{\Gamma}_{\mathrm{LL}} \times \mathbf{M}\big]}{\big|\mathbf{\Gamma}_{\mathrm{LL}}\big|^2}\,, \tag{3.2}$$

where $\Omega(E) = 2\pi/P(E)$ is the energy-dependent natural precessional frequency of the free layer [92]. The first of these relations is a consequence of the LL equation (2.5) and the choice of φ, and the second can be checked, e.g., by going to the instantaneous reference frame, where $\mathbf{H}_{\mathrm{eff}}$ is directed along the z-axis. One may check that indeed E and φ are orthogonal by noting $\partial_\varphi \mathbf{M} \cdot \partial_E \mathbf{M} = 0$. It should be noted that this

parameterization is not global and must instead be introduced separately for each of the basins apparent in Fig. 2.1.

The equations of motion for the free layer magnetization in these new coordinates are found using the following relations:

$$\dot{E} = \nabla_{\mathbf{M}} E \cdot \dot{\mathbf{M}} = -\mathbf{H}_{\text{eff}} \cdot \dot{\mathbf{M}}\,; \qquad \dot{\varphi} = \Omega(E) \frac{\mathbf{\Gamma}_{\text{LL}} \cdot \dot{\mathbf{M}}}{|\mathbf{\Gamma}_{\text{LL}}|^2}. \tag{3.3}$$

Substituting Eqn. (2.1) into Eqs. (3.3) for $\dot{\mathbf{M}}$, the LLGS equation of motion for the energy of the free layer becomes

$$\dot{E} = -\alpha\, U(E, \varphi) + \mathcal{I}_{\text{s}} V(E, \varphi)\,. \tag{3.4}$$

Here the fast LL precessional motion of the free layer drops out, as expected, and the two remaining *generalized forces* on the RHS represent the effects of dissipation and ST, respectively, on the energy of the free layer. They are given by

$$U(E, \varphi) = \frac{1}{\gamma M_{\text{s}}}\, |\mathbf{\Gamma}_{\text{LL}}|^2\,; \qquad V(E, \varphi) = \frac{1}{M_{\text{s}}}\, [\mathbf{\Gamma}_{\text{LL}} \times \mathbf{M}] \cdot \mathbf{m}_{\text{p}}. \tag{3.5}$$

The LLGS equation of motion for the angle φ upon this same substitution is

$$\dot{\varphi} = \Omega(E) + \mathcal{I}_{\text{s}} W(E, \varphi)\,. \tag{3.6}$$

Here $W(E, \varphi)$ represents the effect of the ST on the precessional motion of the free layer about the effective field and is given by

$$W(E, \varphi) = \gamma M_{\text{s}} \Omega(E) \frac{\mathbf{\Gamma}_{\text{LL}} \cdot \mathbf{m}_{\text{p}}}{|\mathbf{\Gamma}_{\text{LL}}|^2}\,. \tag{3.7}$$

To give a visual representation of how the examples in the previous section look in this new coordinate system, Fig. 3.5 plots $V(E, \varphi)$ for a free layer with uniaxial anisotropy with spin-current polarizations along each of the three basis directions at both low and high energies. Notice the clear oscillatory, self-canceling nature of the ST coming from the spin-currents polarized along the easy-plane and hard-axis directions. Notice also the easy-axis ST is stronger at larger energies while the other two get weaker.

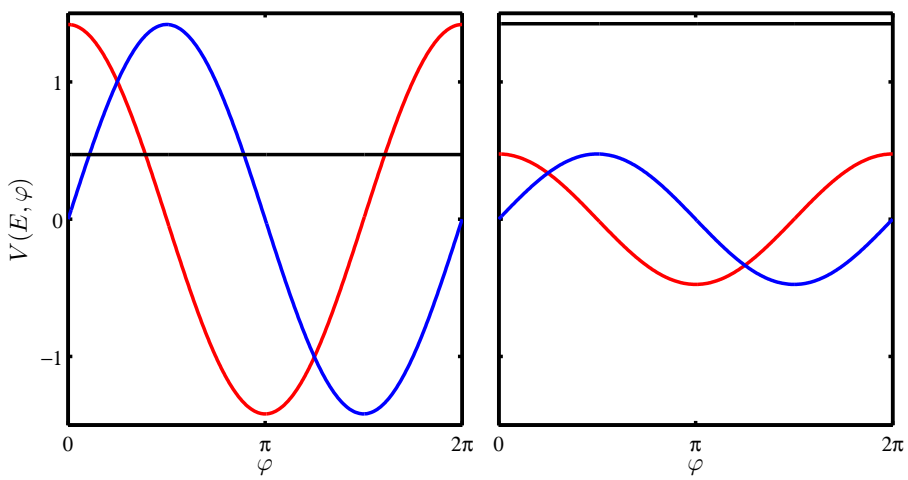

Figure 3.5: $V(E,\varphi)$ in arbitrary units as a function of φ for a free layer with uniaxial anisotropy ($H_{\rm x} = 0.5M_{\rm s}$ and $H_{\rm z} = 0$) with spin-current polarizations, $\hat{\mathbf{e}}_{\rm x}$ (black), $\hat{\mathbf{e}}_{\rm y}$ (blue), and $\hat{\mathbf{e}}_{\rm z}$ (red). Here $E = 0.1E_{\rm b}$ (left) and $E = 0.9E_{\rm b}$ (right).

Figure 3.6 plots $V(E,\varphi)$ for a free layer with strong easy-plane anisotropy in the same arbitrary units used in Fig. 3.5. Note that for low energies the easy-axis and hard-axis ST are similar in strength to the uniaxial case shown in Fig. 3.5. However, the easy-plane ST is significantly stronger. Furthermore, the strength of the easy-plane ST grows with energy. This is in stark contrast to its behavior in the uniaxial case.

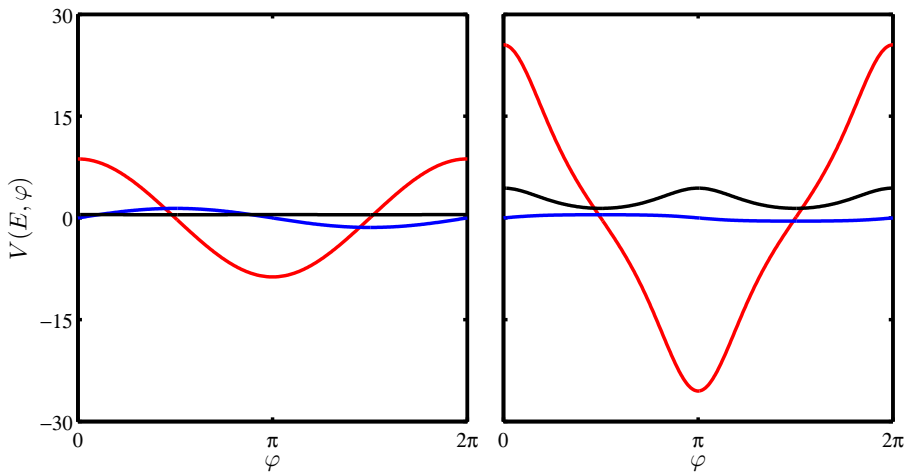

Figure 3.6: $V(E,\varphi)$ in arbitrary units as a function of φ for free layer with strong easy-plane anisotropy ($H_{\rm x} = 0.031 M_{\rm s}$ and $H_{\rm z} = M_{\rm s}$) with spin-current polarizations $\hat{\mathbf{e}}_{\rm x}$ (black), $\hat{\mathbf{e}}_{\rm y}$ (blue), and $\hat{\mathbf{e}}_{\rm z}$ (red). Here $E = 0.1E_{\rm b}$ (Left) and $E = 0.9E_{\rm b}$ (right).

3.4 Theoretical description: time-scale separation

Setting aside for a moment ST switching using easy-plane $\hat{\mathbf{e}}_{\rm z}$-polarized spin-currents, for all of the ST polarizations and anisotropy configurations covered in Secs. 3.2 and 3.3 the preceding two sections, switching takes place on time scales much longer than the precessional period $P(E)$ of the free layer. This means the free layer precesses many times before switching; thus, the characteristic time scale for E is significantly longer than for φ. This separation in time scales suggests the equations of motion given by Eqs. (3.4) and (3.6) can be approximated by averaging each about φ. For this approximation to be valid, the strength of the spin-current $\mathcal{I}_{\rm s}$ must remain small enough for this time-scale separation to remain true. In practice I have found this to be the case for spin-currents on the same order as the critical current, i.e., the minimum current needed to produce switching in the absence of thermal noise. For a more rigorous analysis of when this φ-averaging is appropriate see Sec. 6.3. While this strategy was shown to be useful in the analysis of non-linear oscillators long ago [93], it was probably first applied in the present context by Apalkov and Visscher [94] and further developed by Bertotti [95].

In this section I apply such a time-scale separation and averaging technique to the

equations of motion derived in Sec. 3.3 for $\hat{\mathbf{e}}_{\mathrm{x}}$ and $\hat{\mathbf{e}}_{\mathrm{y}}$-polarized spin-currents to obtain an approximate equation of motion for the energy of the free layer. This approximation is them used to describe DC ST switching. Specifically, I use it to show how the ST can lead to steady-state precessional regimes and to calculate the critical current as a function of the relative anisotropy strength and polarization. Lastly, I show how this formalism leads to a simple form for the switching time that is qualitatively similar to fitting equations used in experiment.

3.4.1 φ-averaged energy dynamics

Averaging Eqn. (3.4) with respect to φ, the energy equation of motion is

$$\dot{E} = -\alpha U(E) + \overline{\mathcal{I}}_{\mathrm{s}} \overline{V}_{\mathrm{x}}(E)\,. \tag{3.8}$$

Here the new φ-averaged generalized energy forces are given by

$$U(E) = \frac{1}{\gamma M_{\mathrm{s}} P(E)} \oint \mathbf{\Gamma}_{\mathrm{LL}} \cdot d\mathbf{M}\,; \qquad \overline{V}_{\mathrm{x}}(E) = \frac{\eta_{\mathrm{x}}}{M_{\mathrm{s}} P(E)} \oint [d\mathbf{M} \times \mathbf{M}] \cdot \hat{\mathbf{e}}_{\mathrm{x}}\,, \tag{3.9}$$

where each of the integrals runs along the SW orbit with energy E, and $\eta_{\mathrm{x}} = \hat{\mathbf{e}}_{\mathrm{x}} \cdot \mathbf{m}_{\mathrm{p}}$ represents the fraction of the spin-current polarized along the easy-axis $\hat{\mathbf{e}}_{\mathrm{x}}$-direction [96]. Here also, the bar over the spin-current strength $\overline{\mathcal{I}}_{\mathrm{s}}$ and the ST energy force $\overline{V}_{\mathrm{x}}$ is used to denote that the spin-current being applied is of a DC nature (this notation is used throughout the remainder of this thesis to denote DC spin-currents and φ-averaged variables associated with DC spin-currents). As expected, the $\hat{\mathbf{e}}_{\mathrm{y}}$ and $\hat{\mathbf{e}}_{\mathrm{z}}$ contributions to the ST vanish upon averaging since both are periodic in φ with zero average. One may also notice Eqn. (3.8) is entirely independent of φ; thus, the switching behavior has been reduced to a one-dimensional system. Fig. 3.7 compares a typical switching trajectory with the φ-averaged trajectory calculated using Eqn. (3.8). Note the good agreement between them.

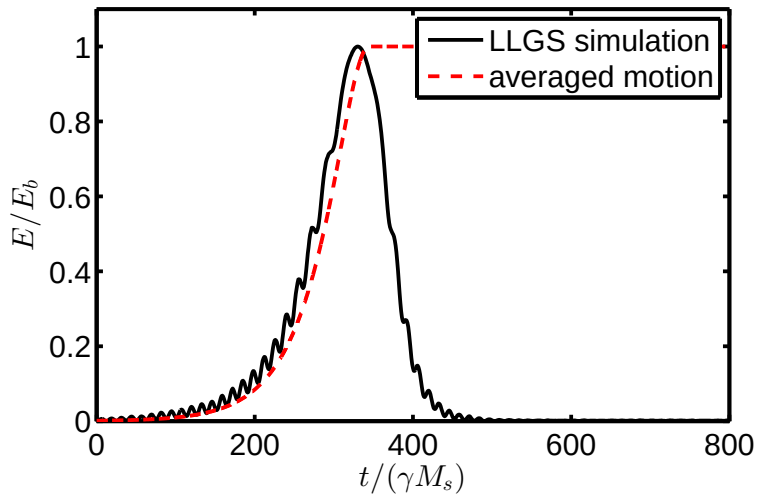

Figure 3.7: Free layer energy $E(t)$ vs. time, under the effect of a DC spin-current, calculated via numerical integration of the LLGS equation (black,solid) and Eqn. (3.8) (red,dashed). Here $H_\mathrm{x} = 0.5M_\mathrm{s}$, $H_\mathrm{z} = 0$, $\alpha = 0.015$, $T = 0$, $\overline{\mathcal{I}}_\mathrm{s} = 0.02M_\mathrm{s}$, and $\mathbf{m}_\mathrm{p} = \hat{\mathbf{e}}_\mathrm{x} + \hat{\mathbf{e}}_\mathrm{z}$.

While it does not play into the dynamics results that follow, for completeness, it is worth averaging the φ equation of motion given by Eqn. (3.6) about φ as well. This gives

$$\dot{\varphi} = \Omega(E)\,. \tag{3.10}$$

Here the ST force on the precessional motion, $W(E, \varphi)$, vanishes regardless of the spin-current polarization. This means, to good approximation, the precessional frequency remains the same as the energy-dependent natural frequency of the free layer $\Omega(E)$. This will prove not to be the case in chapters 4 and 5 when describing the effects of AC spin-current on the free layer.

3.4.2 Equilibrium condition and critical current

An important advantage to this approach for describing the free layer response to a DC spin-current is that to evaluate Eqs. (3.8) and (3.10), along with their corresponding forces, one does not need any information about dynamics, but rather only the form of the *static* SW orbits and spin-current polarization vector $\mathbf{m}_\mathrm{p}$. This is demonstrated in

Fig. 3.8, which plots $\dot{E}$ as a function of energy for a free layer with strong easy-plane anisotropy at several strengths of spin-current $\overline{\mathcal{I}}_{\rm s}$. One can immediately see that for certain values of $\overline{\mathcal{I}}_{\rm s}$, switching will occur regardless of thermal noise (i.e., $\dot{E}$ is strictly positive), while for other it will not (i.e.$\dot{E}$ is strictly negative). More interestingly, for a small range of $\overline{\mathcal{I}}_{\rm s}$ values steady-state precessional motion may occur $\dot{E}(E_{\rm eq}) = 0$ [35, 10].

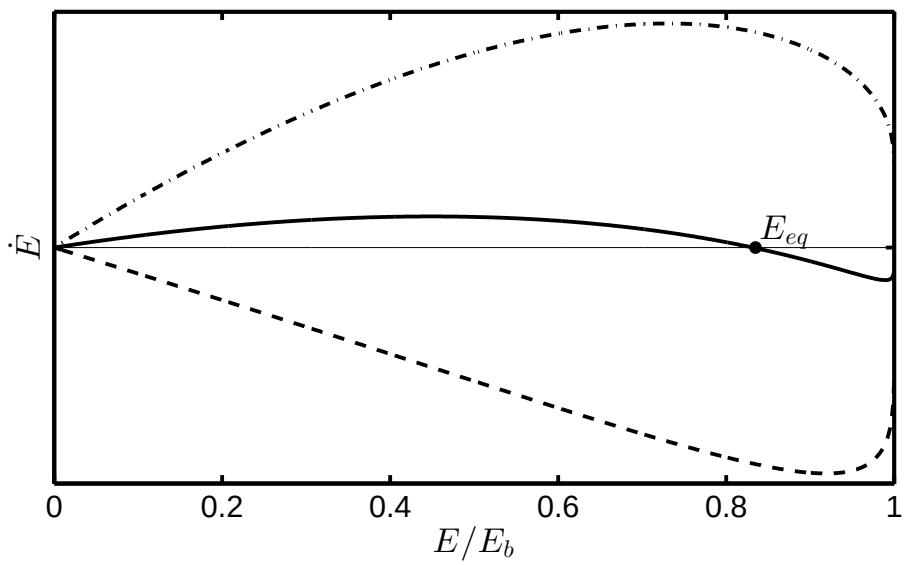

Figure 3.8: Plots $\dot{E}$ vs. energy for various strengths of $\overline{\mathcal{I}}_{\rm s}$ for a free layer with $H_{\rm x} = 0.033M_{\rm s}$ and $H_{\rm z} = M_{\rm s}$. From top to bottom $\overline{\mathcal{I}}_{\rm s} = 0.012M_{\rm s}$ (dot-dashed), $\overline{\mathcal{I}}_{\rm s} = 0.009M_{\rm s}$ (solid), $\overline{\mathcal{I}}_{\rm s} = 0.006M_{\rm s}$ (dashed). For $\overline{\mathcal{I}}_{\rm s} = 0.009M_{\rm s}$ the equilibrium energy is marked by $E_{\rm eq}$.

For free layer anisotropy configuration where steady-state precessions are possible, the spin-current required to produce such an orbit can be thought of as a local critical current $\overline{\mathcal{I}}_{\rm c}(E)$, i.e., the current needed to exactly cancel the local damping. This local critical current is easily calculated from Eqn. (3.8) by setting the LHS equal to zero and solving for $\overline{\mathcal{I}}_{\rm s}$,

$$\overline{\mathcal{I}}_{\rm c}(E) = \frac{\alpha U(E)}{\overline{V}_{\rm x}(E)}\,. \tag{3.11}$$

Figure 3.9 shows $\overline{\mathcal{I}}_{\rm c}(E)$ for the two limiting cases with uniaxial anisotropy and strong

easy-plane anisotropy. Notice that for the free layer with strong easy-plane anisotropy $\overline{\mathcal{I}}_{\rm c}$ is nearly constant, while for the free layer with uniaxial anisotropy $\overline{\mathcal{I}}_{\rm c}$ changes significantly with energy. The negative slope of $\overline{\mathcal{I}}_{\rm c}(E)$ in the uniaxial anisotropy free layer indicates that $E_{\rm eq}$ is an unstable equilibrium point, while the positive slope for the free layer with strong easy-plane anisotropy indicates $E_{\rm eq}$ is a stable equilibrium point.

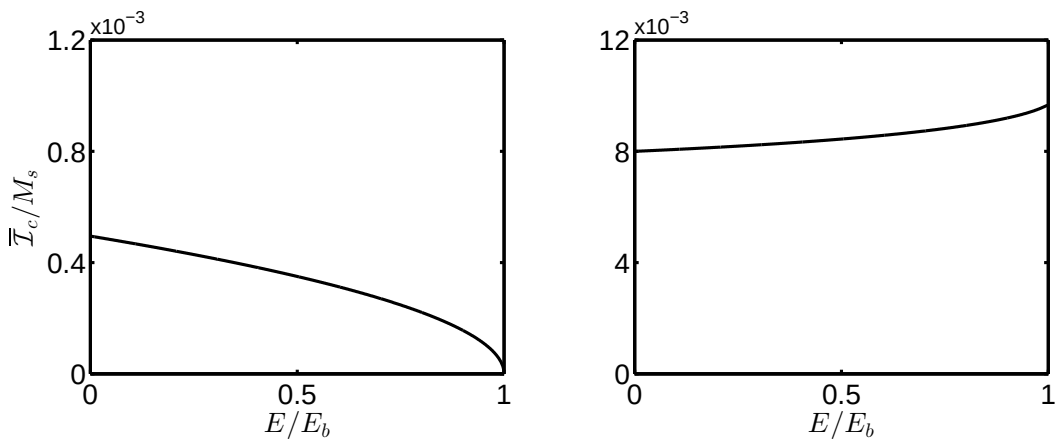

Figure 3.9: Local critical spin-current $\overline{\mathcal{I}}_{\rm c}(E)/M_{\rm s}$ as a function of energy for a free layer with uniaxial anisotropy, $H_{\rm x} = 0.033 M_{\rm s}$ and $H_{\rm z} = 0$ (left), and a free layer with strong easy-plane anisotropy, $H_{\rm x} = 0.033 M_{\rm s}$ and $H_{\rm z} = M_{\rm s}$ (right). Here $\alpha = 0.015$.

Since the critical current is defined as the minimum spin-current needed to produce a switch, i.e., overcome damping, it can be calculated from the local critical current as

$$\overline{\mathcal{I}}_{\rm c} = \max\left\{\overline{\mathcal{I}}_{\rm c}(E) | 0 < E < E_{\rm b}\right\} . \tag{3.12}$$

Figure 3.10 shows the critical current as a function of the anisotropy ratio $h = H_{\rm z}/H_{\rm x}$ for $\mathbf{m}_{\rm p} = \hat{\mathbf{e}}_{\rm x}$. It is clear from Fig. 3.10 that the critical current follows two linear trends, with an elbow near $h = 5$. These two lines correspond to the local critical currents at energies $E = 0$ and $E = E_{\rm b}$ and can be calculated exactly for any anisotropy configuration, giving

$$\overline{\mathcal{I}}_{\rm c}(0) = \alpha H_{\rm x} \frac{h+2}{2\,\eta_{\rm x}} ; \qquad \overline{\mathcal{I}}_{\rm c}(E_{\rm b}) = \alpha H_{\rm x} \frac{2\sqrt{h(h+1)}}{\pi\,\eta_{\rm x}} . \tag{3.13}$$

For a detailed derivation of these equations, see Appendix B.3. The first is exactly the

critical current calculated in Ref. [48] for low-field switching and corresponds to the spin-current needed to dislodge the magnetization from the energy minimum; the second is the spin-current needed to push the magnetization over the energy barrier [97, 98]. The abrupt change in the scaling of $\overline{\mathcal{I}}_{\rm c}$ is due to a first-order phase transition in the value of the maximum local critical current. The equilibrium point between these two critical current lines is $h \approxeq 5.09$ [98].

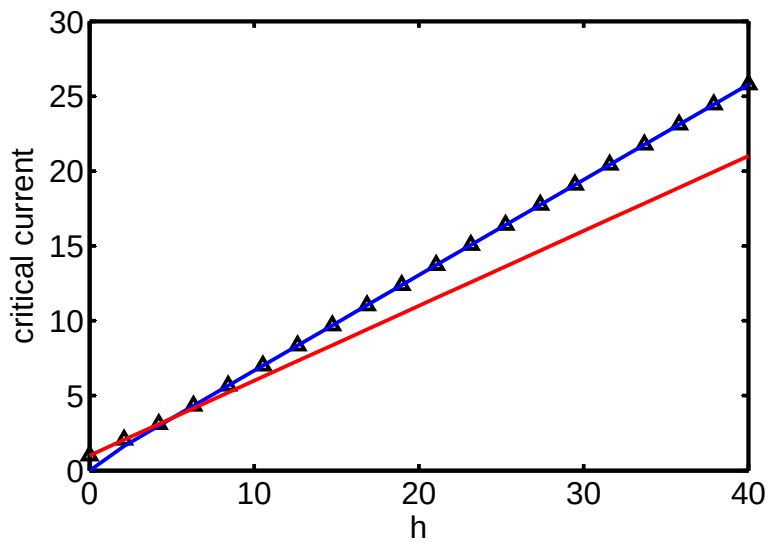

Figure 3.10: Critical current $\overline{\mathcal{I}}_{\rm c}/\alpha H_{\rm x}$ (black, triangles) as a function of $h = H_{\rm z}/H_{\rm x}$, calculated using Eqn. (3.12), along with $\overline{\mathcal{I}}_{\rm c}(0)$ (red) and $\overline{\mathcal{I}}_{\rm c}(E_{\rm b})$ (blue) calculated from Eqs. (3.13).

3.4.3 Switching time

Equation (3.8) can also be used to calculate the deterministic switching time for a given value of $\overline{\mathcal{I}}_{\rm s}$. Using the relation $dt = dE/\dot{E}$ one finds

$$t_{\rm sw}(E_0) = \int_{E_0}^{E_{\rm b}} \frac{dE}{\dot{E}} = \int_{E_0}^{E_{\rm b}} \frac{dE}{\overline{\mathcal{I}}_{\rm s}\overline{V}_{\rm x}(E) - \alpha U(E)}\,, \tag{3.14}$$

where E_0 is the initial energy of the free layer prior to turning on the spin-current and $E_{\rm b}$, recall, is the height of the energy barrier. Using the local critical current $\overline{\mathcal{I}}_{\rm c}$ Eqn.

(3.14) can be rewritten as

$$t_{\rm sw}(E_0) = \int_{E_0}^{E_{\rm b}} \frac{dE}{(\overline{\mathcal{I}}_{\rm s} - \overline{\mathcal{I}}_{\rm c}(E))\overline{V}_{\rm x}(E)} \,. \tag{3.15}$$

This means for cases where the local critical current remains roughly constant, $\overline{\mathcal{I}}_{\rm c}(E) \simeq \overline{\mathcal{I}}_{\rm c}$, such as for free layers with strong easy-plane anisotropy, the switching time goes as $t_{\rm sw} \propto (\overline{\mathcal{I}}_{\rm s} - \overline{\mathcal{I}}_{\rm c})^{-1}$. This dependence of the switching time on the critical current is well established in theoretical [94] and experimental literature [62, 99] for currents above the critical current.

3.5 Joule heat minimization

With the theoretical description developed in the previous sections in hand, I now turn to the underlying thrust of this thesis: optimizing the efficiency of ST switching. The issue at hand is as follows: to make switching times progressively shorter, larger and larger spin-current strengths are needed; see Eqn. (3.15). This leads to excessive Joule heat losses $\propto \int dt\, \overline{\mathcal{I}}_{\rm s}^2(t)$. On the other hand, decreasing the spin-current leads to longer switching times, which in turn may again increase heating due to the long time needed to complete the switch. One may expect that there is an optimal spin-current protocol, $\overline{\mathcal{I}}_{\rm opt}$, which minimizes the heating losses.

To find such a strategy, I look for strategies that satisfy $\partial_{\overline{\mathcal{I}}_{\rm s}} J = 0$, where

$$J(\overline{\mathcal{I}}_{\rm s}) = \int_0^{t_{\rm DC}} dt R(\mathbf{m}(t)) \overline{\mathcal{I}}_{\rm s}{}^2(t) \tag{3.16}$$

is the total energy loss due to Joule heating and $R(\mathbf{m})$ is a resistance that depends on the direction of the magnetization relative to the direction of the reference layer $\mathbf{m}_{\rm p}$. The form of this resistance is well approximated by

$$R(\mathbf{m}) = R_{\rm ave} - \Delta R(\mathbf{m} \cdot \mathbf{m}_{\rm p}) \,, \tag{3.17}$$

where $R_{\rm ave} = (R_{\rm AP} + R_{\rm P})/2$, $\Delta R = (R_{\rm AP} - R_{\rm P})/2$, and $R_{P(AP)}$ is the resistance of the MTJ in the parallel(antiparallel) orientation [100]. In practice this resistance varies little through the switching process [101, 102], both because the change in resistance tends to be small ($\Delta R \ll R_{\rm ave}$) and because the free layer tends to spend most of

its time through the switching process at low energies where the angle between the free layer magnetization and the reference layer is small. As a result, the JHL may be approximated to good accuracy by taking $R(\mathbf{M}) = R$ through the entire switching process. This gives for the total JHL

$$J = \int_0^{t_{\mathrm{DC}}} dt R \overline{\mathcal{I}}_{\mathrm{s}}{}^2(t)\,. \tag{3.18}$$

Equation (3.18) can also be written in terms of energy E by noting $dt = dE/\dot{E}$,

$$J(\overline{\mathcal{I}}_{\mathrm{s}}) = \int_{E_0}^{E_{\mathrm{b}}} dE \frac{R\overline{\mathcal{I}}_{\mathrm{s}}{}^2}{\dot{E}}\,. \tag{3.19}$$

Here the integral is a path integral along the energy trajectory of the free layer and E_0 is the initial energy taken to be the thermal equilibrium energy.

Taking the partial derivative of Eqn. (3.19) with respect to $\overline{\mathcal{I}}_{\mathrm{s}}$, using Eqn. (3.8), and setting the result equal to zero gives:

$$0 = \int_{E_0}^{E_{\mathrm{b}}} dE \frac{R\overline{\mathcal{I}}_{\mathrm{s}}}{\dot{E}^2} \left(\overline{\mathcal{I}}_{\mathrm{s}}\overline{V}_{\mathrm{x}}(E) - 2\alpha\, U(E)\right)\,, \tag{3.20}$$

which $\overline{\mathcal{I}}_{\mathrm{s}}$ must satisfy to minimize the Joule heat loss. Here recall U and $\overline{V}_{\mathrm{x}}$ are the φ-averaged damping and ST forces acting on the energy of the free layer and are given by Eqs. (3.9). The leading factor R here has been left in for completeness.

Of course it must be pointed out that depending on the assumed form for the spin-current, i.e., how it behaves with time/energy, Eqn. (3.20) may be accompanied by additional optimization equations. For example, if one were to try and minimize the JHL using DC spin-current of the form $\overline{\mathcal{I}}_{\mathrm{s}}(t) = \overline{\mathcal{I}}_{\mathrm{s}} + \overline{\mathcal{I}}_{\mathrm{s}}'\, t$, an additional partial derivative equation would be needed to optimize with respect to $\overline{\mathcal{I}}_{\mathrm{s}}'$. The particular form of Eqn. (3.20) is such that it is the optimization equation for square pulses, i.e., $\overline{\mathcal{I}}_{\mathrm{s}}$ held constant for the duration of the pulse, and for the case where no restrictions are place on the energy/time dependence of $\overline{\mathcal{I}}_{\mathrm{s}}$. In the following sections I cover both of these cases, starting with the case where no restrictions are placed on $\overline{\mathcal{I}}_{\mathrm{s}}$.

3.5.1 Optimal DC spin-current protocol: analytic

Looking at Eqn. (3.20) one can image an infinite number of spin-current strategies that may satisfy it. There is, however, one clear solution which makes the quantity inside

the integral on the RHS exactly equal to zero regardless of the energy. One may indeed check that

$$\overline{\mathcal{I}}_{\mathrm{opt}}(E) = 2\,\overline{\mathcal{I}}_{\mathrm{c}}(E) \tag{3.21}$$

satisfies this condition when inserted into Eqn. (3.20). This solution is of particular importance to the question of optimization because it represents the DC spin-current strategy that gives the global minimum JHL for switching using a DC spin-current. That this gives the global minimum JHL for a DC spin-current comes from the fact that it remains the optimal protocol regardless of the upper and lower limits of integration. This means that at every point along the switching process it minimizes the JHL.

One may immediately notice the optimal protocol is to apply a current that is exactly twice the local critical current of the free layer throughout the switching process. Further significance for this optimal protocol can be found by inserting Eqn. (3.21) into Eqn. (3.8) for the spin-current. Doing so, the energy equation of motion takes the form

$$\dot{E} = +\alpha U(E)\,. \tag{3.22}$$

This is exactly the same as in Eqn. (3.4) *without* the external spin-current $\overline{\mathcal{I}}_{\mathrm{s}}$, but with the time being *reversed*. This means *the optimal current protocol is such that it exactly time-reverses the purely relaxational trajectory of an isolated system.* Such a relaxation trajectory must be thought of as starting at the energy maximum E_{b} (i.e., the switching point) and winding down towards the energy minimum at E_0.

Placing Eqs. (3.21) and (3.22) into Eqn. (3.19), the JHL associated with the optimal DC switching protocol becomes

$$J(\overline{\mathcal{I}}_{\mathrm{s}}) = \alpha R \int_{E_0}^{E_{\mathrm{b}}} dE \frac{U(E)}{\overline{V}_{\mathrm{x}}^2(E)}\,. \tag{3.23}$$

Since the volatility of a MTJ is directly related to the height of the energy barrier E_{b}, i.e.H_{x}, Eqn. (3.23) can be used to compare the optimal JHL for free layers with various anisotropy configurations and equal values of E_{b}. Figure 3.11 plots the JHL, calculated numerically using Eqn. (3.23), for a wide range of H_{z} values with fixed H_{x}. Clearly the uniaxial case is optimal. This is in line with experimental results in Ref. [99] on free layers with perpendicular magnetic anisotropy. Notice the JHL is essentially linear in

H_z. For a free layer with uniaxial anisotropy, U and $\overline{V}_x$ can be solved for exactly yielding

$$U(E) = 2\gamma H_x E \left(\frac{E_b - E}{E_b} \right) ; \qquad \overline{V}_x = 2\gamma E \left(\frac{E_b - E}{E_b} \right)^{1/2} . \tag{3.24}$$

Plugging these into Eqn. (3.23) gives $J_{opt} = \alpha R E_b \ln(E_b/E_0)/\gamma M_s$. For a free layer with strong easy-plane anisotropy, U and $\overline{V}_x$ can be approximated to leading order in energy as

$$U(E) \approx \gamma(2H_x + H_z)E ; \qquad \overline{V}_x \approx \gamma 2E . \tag{3.25}$$

Plugging these into Eqn. (3.23) gives $J_{opt} \approx \alpha R E_b (1 + h/2) \ln(E_b/E_0)/2\gamma M_s$ for the JHL where $h = H_z/H_x$. This suggests a general relation for the optimal JHL as a function of free layer anisotropy

$$J_{opt} \approx \frac{\alpha R E_b}{\gamma M_s} \left(1 + \frac{h}{2} \right) \ln \left(\frac{E_b}{E_0} \right) . \tag{3.26}$$

Figure 3.11 plots this relation along with numerical solutions to Eqn. (3.23). As one can see, they are in good agreement. For detailed derivations of Eqs. (3.24) and (3.25), see Appendix B.2.

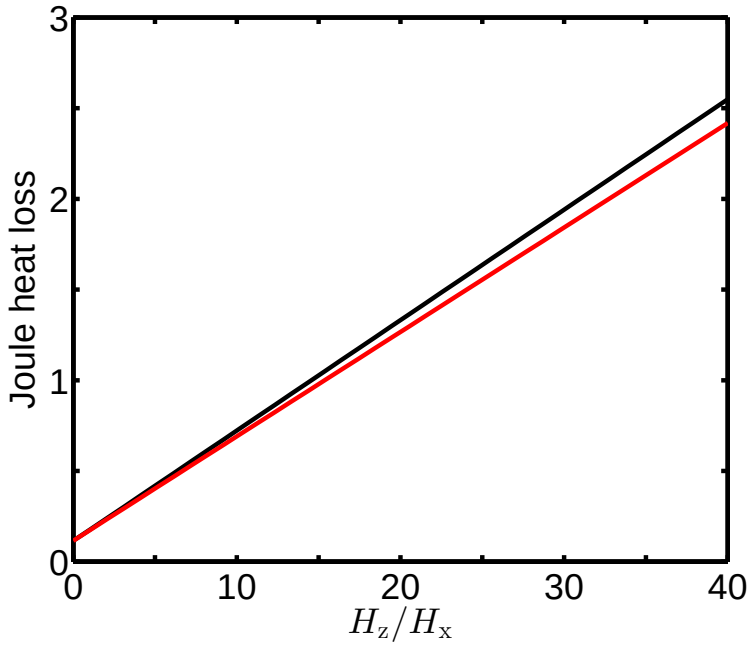

Figure 3.11: Minimum JHL in arbitrary units vs. H_z. Calculated numerically using Eqn. (3.23) (black) and Eqn. (3.26) (red).

3.5.2 Practical solutions

The spin-current strategy discussed in the previous section for the global minimum JHL using a DC spin-current is not always practical. For instance, for free layers with uniaxial anisotropy, the local critical current $\overline{\mathcal{I}}_c(E)$ goes to zero as the energy approaches the energy barrier (see Fig. 3.10). This causes the associated switching time to diverge. So while the switching strategy may indeed be energy efficient, it will take infinitely long to complete. Furthermore, applying any energy dependent spin-current strategy becomes problematic for practical devices which are subject to thermal fluctuations. These thermal fluctuations ensure the free layer energy deviates from the deterministic energy trajectory calculated using Eqn. (3.8). For these reasons, it is also important to look at optimizing more realistic current pulse forms.

Here I consider the simplest spin-current strategy, a square current pulse, i.e., $\overline{\mathcal{I}}_s$ constant. Even for this simple spin-current pulse form, finding the optimal protocol analytically is prohibitively difficult. As a result, is it significantly faster and easier

to calculate the optimal protocol by solving Eqn. (3.20) numerically for $\overline{\mathcal{I}}_{\mathrm{s}}$. To aid in such numerical approaches, Eqn. (3.20) can be used to significantly narrow the range of spin-current values that may satisfy it.

Immediately one may note that $\overline{\mathcal{I}}_{\mathrm{s}}$ must be large enough to ensure $\dot{E}(E) > 0$ throughout the range of integration. This means the optimal current must be greater than the critical current, $\overline{\mathcal{I}}_{\mathrm{opt}} > \overline{\mathcal{I}}_{\mathrm{c}}$, given by Eqn. (3.13). The range of possibly values for $\overline{\mathcal{I}}_{\mathrm{opt}}$ can be narrowed further by noting that $\dot{E}^2$ and $\overline{V}_{\mathrm{x}}$ are entirely positive over the range of integration. As a result, Eqn. (3.20) may only have solutions provided $\overline{\mathcal{I}}_{\mathrm{s}} - 2\overline{\mathcal{I}}_{\mathrm{c}}(E)$ is not entirely positive or negative over the range of integration, $E_0 < E < E_{\mathrm{b}}$. This means the DC spin-current must be between twice the smallest and twice largest DC local critical current. These conditions place upper and lower bounds on the optimal DC spin-current such that

$$\max\left\{\overline{\mathcal{I}}_{\mathrm{c,min}}, \overline{\mathcal{I}}_{\mathrm{c}}\right\} < \overline{\mathcal{I}}_{\mathrm{opt}} < 2\overline{\mathcal{I}}_{\mathrm{c}}\,, \tag{3.27}$$

where $\overline{\mathcal{I}}_{\mathrm{c,min}}$ is the minimum local critical current given by

$$\overline{\mathcal{I}}_{\mathrm{c,min}} = 2\min\left\{\overline{\mathcal{I}}_{\mathrm{c}}(E)|E_0 < E < E_{\mathrm{b}}\right\}\,. \tag{3.28}$$

For free layers with strong easy-plane anisotropy, these constraints result in a very narrow range of possible values for the optimal spin-current such that $\overline{\mathcal{I}}_{\mathrm{opt}} \simeq 2\overline{\mathcal{I}}_{\mathrm{c}}$. So, the optimal DC spin-current protocol for a square current pulse is to use a spin-current approximately twice the critical current. This result is confirmed in the experimental results of Refs. [62, 103]. This is shown in Fig. 3.12 which plots Joule heating as a function of the spin-current strength for various switching probability levels for a free layer with strong easy-plane anisotropy and $T = 300$K. At low switching probabilities $\overline{\mathcal{I}}_{\mathrm{opt}} \lesssim 2\overline{\mathcal{I}}_{\mathrm{c}}$ due to large fluctuations dominating the early switching behavior. However, at switching probabilities nearing 100% we see the predicted $\overline{\mathcal{I}}_{\mathrm{opt}} \approx 2\overline{\mathcal{I}}_{\mathrm{c}}$.

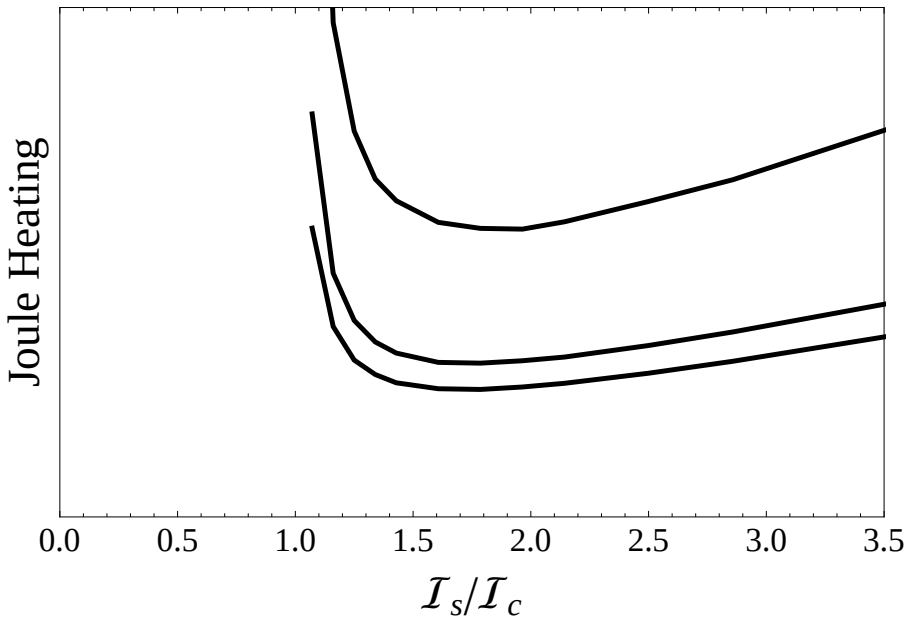

Figure 3.12: Simulated JHL in arbitrary units vs. spin-current strength for various confidence levels p. From top to bottom, $p = 0.99$, $p = 0.5$, $p = 0.2$. Here $\alpha = 0.015$, $H_\mathrm{x} = 0.033 M_\mathrm{s}$, $H_\mathrm{z} = M_\mathrm{s}$, and $T = 300\mathrm{K}$.

The optimal pulse time associated with this strategy depend on the desired switching probability as well. For MTJs without hard-axis or easy-plane spin-current polarizations, the distribution of the switching times strongly depends on the equilibrium thermal distribution of initial energy $\propto e^{-E_0/k_\mathrm{B}T}$ and the deterministic switching time, Eqn. (3.14). Since the distribution of initial energies is $\propto \alpha^{-1}\ln(E_\mathrm{b}/E_0)$, this means any pulse of a finite duration achieves switching only with a certain probability $p < 1$. If this probability, i.e., error tolerance, is specified such that $1 - p \ll 1$, all realizations with $E_0 \geq k_\mathrm{B}T(1-p)$ should undergo the switch. This dictates that the duration of the optimal current pulse scales as

$$t_\mathrm{opt} \approx \frac{t_0}{\alpha}\,\ln\left(\frac{E_\mathrm{b}}{k_\mathrm{B}T(1-p)}\right)\,, \tag{3.29}$$

where $t_0 = (\gamma M_\mathrm{s})^{-1}$. This result is shown in Fig. 3.13 for higher switching probabilities and is in good agreement with the simulated data. Similar probabilistic switching behavior is seen in Refs. [53, 52].

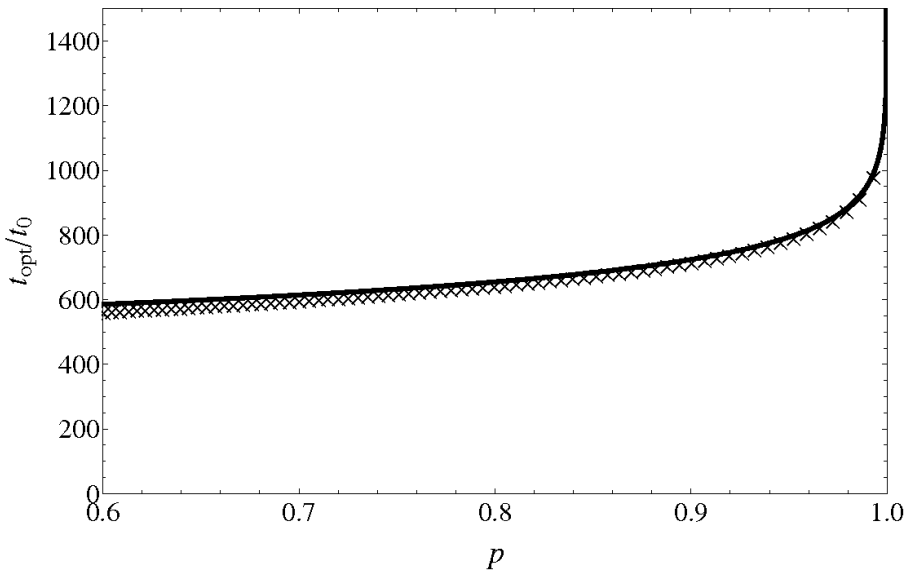

Figure 3.13: Simulated optimal switching time (crosses) and Eqn. (3.29)(black line) as a function of the confidence level, p. Here $\alpha = 0.015$, $H_{\rm x} = 0.033M_{\rm s}$, $H_{\rm z} = M_{\rm s}$, $T = 300$K, and $\overline{\mathcal{I}}_{\rm s} = 2\overline{\mathcal{I}}_{\rm c}$.

3.6 DC switching with easy-plane polarized spin-currents

The theoretical description developed in this chapter is a powerful tools for understanding and optimizing ST switching using DC currents. However, as one may recall, in using this description I have ignored ST switching in perpendicular MTJs with strong easy-plane anisotropy. One may recall that for these MTJs, switching times were much shorter than those of collinear MTJs (see Figs. 3.2 and 3.4), with switching times faster less than the precessional period of the free layer. These perpendicular MTJs also exhibited a strong dependence on the pulse time.

To explore the differences in switching behavior between perpendicular MTJs with strong easy-plane anisotropy and collinear MTJ Fig. 3.14 plots simulated switching probabilities as a function of spin-current strength and inverse pulse time. Note that while both collinear MTJs exhibit two distinct regions of high and low switching probability, the perpendicular MTJ has several regions that alternate between high and low switching probability. These alternating regions are seen experimentally in Ref. [87] and

via micromagnetic simulations in Refs. [63, 104, 105]. The dramatic improvement in switching speed for the perpendicularly configured MTJ eliminates the time-scale separation between φ and E. This means one may not average Eqs. (3.4) and (3.6) about φ; thus the theory developed in this chapter is inadequate for discussing and optimizing this kind of DC ST switching.

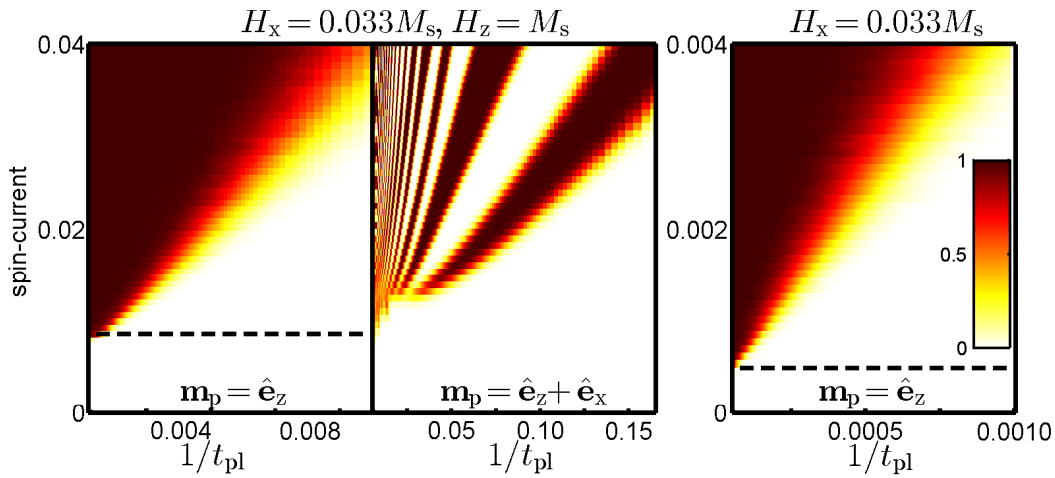

Figure 3.14: Switching probability as a function of spin-current strength (in units of M_s) and inverse pulse time (in units of γM_s) for a free layer with strong easy-plane anisotropy (left and center) and uniaxial anisotropy (right). Here $\alpha = 0.015$ and $T = 300$K. Dashed black lines represent critical current calculated using Eqn. (3.13).

As established in Sec. 3.5.1, for $\hat{\mathbf{e}}_x$-polarized spin-currents, switching is most efficient for free layers with uniaxial anisotropy. This means for $\hat{\mathbf{e}}_z$-polarized spin-currents to be useful, the energy loss from Joule heating must be comparable to that of DC uniaxial free layers with equal energy barriers, i.e.equal values of H_x. Calculating the JHL for the devices simulated in Fig. 3.14 using Eqn. (3.18), one finds this is indeed the case (see Fig. 3.15). Notice that for the $\hat{\mathbf{e}}_z$-polarized spin-current, the JHL is reduced by more than an order of magnitude over the collinear MTJ with strong easy-plane anisotropy. In fact, the JHL is improved such that it is nearly equal to that of the uniaxial free layer with the same energy barrier E_b.

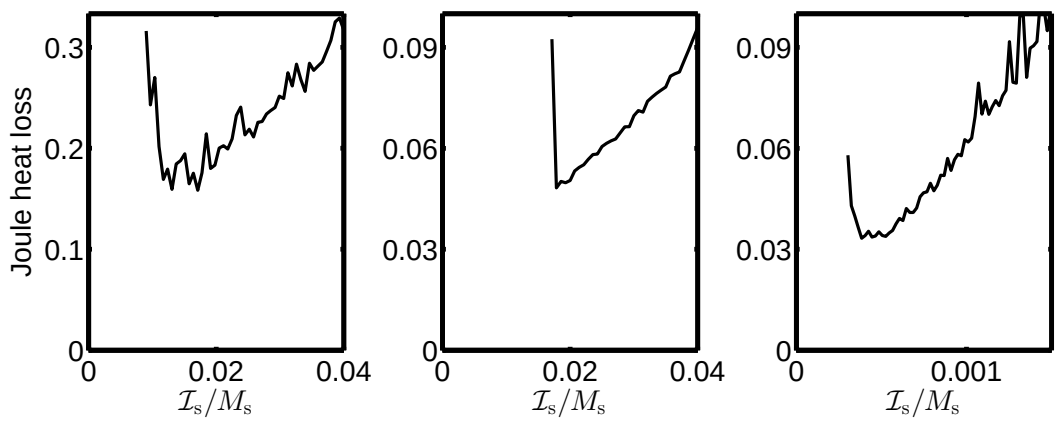

Figure 3.15: JHL as a function of spin-current strength for free layers anisotropy and spin-polarization configurations: $H_x = 0.033M_s$, $H_z = M_s$, and $\mathbf{m}_p = \hat{\mathbf{e}}_x$ (left); $H_x = 0.033M_s$, $H_z = M_s$, and $\mathbf{m}_p = \hat{\mathbf{e}}_x + \hat{\mathbf{e}}_z$ (center); $H_x = 0.033M_s$, $H_z = 0$, and $\mathbf{m}_p = \hat{\mathbf{e}}_x$ (right). Here $\alpha = 0.015$ and $T = 300$K. For all cases only switching probabilities above 95% were considered.

This improvement in ST efficiency is made all the more impressive when considering the pulse times corresponding to the JHL values plotted in Fig. 3.15. As Fig. 3.16 shows, the optimal switching pulse time for the perpendicular MTJ with strong easy-plane anisotropy is nearly two orders of magnitude faster than that of the collinear MTJ with strong easy-plane anisotropy, and nearly three orders of magnitude faster than that of the uniaxial free layer. From these results the $\hat{\mathbf{e}}_z$-polarized DC spin-current is clearly the best choice. In the following chapter I will discuss ways of improving the efficiency of this method further by using AC spin-currents.

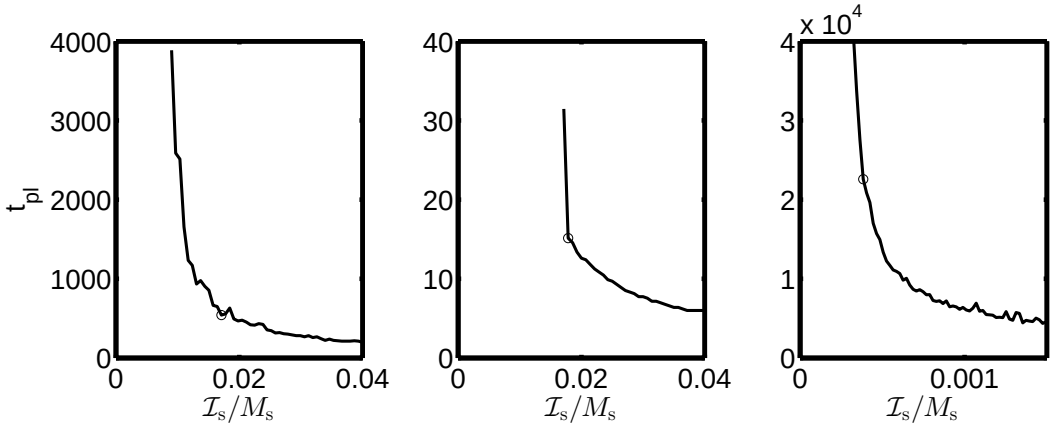

Figure 3.16: Pulse times, in units of $(\gamma M_s)^{-1}$, as a function of spin-current strength corresponding to the JHL values shown in Fig. 3.15. Pulse times associated with minimum JHL for each free layer configuration are marked with a circle.

Chapter 4

AC spin-torque

4.1 Introduction

In this chapter I explore the effects of AC spin-currents on the free layer magnetization of a MTJ. In keeping with the format of the previous chapter I begin by presenting simulations of a free layer under the effect of AC spin-currents with different spin-current polarizations. From there I employ the same energy/angle change of variable presented in chapter 3 to describe the AC response of the free layer. The resulting equations of motion are then averaged with respect to the fast precessional angle, resulting in two equations of motion which describe the system as a strongly non-linear oscillator. The switching characteristics of AC spin-current strategies are explained using this description. Finally, this description is used to minimize the JHL associated with switching using an AC spin-current.

The desire to look at ST switching using AC spin-currents is motivated by the results of section 3.6, where switching using DC perpendicular spin-currents was shown to be inhibited by the precessional motion of the magnetization about the easy-axis. One will recall these precessions cause the ST from the spin-current polarized along the easy-plane axis to self-cancel as the magnetization orbits the effective field. One can imagine that a properly applied AC spin-current could prevent this self-canceling and allow the easy-plane polarized spin-torque to provide a net positive torque on the free layer. Numerous experimental and numerical works over the last five years have shown AC spin-currents can produce a resonant response in MTJ free layers [106, 107, 108,

109, 110, 111]. Therefore, given the right phase difference between the AC signal and the magnetic response, the AC spin-current may prevent this self-canceling and allow switching to occur. Since this would remove the limit on the switching time present in DC perpendicular switching, this may result in switching with lower currents and JHL than in the DC case. This approach is further motivated by the experimental work of [60], which shows an AC spin-current pulse followed by a DC pulse can facilitate switching by inducing a resonant response in the free layer driving, it to a higher energy state.

4.2 Numerical simulations of AC ST

In this section, I present numerical simulations showing how AC spin-currents may produce switching in free layers of MTJs. These simulations were performed by numerically integrating the LLGS Eqn. (2.1) from chapter 2 with respect to time. The spin-current in these simulations is defined by the polarization vector $\mathbf{m}_\mathrm{p}$, the strength of the spin-current $\mathcal{I}_\mathrm{s}$, and the AC spin-current frequency ω such that $\vec{\mathcal{I}}_\mathrm{s}(t) = \mathcal{I}_\mathrm{s}\sin(\omega t)\mathbf{m}_\mathrm{p}$.

As will quickly become clear, the nature of AC spin-torque switching is significantly more complex than its DC counterpart. For switching using AC spin-currents, not only does the likelihood of switching depend strongly on the polarization $\mathbf{m}_\mathrm{p}$ and spin-current strength $\mathcal{I}_\mathrm{s}$, but also it is strongly dependent on the duration of the spin-current pulse and on the frequency of the AC signal. As a result of this added complexity, I first present the free layer responses to various spin-current polarizations and driving frequencies in the absence of switching before moving on to the switching dynamics.

Since the thrust of this thesis is about the optimization of ST switching, i.e., minimizing the JHL, I feel I must first provide some evidence that such AC spin-current strategies may result in lower JHL than found in chapter 3 with DC spin-current strategies. To this end, Fig. 4.1 plots the minimum JHL as a function of spin-current strength $\mathcal{I}_\mathrm{s}$ for the system with strong easy-plane anisotropy discussed in depth in chapter 3. Notice, not only is the minimum JHL nearly a factor of two lower than it is for the optimal DC strategy, but also that switching takes place at currents well below the critical current of the DC approach. Such switching below the DC critical current is observed in Ref. [112] for AC spin-currents superimposed onto a DC spin-current pulse.

In order to ensure the AC results shown in Fig. 4.1 constituted a strategy that could be applied to practical devices, only parameters resulting in switching probabilities above 99% were used to calculate the optimal JHL values at each current.

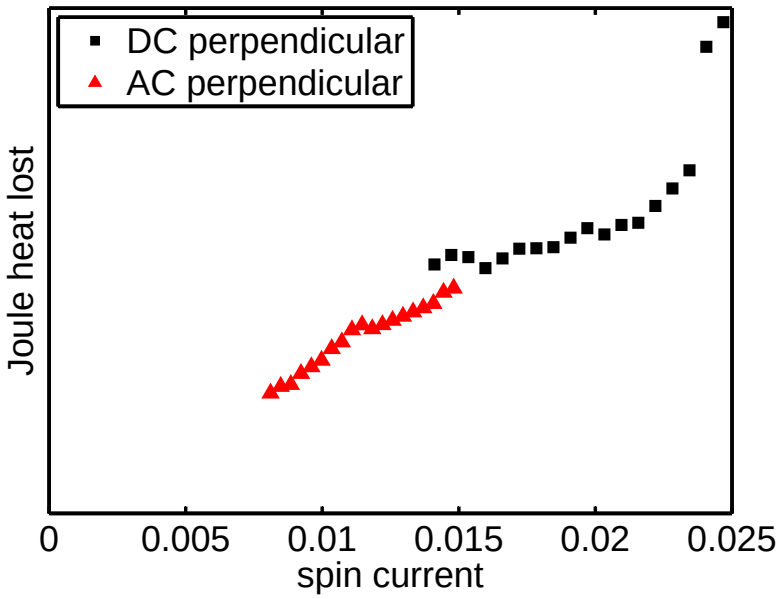

Figure 4.1: Simulated optimal Joule heat lost during switching process in arbitrary units as a function of spin-current amplitude ($\mathcal{I}_s/M_s$) for DC (black squares) and AC (red triangles) spin-current methods with $\mathbf{m}_p = \hat{\mathbf{e}}_x + \hat{\mathbf{e}}_z$. For AC simulations, frequencies $\omega/2\pi$ ranged from $0 - 0.03\gamma M_s$ with pulse times $t_{pl} = n(2\pi/\omega)$ where n ranged from $0.5 - 4$ to find the optimal regime. For both AC and DC, cases only combinations of spin-current $\mathcal{I}_s$ and AC frequency ω that resulted in switching probabilities above 99% were are displayed. Same parameters as in Fig. 4.4.

4.2.1 Free layer response: non-switching events

To illustrate how the free layer responds to an AC spin-current when switching does not occur, numerical simulations of the LLGS Eqn. (2.1) were performed with $\mathcal{I}_s(t) = \mathcal{I}_s \sin(\omega t)$ for each of the three cardinal spin-current polarizations, i.e., polarized along the free layer easy-axis, hard-axis, and easy-plane directions. As in chapter 3, each polarization was applied to a free layer with uniaxial anisotropy as well as one with

strong easy-plane anisotropy. The free layer energy as a function of time is shown in Fig. 4.2 for these simulations. Simulations showing the effect of the AC spin-current frequency ω are discussed later in this section.

Upon inspection of Fig. 4.2 one may immediately notice that the $\hat{\mathbf{e}}_{\mathrm{x}}$-polarized (easy-axis) AC spin-current produces no response in both free layer anisotropy configurations. Here the oscillations of the spin-current cause the $\hat{\mathbf{e}}_{\mathrm{x}}$-polarized ST to self-cancel over each period of oscillation. This self-canceling is similar to the self-canceling of the $\hat{\mathbf{e}}_{\mathrm{y}}$- and $\hat{\mathbf{e}}_{\mathrm{z}}$-polarized DC STs in chapter 3. One may also recall from the previous chapter that the ST from $\hat{\mathbf{e}}_{\mathrm{x}}$-polarized spin-currents is weakest when the free layer magnetization is along the easy-axis. This means any gains or losses in free layer energy from the $\hat{\mathbf{e}}_{\mathrm{x}}$-polarized portion of the spin-current will remain small so long as the free layer remains near the energy minimum.

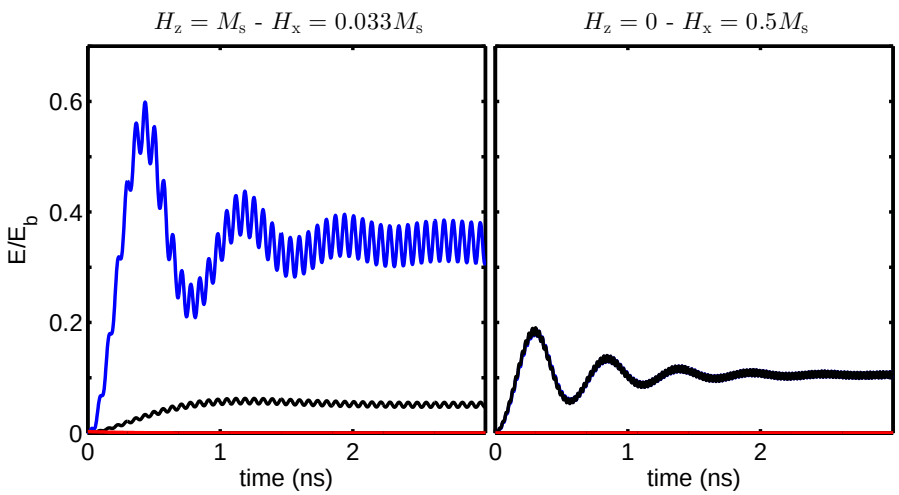

Figure 4.2: Free layer energy vs. time under the influence of several AC spin-currents. The spin-current polarizations shown in each are $\mathbf{m}_{\mathrm{p}} = \hat{\mathbf{e}}_{\mathrm{x}}$ (red), $\mathbf{m}_{\mathrm{p}} = \hat{\mathbf{e}}_{\mathrm{y}}$ (black), and $\mathbf{m}_{\mathrm{p}} = \hat{\mathbf{e}}_{\mathrm{z}}$ (blue). Free layer with $H_{\mathrm{x}} = 0.033M_{\mathrm{s}}$, $H_{\mathrm{z}} = M_{\mathrm{s}}$, and $\mathcal{I}_{\mathrm{s}} = 0.004M_{\mathrm{s}}$ (left) and with $H_{\mathrm{x}} = 0.5M_{\mathrm{s}}$, $H_{\mathrm{z}} = 0$, and $\mathcal{I}_{\mathrm{s}} = 0.018M_{\mathrm{s}}$ (right). Here $T = 0$ and $\omega = \Omega_0$, i.e., the zero-energy natural frequency of the free layer.

For spin-currents polarized along the $\hat{\mathbf{e}}_{\mathrm{y}}$ and $\hat{\mathbf{e}}_{\mathrm{z}}$ directions, the response quite strong. For the uniaxial free layer, the $\hat{\mathbf{e}}_{\mathrm{y}}$- and $\hat{\mathbf{e}}_{\mathrm{z}}$-polarized spin-currents produce identical

free layer responses due to the rotational symmetry of the system about the easy-axis $\hat{\mathbf{e}}_{\mathrm{x}}$ direction. However, for the free layer with strong easy-plane anisotropy, the energy response from the $\hat{\mathbf{e}}_{\mathrm{z}}$-polarized spin-current is significantly stronger. That the maximum free layer energy during the $\hat{\mathbf{e}}_{\mathrm{z}}$-polarized AC pulse exceeds half the barrier height is made more impressive by noting the strength of the spin-current used to produce it. Here the strength of the spin-current is $\mathcal{I}_{\mathrm{s}} = 0.004M_{\mathrm{s}}$, less than half the DC critical current $\mathcal{I}_{\mathrm{c}} \simeq 0.009M_{\mathrm{s}}$ calculated in chapter 3 for the same anisotropy configuration. For the free layer with uniaxial anisotropy, the strength of the spin-current $\mathcal{I}_{\mathrm{s}} = 0.018M_{\mathrm{s}}$ is well above the corresponding DC critical current value $\mathcal{I}_{\mathrm{c}} = 0.075M_{\mathrm{s}}$; thus it appears AC spin-currents are unlikely to improve the efficiency of free layers with weak easy-plane anisotropy.

The shape of the energy trajectories plotted in Fig. 4.2 are also of interest. The energy trajectories for the $\hat{\mathbf{e}}_{\mathrm{y}}$- and $\hat{\mathbf{e}}_{\mathrm{z}}$-polarized spin-currents look like those of a damped oscillator, overshooting the equilibrium value before gradually decaying to it over several oscillations. One will also notice there is practically no incubation time. The free layer energy appears to rise almost linearly in time from its initial value, E_0.

The dependence of the free layer response on the frequency of the AC signal ω can be seen in Fig. 4.3 for the free layer with easy-plane anisotropy considered previously. Note for the frequency just below the naturally frequency $\omega = 0.88\Omega_0$, the maximum energy overshoot and the final equilibrium energy are significantly higher than in the case with $\omega = \Omega_0$; recall Ω_0 is the zero-energy natural precessional frequency of the free layer calculated using Eqn. (3.1). However, for the lowest AC frequency shown, $\omega = 0.73\Omega_0$, the maximum energy and equilibrium energy are dramatically reduced. These results suggests an optimal frequency value exists somewhere in this range. The specific nature of this frequency dependence is discussed in the theoretical section that follows.

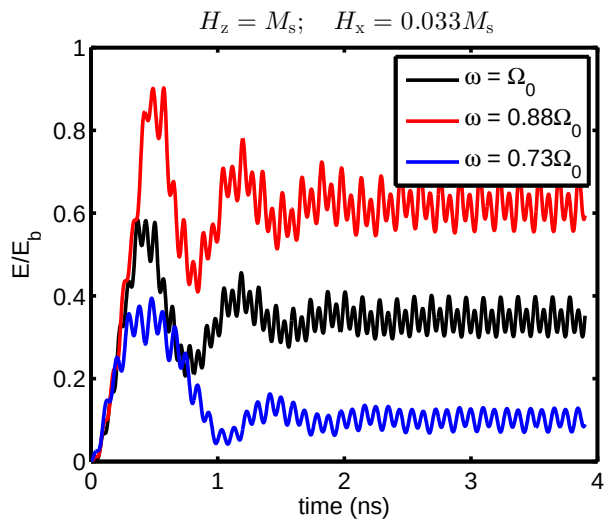

Figure 4.3: Free layer energy vs. time under the effect of AC spin-currents for three different AC frequencies for free layer with $H_x = 0.033M_s$, $H_z = M_s$, $\mathcal{I}_s = 0.004M_s$, $T = 0$, and $\mathbf{m}_p = \hat{\mathbf{e}}_z$.

4.2.2 AC ST switching

With this basic understanding of how the polarization and frequency of an AC spin-current affects the energy of the free layer, we now turn our attention to simulations of AC spin-current induced switching. Given the poor response of the uniaxial free layer to all of the AC spin-current polarizations, for the rest of this I will discuss only switching behavior for free layers with strong easy-plane anisotropy and spin-currents polarized along the easy-plane $\hat{\mathbf{e}}_z$-direction. Specifically, I will focus on simulations of the free layer with $H_z = M_s$, $H_x = 0.033M_s$, and $\mathbf{m}_p = \hat{\mathbf{e}}_x + \hat{\mathbf{e}}_z$. Here I have included $\hat{\mathbf{e}}_x$ in the spin-current polarization to reflect the impact of the MTJ reference layer on the switching dynamics.

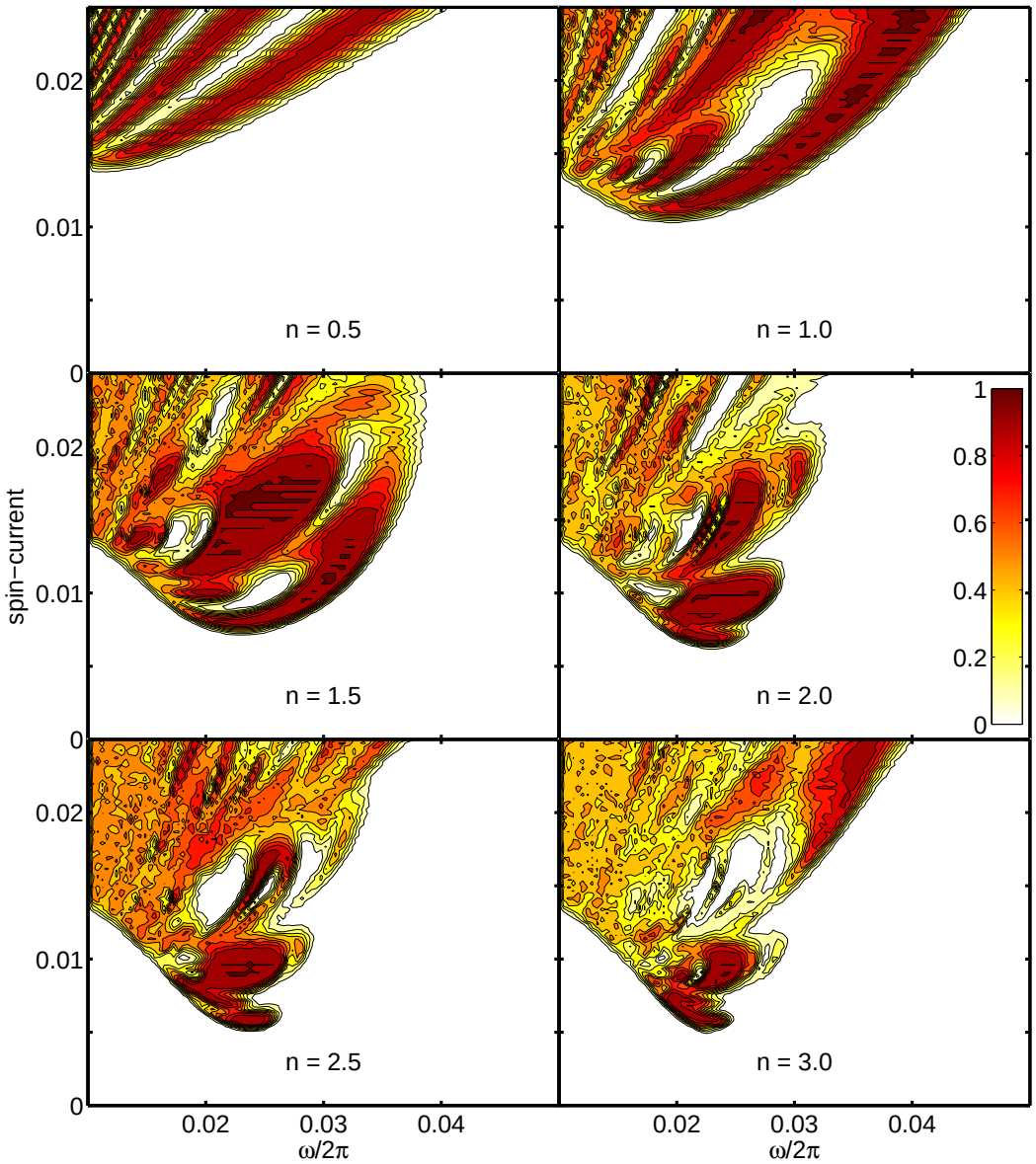

Figure 4.4: Switching probability of perpendicular MTJ as a function of AC spin-current amplitude ($\mathcal{I}_s/M_s$) and applied frequency ω (in units of γM_s) with pulse times $t_{pl} = n2\pi/\omega$. Here $H_z = M_s$, $H_x = 0.033M_s$, $\alpha = 0.015$, and $T = 300$K.

Figure 4.4 shows simulated switching probabilities as a function of spin-current strength $\mathcal{I}_{\mathrm{s}}$ and AC frequency ω for various pulse times t_{pl} for the free layer mentioned in the previous paragraph. For each frequency shown, the corresponding pulse times are $t_{\mathrm{pl}} = n(2\pi/\omega)$ where n varies from $0.5 - 3.0$ in half-integer steps with each figure corresponding to a specific value of n. Notice for $n = 0.5$ the switching probability looks qualitatively similar to the DC perpendicular switching probability in Fig. 3.14 with alternating high and low switching probability regions, each being roughly linear in $1/t_{\mathrm{pl}}$. This makes sense, as the spin-current pulse for $n = 0.5$ is effectively DC. That the spin-current has to ramp up and then down in strength over the pulse duration explains the higher critical current compared to the square pulse used in Fig. 3.14.

For $n = 1$ notice the rightmost high switching probability bands extends down allowing the free layer to switch at currents below the DC critical current, $\mathcal{I}_{\mathrm{c}} \simeq 0.01 M_{\mathrm{s}}$ (see Fig. 3.14). This reduction in critical current continues for $n > 1$ until a V-shaped switching region emerges for $n = 3$. Qualitatively similar switching behavior is observed in the experimental works of Ref. Chen11 and [113].

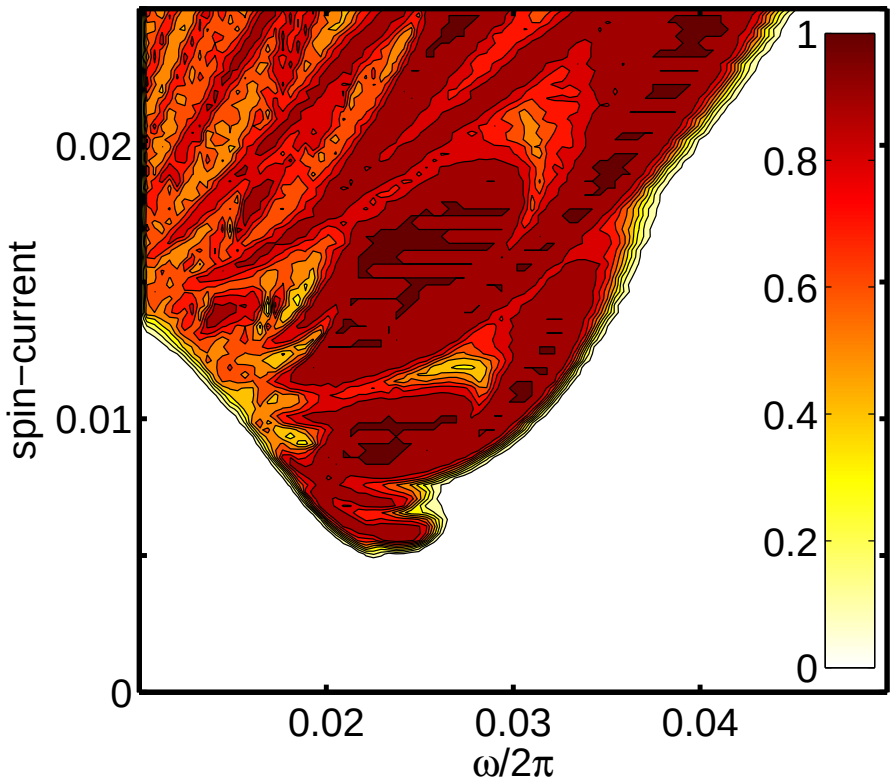

Figure 4.5: Composite switching probability created by overlaying the highest switching probabilities in Fig. 4.4.

The lakes of low switching probability at each value of n are a unique feature in AC ST switching. Figure 4.5 overlays each of the switching probability maps shown in Fig. 4.4 into a single figure to show the maximum switching probability achieved by each combination of $\mathcal{I}_{\mathrm{s}}$ and ω. Note that upon doing so the lakes vanish. This means the lakes of low switching probabilities shown in Fig. 4.5 correspond to islands of high switching probabilities at different pulse times. This behavior is illustrated more clearly in Fig. 4.6, which plots the switching probability as a function of time for a single combination of $\mathcal{I}_{\mathrm{s}}$ and ω. Indeed, the switching probability does oscillate between high and low values with a period on order of the initial switching time. With each successive oscillation, the switching probability moves closer towards 50%. Similar behavior is observed via micromagnetic simulations in Ref. [114] where AC spin-currents produce

hopping between meta-stable states.

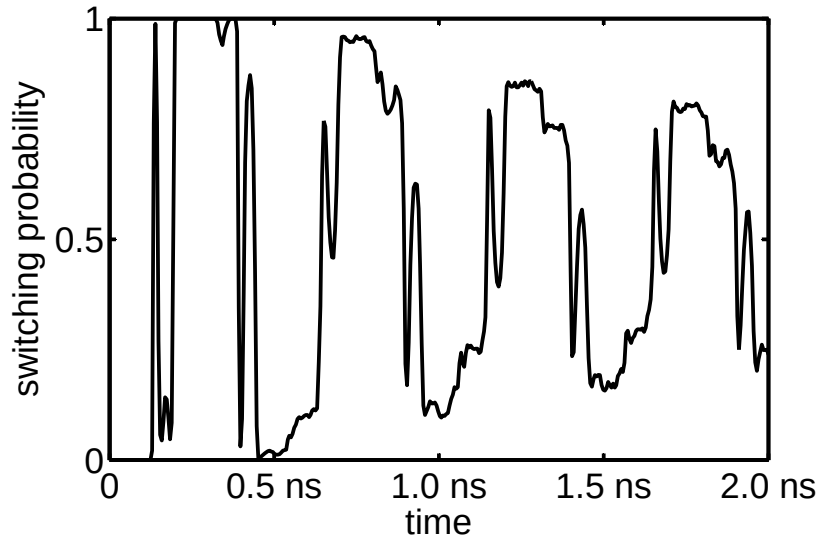

Figure 4.6: Switching probability as a function of pulse time for $\omega/2\pi = 0.024\gamma M_{\rm s}$ and $\mathcal{I}_{\rm s} = 0.015 M_{\rm s}$. All other parameters are the same as in Fig. 4.4.

4.3 Theoretical description: energy/angle coordinates

Just as in DC ST switching, in order for an AC spin-current to produce a switch the ST must first overcome damping. Therefore, it is again convenient to describe the dynamics of the free layer in terms of the energy angle pair, E and φ, presented in chapter 3 and defined implicitly by Eqs. (3.2). One may recall, the equations of motion for these new coordinates are

$$\begin{aligned} \dot{E} &= -\alpha U(E,\varphi) + \mathcal{I}_{\rm s}\sin(\omega t) V(E,\varphi)\,; \\ \dot{\varphi} &= \Omega(E) + \mathcal{I}_{\rm s}\sin(\omega t) W(E,\varphi)\,, \end{aligned} \tag{4.1}$$

c.f. Eqs. (3.4) and (3.6) with the AC spin-current $\mathcal{I}_{\rm s}\sin(\omega t)$ substituted in place of the DC spin-current $\mathcal{I}_{\rm s}$. Here recall $\Omega(E)$ is the energy-dependent natural precessional frequency of the free layer about the easy-axis, and the generalized forces U, V, and W

correspond to the effects of damping on E and the effects of ST on E and φ, respectively, and are given by Eqs. (3.5) and Eqn. (3.7), respectively. The strengths of the generalized forces listed in Eqs. (4.1) behave identically to those shown in section 3.3 (see Figs. 3.5 and 3.6).

From Sec. 4.2 we know the free layer tends to resonate with the spin-current for frequencies close to the natural frequency of the free layer and for spin-currents polarized in part along the $\hat{\mathbf{e}}_{\mathrm{z}}$ or $\hat{\mathbf{e}}_{\mathrm{y}}$ directions. This means the AC signal and the free layer angles can be linked by the relative phase between them, $\phi(t) = \varphi(t) - \omega t$. The time evolution for this phase is found by differentiating with respect to time, yielding $\dot{\phi} = \dot{\varphi} - \omega$. Substituting Eqn. (4.1) into this expression for $\dot{\varphi}$ gives the full equation of motion for the phase

$$\dot{\phi} = \Omega(E) - \omega + \mathcal{I}_{\mathrm{s}} \sin(\omega t) W(E, \varphi)\,. \tag{4.2}$$

Using Eqn. (4.2) along with the relation $\sin(\omega t) = \sin(\varphi - \phi) = \sin\varphi\cos\phi - \cos\varphi\sin\phi$, the explicit time dependence of Eqs. (4.1) and (4.2) can be removed completely.

4.4 Theoretical description: φ-averaged equations of motion

So long as the free layer remains in resonance with the AC spin-current, the free layer angle φ will precess near the resonance frequency. This means $\dot{\varphi} - \omega \ll \dot{\varphi}$ as $\dot{\varphi} \simeq \omega$ and thus the phase is a slow variable relative to the free layer angle, $\dot{\phi} \ll \dot{\varphi}$. From the simulations presented in section 4.2, the energy E is also a slow variable relative to φ; thus the time-scale separation present in chapter 3 when dealing with DC spin-currents is applicable here [91]. Performing this averaging on Eqs. (4.1) and (4.2) gives

$$\begin{aligned} \dot{E} &= -\alpha U(E) + \widetilde{\mathcal{I}}_{\mathrm{s}} \widetilde{V}_{\mathrm{y}}(E) \cos\phi - \widetilde{\mathcal{I}}_{\mathrm{s}} \widetilde{V}_{\mathrm{z}}(E) \sin\phi\,; \\ \dot{\phi} &= \Omega(E) - \omega + \widetilde{\mathcal{I}}_{\mathrm{s}} \widetilde{W}_{\mathrm{y}}(E) \sin\phi - \widetilde{\mathcal{I}}_{\mathrm{s}} \widetilde{W}_{\mathrm{z}}(E) \cos\phi\,. \end{aligned} \tag{4.3}$$

The two new φ-averaged generalized energy forces in Eqs. (4.3) are

$$\begin{aligned} \widetilde{V}_{\mathrm{y}}(E) &= \eta_{\mathrm{y}} \frac{\Omega(E)}{2\pi M_{\mathrm{s}}} \oint [d\mathbf{M} \times \mathbf{M}] \cdot \hat{\mathbf{e}}_{\mathrm{y}} \sin\varphi\,; \\ \widetilde{V}_{\mathrm{z}}(E) &= \eta_{\mathrm{z}} \frac{\Omega(E)}{2\pi M_{\mathrm{s}}} \oint [d\mathbf{M} \times \mathbf{M}] \cdot \hat{\mathbf{e}}_{\mathrm{z}} \cos\varphi\,, \end{aligned} \tag{4.4}$$

and the two new phase φ-averaged generalized forces are

$$\widetilde{W}_{\rm y}(E) = -\gamma M_{\rm s}\eta_{\rm y}\frac{\Omega^2(E)}{2\pi}\oint\frac{d\mathbf{M}\cdot\hat{\mathbf{e}}_{\rm y}}{|\mathbf{\Gamma}_{\rm LL}|^2}\cos\varphi\,;$$
$$\widetilde{W}_{\rm z}(E) = -\gamma M_{\rm s}\eta_{\rm z}\frac{\Omega^2(E)}{2\pi}\oint\frac{d\mathbf{M}\cdot\hat{\mathbf{e}}_{\rm z}}{|\mathbf{\Gamma}_{\rm LL}|^2}\sin\varphi\,. \tag{4.5}$$

Here the tilde over the spin-current and the generalized forces is used to indicate that they result from an AC spin-current. To obtain the specific form of Eqs. (4.4) and (4.5), $\varphi = 0$ was chosen along the $\hat{\mathbf{e}}_{\rm z}$-axis. Notice that had ϕ been chosen such that $\phi' = \varphi - \omega t \pm \pi$ or had $\varphi = 0$ been chosen along the $-\hat{\mathbf{e}}_{\rm z}$-axis, the phase dependencies of the $\hat{\mathbf{e}}_{\rm y}$ and $\hat{\mathbf{e}}_{\rm z}$ forces in Eqn. (4.5) would be reversed. This means the differences in the free layer response to an $\hat{\mathbf{e}}_{\rm y}$- or $\hat{\mathbf{e}}_{\rm z}$-polarized spin-torque depend only on the energy dependencies of $\widetilde{V}$ and $\widetilde{W}$ calculated in Eqs. (4.4) and (4.5).

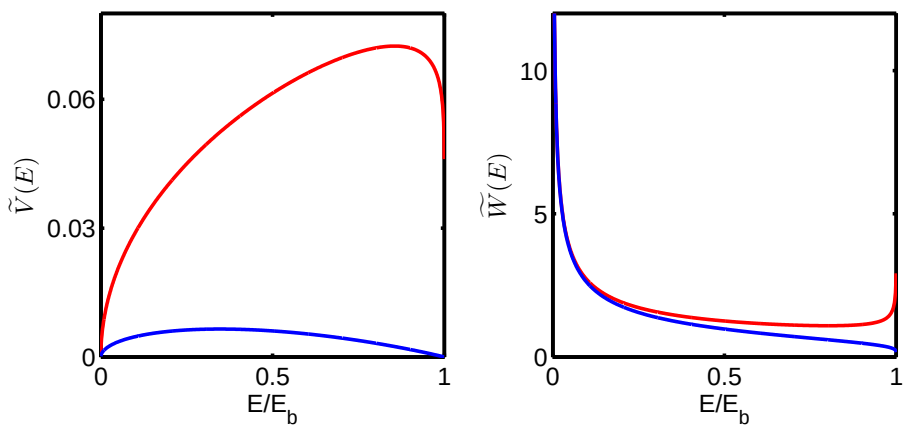

Figure 4.7: Generalized φ-averaged ST forces $\widetilde{V}$(Left) and $\widetilde{W}$(right) in arbitrary units as functions of energy for $\mathbf{m}_{\rm p} = \hat{\mathbf{e}}_{\rm y}$ (blue) and $\mathbf{m}_{\rm p} = \hat{\mathbf{e}}_{\rm z}$ (red) polarized spin-currents. Here $H_{\rm x} = 0.033M_{\rm s}$ and $H_{\rm z} = M_{\rm s}$.

With the ϕ dependence separated from the $\hat{\mathbf{e}}_{\rm y}$ and $\hat{\mathbf{e}}_{\rm z}$ energy and phase forces, the strengths of each can be observed as functions of energy, just as was done for the DC forces. Figure 4.7 plots these generalized forces as functions of energy for a free layer with strong easy-plane anisotropy. As expected from the simulations in Sec. 4.2 the net energy force from the $\hat{\mathbf{e}}_{\rm z}$-polarized AC spin-current is significantly stronger than that from $\hat{\mathbf{e}}_{\rm y}$-polarized AC spin-current. Due to this dramatic difference in strength, for the

rest of this chapter I will only discuss spin-currents polarized along the $\hat{\mathbf{e}}_z$-axis. However, the formalisms that follow can easily be applied to a $\hat{\mathbf{e}}_y$-polarized AC spin-current as well.

A typical parametric trajectory, $E(t)$ versus $\phi(t)$, is shown in Fig. 4.8 for a subcritical spin-current, along with a simulated trajectory using the same parameters. Note the excellent agreement between the simulated trajectory and the trajectory found using Eqs. (4.3). From Fig. 4.8, the damped-oscillator-like motion of the energy observed in the numerical simulations of Sec. 4.2 is made clear: for AC spin-currents, the relative phase between the angle swept out by the free layer and the AC signal acts as a momentum conjugate to the coordinate E, i.e., the energy [91, 115].

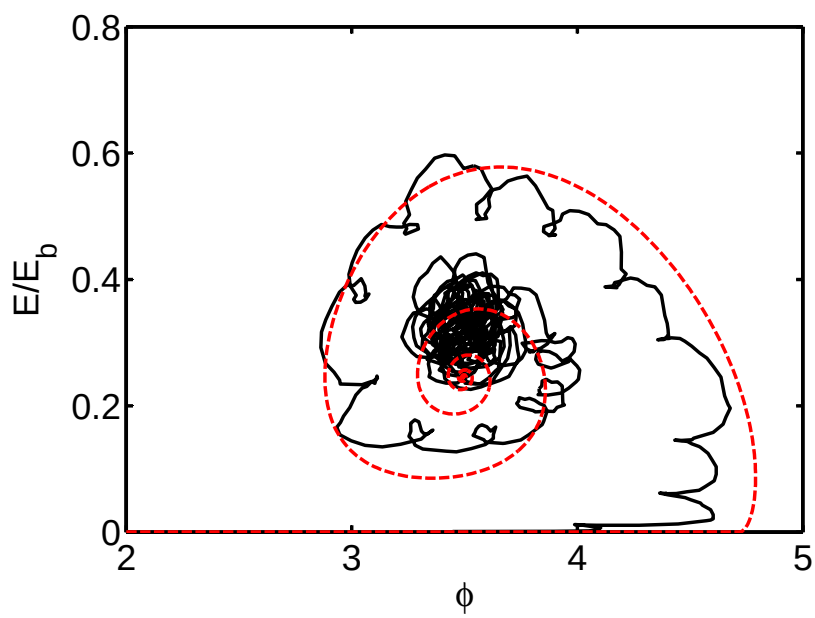

Figure 4.8: Simulated energy E vs. phase ϕ (black, solid) calculated from numerical integration of the LLG Eqn. (2.1) and via Eqn. (4.3) (red, dashed). Here $\widetilde{\mathcal{I}}_s = 0.004M_s$ and $\omega/2\pi = 0.028\gamma M_s$. Other parameters are the same as in Fig. 4.4.

While the dynamics of the free layer under the effect of an AC spin-current appears well described by Eqn. (4.3), there are still many interesting features of the switching probability plots in Sec. 4.2 that have yet to be explained. These features, namely the

strong frequency and current dependencies of the switching probability, are discussed in the following two sections and will prove critical to the task of optimizing the JHL for AC ST switching.

4.4.1 Critical frequency

Understanding the abrupt decrease in switching probability at certain combinations of $\widetilde{\mathcal{I}}_{\mathrm{s}}$ and ω is of critical importance to the viability of AC spin-torque strategies. The simulations shown in Fig. 4.3 have already provided some evidence for the cause of the left-hand boundary of this region. Here recall, for AC frequencies just below the zero-energy natural frequency of the free layer, Ω_0, the size of the energy overshoot increases. However, for too small of frequencies the energy overshoot is substantially diminished. This result implies the existence of a critical AC frequency below which switching using an AC spin-current will not occur.

To gain understanding for how this energy overshoot depends on the AC frequency one may note that in the absence of damping, $\alpha = 0$, the trajectories given by Eqs. (4.3) possess an integral of motion and can thus be described as lines of constant value for some function $\mathcal{H}(E, \phi)$ [91]. Indeed, one can verify that the following function

$$\mathcal{H}(E, \phi) = \int_0^E dE' \mathcal{J}(E') \left[\omega - \Omega(E') + \widetilde{\mathcal{I}}_{\mathrm{s}} \widetilde{W}(E') \cos\phi\right] , \tag{4.6}$$

is conserved by the equations of motion Eqs. (4.3), when $\alpha = 0$. Here $\mathcal{J}(E)$ is a solution of the following linear homogeneous differential equation:

$$\widetilde{V}(E) \frac{d\mathcal{J}(E)}{dE} = \mathcal{J}(E) \left(\widetilde{W}(E) - \frac{d\widetilde{V}(E)}{dE}\right) . \tag{4.7}$$

Setting $E = 0$ in Eqn. (4.6) gives $\mathcal{H} = 0$; thus for a free layer with small initial energy $E_0 \ll E_{\mathrm{b}}$ under the effect of an AC ST, the magnetization should closely follow the $\mathcal{H} = 0$ contour for the initial part of its trajectory. Figure 4.9 shows one such $\mathcal{H} = 0$ trajectory, along with the simulated trajectory from the LLGS equation (2.1) and the corresponding φ-averaged trajectory calculated using Eqs. (4.3). Indeed, even with damping the magnetization closely follows the $\mathcal{H} = 0$ line for a good portion of its initial upward trajectory.

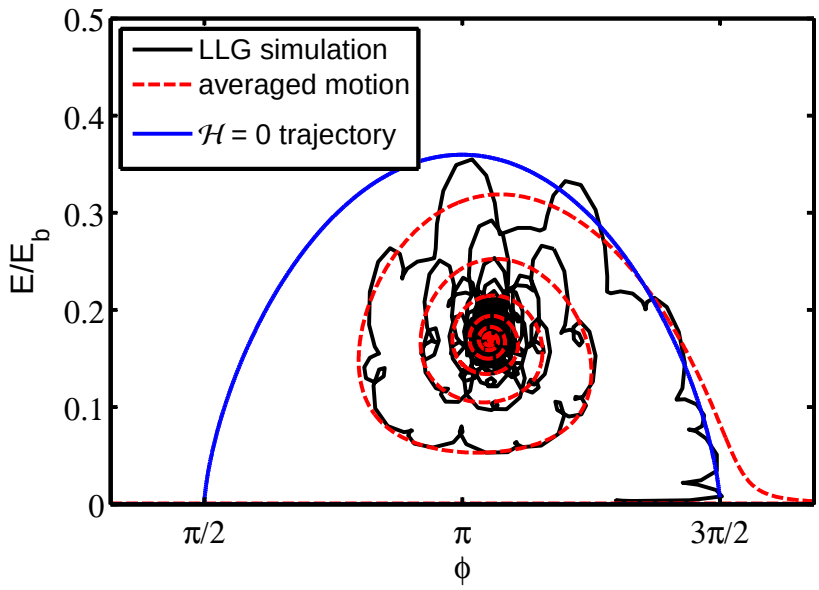

Figure 4.9: Free layer energy E vs. phase ϕ under the effect of an AC spin-current calculated via numerical integration of the LLGS equation(black,solid), Eqn. (4.3) (red,dashed), and $\mathcal{H} = 0$ trajectory (blue,solid) from Eqn. (4.6). Here $\widetilde{\mathcal{I}}_{\rm s} = 0.04 M_{\rm s}$, $\omega = \Omega_0$, and $T = 0$ with other parameters the same as in Fig. 3.2.

This means for small damping the dependence of the phase on the energy can be approximated using the $\mathcal{H} = 0$ trajectory as

$$\widetilde{\mathcal{I}}_{\rm s} \cos(\phi(E)) = \mathcal{F}_\Omega(E) - \mathcal{F}_\omega(E,\omega)\,, \tag{4.8}$$

where

$$\mathcal{F}_\Omega(E) = \frac{\int_0^E dE' \mathcal{J}(E')\Omega(E')}{\int_0^E dE' \mathcal{J}(E')\widetilde{W}(E')}\,; \qquad \mathcal{F}_\omega(E,\omega) = \frac{\int_0^E dE' \mathcal{J}(E')\,\omega}{\int_0^E dE' \mathcal{J}(E')\widetilde{W}(E')}\,. \tag{4.9}$$

Substituting Eqn. (4.8) into $\dot{E}$ in Eqn. (4.3) removes all ϕ dependence from the AC energy trajectory and reduces free layer switching to a one dimensional problem as, was the case for DC spin-currents.

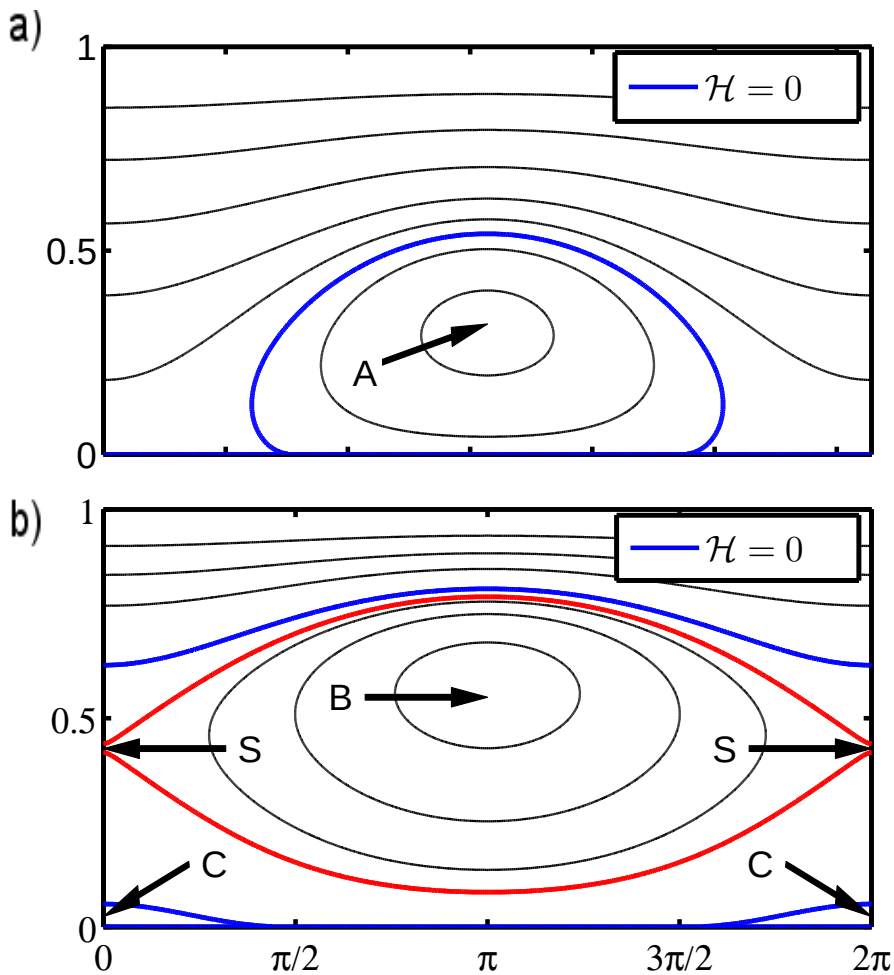

Figure 4.10: Several contours of constant $\mathcal{H}$ (black,thin), including $\mathcal{H} = 0$ (blue,thick) and separatrix contour (red,thick) calculated via Eqn. (4.6) for AC frequencies a) $\omega = 0.9\,\Omega_0$ and b) $\omega = 0.7\,\Omega_0$. Stable fixed points are marked as A, B, and C. Unstable fixed point is marked as S. Here $H_\mathrm{x} = 0.5M_\mathrm{s}$, $H_\mathrm{z} = 0$, $\alpha = 0.015$, $\mathbf{m}_\mathrm{p} = \hat{\mathbf{e}}_\mathrm{x} + \hat{\mathbf{e}}_\mathrm{z}$, and $\widetilde{\mathcal{I}}_\mathrm{s} = 0.04M_\mathrm{s}$.

The dependence of the energy overshoot on the frequency can now be seen clearly by observing how these $\mathcal{H} = 0$ trajectories change while varying ω. Figure 4.10 plots several lines of constant $\mathcal{H}$, calculated from Eqn. (4.6), for a free layer with uniaxial anisotropy and AC signal frequencies $\omega = 0.9\,\Omega_0$ and $\omega = 0.7\,\Omega_0$. Note the difference in

the $\mathcal{H} = 0$ trajectories (blue) as well as the appearance of a separatrix trajectory (red) for $\omega = 0.7\,\Omega_0$. For small initial energies this separatrix prevents the magnetization from reaching the upper $\mathcal{H} = 0$ trajectory, confining it to the lower $\mathcal{H} = 0$ orbit and equilibrium point C. This new equilibrium point is completely out of phase with the spin-current when compared to equilibrium point A, which had $\phi_{\rm eq} = \pi$. This change in phase causes the ST force on the phase to switch from positive to negative, which forces the magnetization to lower energy where $\Omega(E)$ is strong enough to compensate for the added strength of ω and $\widetilde{W}(E)$.

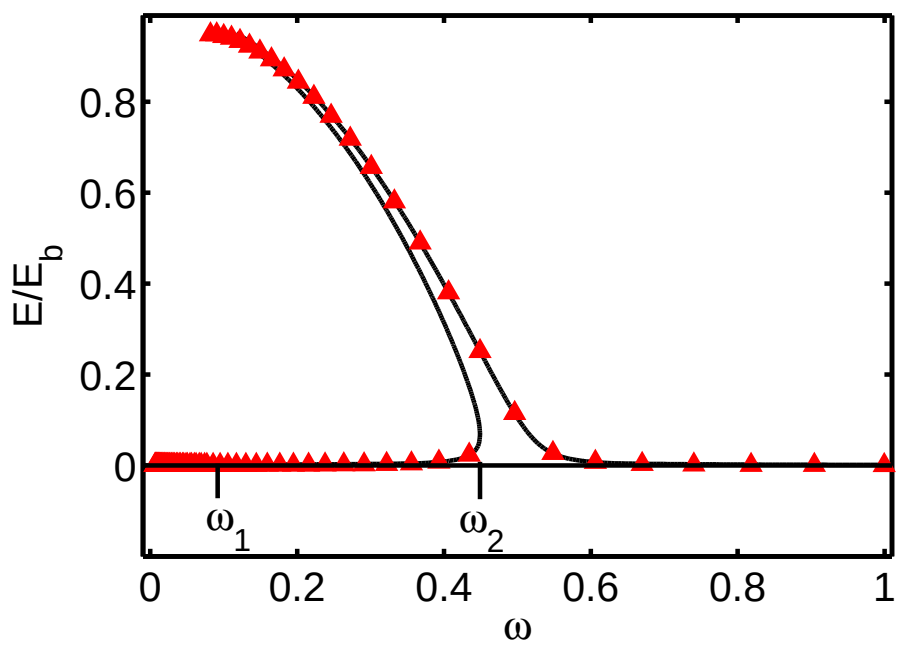

Figure 4.11: Equilibrium energy as a function of frequency ω in units of $\gamma M_{\rm s}$ found via simulation of the LLS equation (red,triangles) and calculated numerically using Eqn. (4.10). Same parameters as in Fig. 3.2.

Varying the AC frequency from $\omega = 0.9\,\Omega_0$ to $\omega = 0.7\,\Omega_0$ one sees these two regimes are separated by a bifurcation frequency. Above this bifurcation frequency the system has a single fixed point and below it two stable fixed points exist, separated by a separatrix. Similar results are found experimentally and via macromagnetic simulations

in Ref. [116]. This bifurcation frequency can be seen clearly in Fig. 4.11, where the equilibrium energy has been calculated by numerically solving

$$\widetilde{\mathcal{I}}_{\mathrm{s}}^{2} = \left(\frac{\alpha U(E)}{\widetilde{V}(E)}\right)^{2} + \left(\frac{\omega - \Omega(E)}{\widetilde{W}(E)}\right)^{2} . \tag{4.10}$$

Equation (4.10) is found by setting the LHS of Eqs. (4.3) to zero, and separating out the phase dependencies. Figure 4.11 also shows E_{eq} calculated via simulations of the LLGS equation, with temperature $T = 0$, by adiabatically varying the frequency with time. From the simulations we see two *jump frequencies* at ω_1 and ω_2 where the energy abruptly jumps between the upper and lower equilibrium branches. Such hysteretic behavior is seen experimentally in Refs. [117]. Since the initial energy is near zero for any switching process, for $\omega < \omega_2$ the trajectory will overshoot and then relax to the lower equilibrium energy branch (point C in Fig. 4.10) while for $\omega > \omega_2$ the trajectory will overshoot and then relax to the upper equilibrium energy branch (point A in Fig. 4.10). This means ω_2 acts as a sort of critical frequency for the switching process. Plotting the simulated ω_2 at various levels of spin-current strength $\widetilde{\mathcal{I}}_{\mathrm{s}}$ one finds excellent agreements with the left-hand boundary of the high switching probability region (see Fig. 4.12).

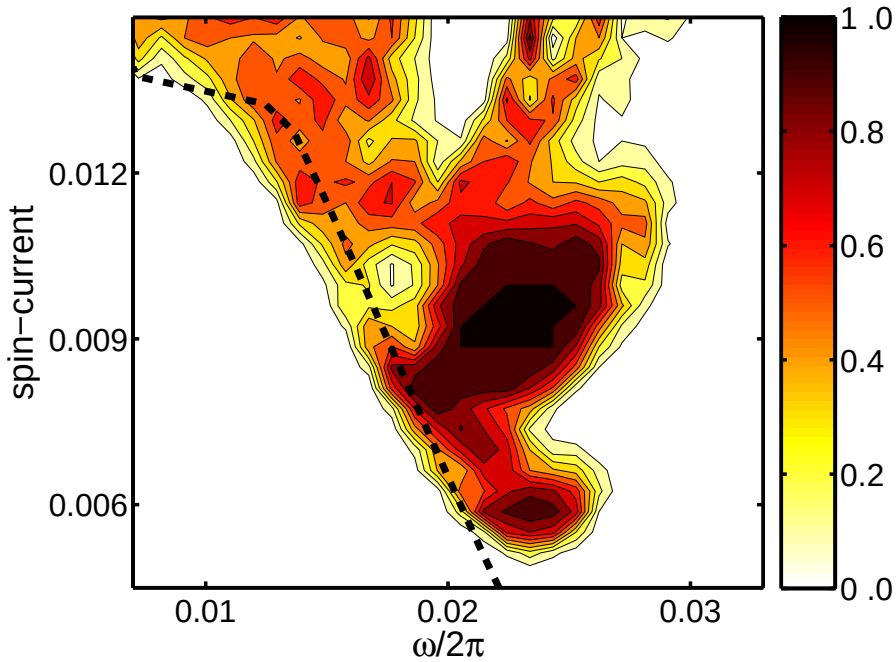

Figure 4.12: Critical frequency $\omega = \omega_2$ (dashed) atop of the switching probability as a function of spin-current ($\widetilde{\mathcal{I}}_{\rm s}/M_{\rm s}$) and driving frequency ω (in units of $\gamma M_{\rm s}$) for AC pulse duration $t_{\rm pl} = 3(2\pi/\omega)$.

4.4.2 Critical current

The right-hand boundary of the high switching probability region can also be found using the $\mathcal{H} = 0$ trajectories derived in Sec. 4.4.1. Since switching can only occur when the energy overshoot exceeds $E_{\rm b}$, the $\mathcal{H} = 0$ trajectory of the free layer, for a given ω and $\widetilde{\mathcal{I}}_{\rm s}$, must exceed $E_{\rm b}$ as well. For AC frequencies greater than the critical frequency ω_2, the maximum of each $\mathcal{H} = 0$ trajectory occurs at $\phi = \pi$ (see Fig. 4.10). Setting $\phi = \pi$ in Eqn. (4.8) and solving for $\widetilde{\mathcal{I}}_{\rm s}$ gives, for the AC critical current,

$$\widetilde{\mathcal{I}}_{\rm s} > \mathcal{F}_\omega(E,\omega) - \mathcal{F}_\Omega(E)\,. \tag{4.11}$$

To calculate the AC critical current the effects of damping must be taken into account. This can be done by integrating the generalized damping force over the $\mathcal{H} = 0$ trajectory and scaling $\widetilde{\mathcal{I}}_{\rm s}$ in order to compensate. Placing Eqn. (4.8) into Eqn. (4.3) and solving

for $\widetilde{\mathcal{I}}_{\rm s}$ gives a lower bounds for the AC critical current,

$$\widetilde{\mathcal{I}}_{\rm c}(\omega) = \left(\left(\frac{\alpha U(E_{\rm b})}{\widetilde{V}_{\rm z}(E_{\rm b})} \right)^2 + \Big(\mathcal{F}_{\Omega}(E_{\rm b}) - \mathcal{F}_{\omega}(E_{\rm b}, \omega) \Big)^2 \right)^{1/2} . \tag{4.12}$$

An example of this critical current is shown in Fig 4.13 along with simulated results. One can see the AC critical current line is indeed close to the boundary of the observed high probability switching region.

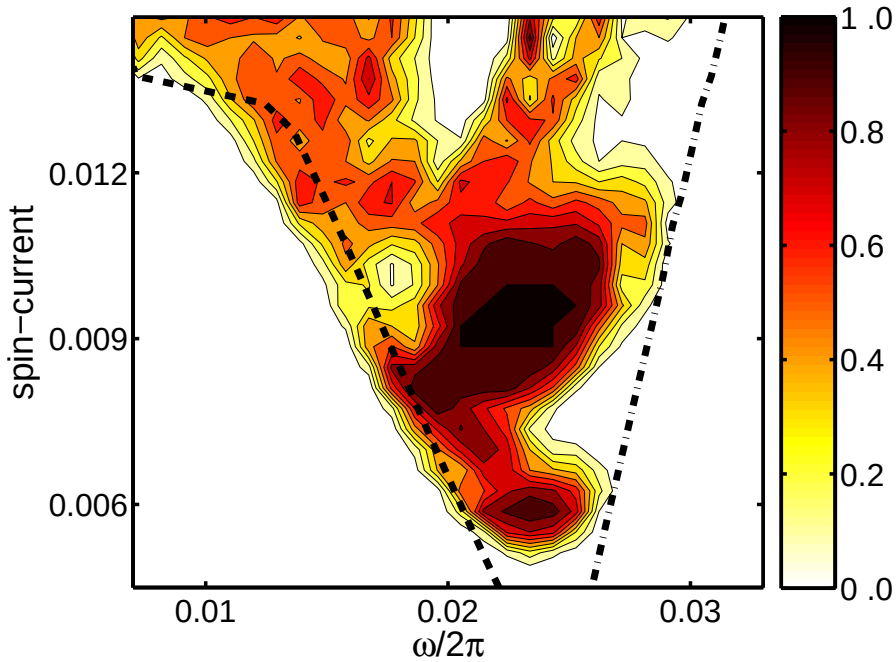

Figure 4.13: Critical frequency $\omega = \omega_2$ (dashed) and critical current (dot-dashed) lines atop of the switching probability as a function of spin-current ($\widetilde{\mathcal{I}}_{\rm s}/M_{\rm s}$) and driving frequency ω (in units of $\gamma M_{\rm s}$) for the pulse duration $t_{\rm pl} = 3(2\pi/\omega)$.

4.5 Joule heat minimization

With a full understanding of the switching behavior of free layers affected by AC spin-currents we can finally proceed to the key portion of this chapter: optimizing the JHL of switching using an AC spin-current. One may recall, when optimizing DC ST switching

the relevant parameters were the strength of the spin-current and the duration of the pulse. For AC spin-currents these must be optimized as well with the addition of the AC signal frequency. The JHL associated with switching using an AC spin-current can be approximated by

$$J(\widetilde{\mathcal{I}}_{\mathrm{s}}) = \int_{E_0}^{E_{\mathrm{b}}} dE \frac{R\widetilde{\mathcal{I}}_{\mathrm{s}}^2}{2\dot{E}} \,, \tag{4.13}$$

c.f. from Eqn. (3.19). Here $\dot{E}$ is given by Eqn. (4.3) and the factor of two in the denominator comes from averaging that power dissipated over the driving frequency, i.e., $\langle \sin^2 \varphi \rangle / 2\pi = 1/2$.

Varying Eqn. (4.13) with respect to the AC spin-current strength $\widetilde{\mathcal{I}}_{\mathrm{s}}$ and frequency ω, paying close attention to the energy dependence of $\sin\phi$ (calculated using Eqn. (4.8) with $\mathcal{H} = 0$), gives the following optimization equations

$$0 = \frac{R}{2} \int_{E_0}^{E_{\mathrm{b}}} dE \, \frac{\widetilde{\mathcal{I}}_{\mathrm{s}}}{\dot{E}^2} \left(2\dot{E} + \frac{\widetilde{\mathcal{I}}_{\mathrm{s}} \widetilde{V}(E)}{\sin\phi} \right) \,; \tag{4.14a}$$

$$0 = \frac{R}{2} \int_{E_0}^{E_{\mathrm{b}}} dE \, \frac{\widetilde{\mathcal{I}}_{\mathrm{s}}^2}{\dot{E}^2} \left(\mathcal{F}_\omega(E) \, \widetilde{V}(E) \cot\phi \right) \,, \tag{4.14b}$$

which correspond to $\partial_{\widetilde{\mathcal{I}}_{\mathrm{s}}} J = 0$ and $\partial_\omega J = 0$, respectively. It should again be pointed out here that, as was the case for DC spin-currents, there may be more or fewer optimization equations depending on the assumed forms of $\widetilde{\mathcal{I}}_{\mathrm{s}}$ and ω. The two optimization equations listed in Eqn. (4.14) are applicable when $\widetilde{\mathcal{I}}_{\mathrm{s}}$ and ω have no assumed energy/time dependencies and when $\widetilde{\mathcal{I}}_{\mathrm{s}}$ and ω are assumed to be constant throughout the switching process.

In the following two sections I discuss solutions to Eqn. (4.14) for both of these cases. First, I will cover the energy-dependent case, where $\widetilde{\mathcal{I}}_{\mathrm{s}}$ and ω are allowed to vary freely in energy/time. This case has an analytic solution similar to that found for DC switching in Sec. 3.5.1. Second, I will cover the case where $\widetilde{\mathcal{I}}_{\mathrm{s}}$ and ω are held constant. The optimal protocols for this case are solved numerically.

4.5.1 Optimal AC spin-current protocol: analytic

As in the DC optimization case one can imagine infinite AC spin-current strategies that may satisfy Eqs. (4.14), each of which will represent at best a local minimum in

an otherwise infinite parameter space. The spin-current protocol that gives the global minimum JHL for AC spin-current strategies is found by solving Eqs. (4.14) without placing any restrictions on the energy/time dependence of $\widetilde{\mathcal{I}}_{\rm s}$ and ω. Amazingly, such a solution exists. One may indeed verify that the following functions for $\widetilde{\mathcal{I}}_{\rm s}$ and ω satisfy Eqs. (4.14):

$$\widetilde{\mathcal{I}}_{\rm opt}(E) = 2\frac{\alpha U(E)}{\widetilde{V}(E)}\,; \qquad \omega_{\rm opt}(E) = \Omega(E)\,. \tag{4.15}$$

The optimal AC frequency protocol from Eqs. (4.15) clearly is to drive the spin-current at the natural precessional-frequency of the free layer through the entire switching trajectory. Substituting $\Omega(E)$ for ω in the equation of motion for ϕ, Eqn. (4.3) gives

$$\dot{\phi} = -\widetilde{\mathcal{I}}_{\rm s}\widetilde{W}(E)\cos\phi\,. \tag{4.16}$$

By inspection one can see Eqn. (4.16) has one stable equilibrium point at $\phi = 3\pi/2$ and one unstable equilibrium point at $\phi = \pi/2$. This means, by keeping the AC signal frequency at the natural frequency of the free layer, the magnetization and the AC signal become phase-locked. For small initial energies $E_0 \ll E_{\rm b}$ this phase-locking happens rapidly as $\widetilde{W} \propto 1/\sqrt{E}$ for $E \ll E_{\rm b}$.

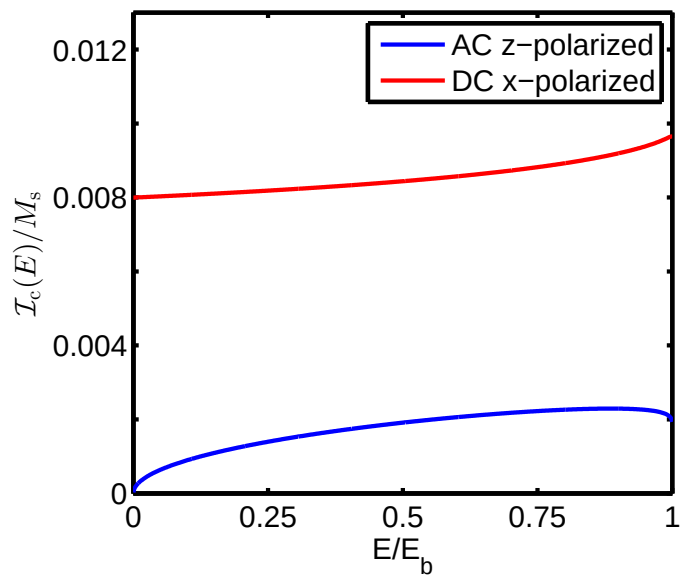

Figure 4.14: Local critical current $\widetilde{\mathcal{I}}_c(E)$ associated with the optimal AC frequency $\omega_{opt} = \Omega(E)$ as a function of free layer energy (blue) along with the equivalent DC local critical current(red). Here $H_x = 0.033M_s$, $H_z = M_s$, and $\alpha = 0.015$.

This phase-locking between the magnetization and the AC signal has a profound effect on the efficiency of the AC ST. Placing $\omega = \Omega(E)$ into the AC energy equation of motion, Eqn. (4.3) gives

$$\dot{E} = -\alpha U(E) + \widetilde{\mathcal{I}}_s \widetilde{V}(E)\,; \tag{4.17}$$

thus, $\omega_{opt} = \Omega(E)$ also maximizes the ability of the AC ST to push the free layer to higher energy. Note this also gives the AC energy equation of motion the same form as the DC energy equation of motion. This means when $\omega = \Omega(E)$ there exists an AC local critical current $\widetilde{\mathcal{I}}_c(E) = \alpha U(E)/\widetilde{V}(E)$ exactly equivalent to the local DC critical current found in chapter 3. An example of this local critical current is shown in Fig. 4.14. Note $\widetilde{\mathcal{I}}_c$ at its largest value is almost a quarter of the lowest local critical current using a DC spin-current. One may also notice that the optimal AC spin-current strength is precisely twice this local critical current

$$\widetilde{\mathcal{I}}_{opt}(E) = 2\widetilde{\mathcal{I}}_c(E); \qquad \widetilde{\mathcal{I}}_c(E) = \frac{\alpha U(E)}{\widetilde{V}(E)}\,, \tag{4.18}$$

just as in the DC case. Inserting $\widetilde{\mathcal{I}}_{\rm opt}$ and $\omega_{\rm opt}$ into the energy equation of motion given by Eqn. (4.17) one finds

$$\dot{E} = +\alpha\, U(E)\,. \tag{4.19}$$

Once again this means *the optimal spin-current protocol exactly time-reverses the purely relaxational trajectory of the free layer magnetization from initial energy* $E_{\rm b}$ *to the energy minimum* E_0.

4.5.2 Practical solutions

The spin-current protocol given in the previous section for the global minimum JHL using an AC/DC spin-current strategy provides us with valuable insight into how the free layer should behave near optimal switching conditions. However, applying this strategy is not practical for many reasons. Chief amongst these is its strong dependence on the energy trajectory of the free layer. For ST devices at room temperature, thermal noise prevents knowing the exact trajectory for each switch. Theoretically these thermal fluctuations could be overcome by adjusting the spin-current in real time. However, as most practical applications of ST switching require switching times in the nanosecond and sub-nanosecond regimes, any such self-adjusting system would be well beyond the limits of current technology. Even without thermal fluctuations, producing an AC current that matches the optimal spin-current protocol given by Eqs. (4.14) would likely prove prohibitively difficult.

For these reason I now discuss practical solutions to Eqs. (4.14) that give local minima for the JHL. The simplest, most practical restriction one can place on the form of the spin-current parameters $\widetilde{\mathcal{I}}_{\rm s}$ and ω, is to require each be held constant for the duration of the AC pulse, as was done for the simulations presented in section 4.2. This requires Eqs. (4.14) be solved numerically, and thus it is useful to place limitations on the range where the optimal values of each parameter may be found.

To limit the range for the optimal frequency $\omega_{\rm opt}$, one may notice each of the terms in Eqn. (4.14b), save $\cos\phi$, is either entirely positive or entirely negative over the range of integration. Thus, any frequency that satisfies Eqn. (4.14b) must produce an $\mathcal{H} = 0$ trajectory such that $\cos(\phi_E)$ is neither entirely positive or entirely negative over the range of integration. An example of such a trajectory is shown in Fig. 4.10. Substituting

Eqs. (4.9) into Eqn. (4.8) with $\phi = 3\pi/2$ gives the necessary, but not sufficient, condition

$$0 = \int_{E_0}^{E} dE \mathcal{J}\left(\omega - \Omega(E)\right) , \tag{4.20}$$

which ω_{opt} must satisfy. Since $\Omega(E)$ monotonically decreases with increasing energy, this puts an upper bounds on the optimal frequency of $\omega_{\text{opt}} < \Omega_0$. The range of possible values for ω_{opt} can be restricted further by recalling for frequencies above the upper bifurcation frequency ω_2, switching is prohibited by the formation of a separatrix trajectory that confines the free layer energy to oscillate about the lower equilibrium energy (see Fig. 4.10). Combining these upper and lower bounds on the optimal frequency gives

$$\omega_2 < \omega_{\text{opt}} < \Omega_0 \, . \tag{4.21}$$

Limits on the optimal AC spin-current strength $\widetilde{\mathcal{I}}_{\text{opt}}$ may be obtained similarly by observing that only the numerator in Eqn. (4.14a), $2\dot{E}_{AC}(E) + \widetilde{\mathcal{I}}_{\text{s}}\widetilde{V}(E)/\sin\phi$, can be both positive and negative in the range of integration. This means the numerator must be zero somewhere in the range $E_0 < E < E_{\text{b}}$. An upper limit on the optimal AC spin-current $\widetilde{\mathcal{I}}_{\text{opt}} < \widetilde{\mathcal{I}}_{\text{max}}(E)$ may be found by setting the numerator of Eqn. (4.14a) equal to zero and solving for $\widetilde{\mathcal{I}}_{\text{s}}$ with $E = E_{\text{b}}$. Doing so gives

$$\widetilde{\mathcal{I}}_{\text{max}}(\omega) = \left(2\widetilde{\mathcal{I}}_{\text{c}}(\omega)\left(\widetilde{\mathcal{I}}_{\text{c}}(\omega) + \widetilde{\mathcal{I}}_{\text{c}}(E_{\text{b}})\right)\right)^{1/2} , \tag{4.22}$$

where $\widetilde{\mathcal{I}}_{\text{c}}(\omega)$ is the AC critical current for constant ω given by Eqn. (4.12) and $\widetilde{\mathcal{I}}_{\text{c}}(E_{\text{b}})$ is the AC local critical current when $\omega = \Omega(E)$, as given by Eqn. (4.18). Since the optimal protocol should be such that $\dot{E} > 0$ through the entire switching process, $\widetilde{\mathcal{I}}_{\text{c}}(\omega)$ acts as a lower limit on the optimal AC spin-current strength as well. Combining these two constraints, the optimal AC spin-current strength must fall in the range

$$\widetilde{\mathcal{I}}_{\text{c}}(\omega) < \widetilde{\mathcal{I}}_{\text{opt}} < \widetilde{\mathcal{I}}_{\text{max}}(\omega) \, . \tag{4.23}$$

Chapter 5

AC/DC spin-torque

In this chapter I discuss AC/DC spin-current strategies using the formalisms and theoretical methods developed in chapters 3 and 4. I again begin by presenting numerical simulations of ST switching using AC/DC spin-current pulses. From there I present a theoretical description of free layer dynamics and switching using strategies that draw heavily from the theoretical findings in the previous two chapters. Finally, I conclude this chapter by showing how AC/DC spin-current strategies can be optimized to minimize the JHL from switching.

5.1 Introduction

In chapter 4 it was shown that by applying an AC spin-current polarized along the easy-plane axis, the critical current and switching energy could be significantly reduced in MTJs with a free layer exhibiting strong easy-plane anisotropy. However as Fig. 4.2 illustrates, for free layers with weak easy-plane anisotropy, DC spin-current strategies remain superior due to the large AC spin-currents required to produce switching. This result is disappointing since free layers with weak easy-plane anisotropy have lower DC critical currents when compared those with strong easy-plane anisotropy of equal stability, i.e., equal energy barrier height $E_{\mathrm{b}} = \frac{1}{2}H_{\mathrm{x}}M_{\mathrm{s}}$ (see Eqn. (3.13) and Fig. 3.10). This seems to force a choice between fast switching times, i.e., AC spin-current switching in free layers with strong easy-plane anisotropy, and high efficiency, i.e., DC spin-current switching in free layers with weak easy-plane anisotropy.

Thankfully, this is not the end of the story. While AC spin-currents are less efficient than DC spin-currents at producing switching in free layers with weak easy-plane, they can very efficiently push the free layer to energies below the height of the energy barrier. This is because at low energies the ST from spin-currents polarized along the hard-axis $\hat{\mathbf{e}}_{\mathrm{y}}$ and easy-plane $\hat{\mathbf{e}}_{\mathrm{z}}$ directions remain significantly stronger than the ST from spin-currents polarized along the easy-axis $\hat{\mathbf{e}}_{\mathrm{x}}$ direction. This tradeoff suggests an alternative means of magnetic switching in MTJs with weak easy-plane anisotropy. Instead of using a purely AC or DC spin-current, an AC pulse may be used to push the magnetization to a higher energy state where a DC spin-current can then be used to switch the magnetization the rest of the way. Such an AC/DC current pulse strategy is considered experimentally in Ref. [60] and via micromagnetic simulations in Ref. [118] where AC external fields provided the initial resonant response. In both cases, the AC pulse is shown to markedly improve the efficiency of the switching process.

5.2 Numerical simulations of AC/DC ST

To make the trade-off between AC and DC spin-currents more apparent, in this section I present numerical simulations of the LLGS equation directly comparing the effects of AC, DC, and AC/DC spin-current strategies. Here the AC spin-current pulses are of the form $\mathcal{I}_{\mathrm{s}}(t) = \widetilde{\mathcal{I}}_{\mathrm{s}} \sin(\omega t)$ with pulse duration t_{AC} where $\widetilde{\mathcal{I}}_{\mathrm{s}}$ is the strength of the AC spin-current and ω is the AC signal frequency. The DC spin-current pulses are of the form $\mathcal{I}_{\mathrm{s}}(t) = \overline{\mathcal{I}}_{\mathrm{s}}$ with pulse duration t_{DC} where $\overline{\mathcal{I}}_{\mathrm{s}}$ is the strength of the DC spin-current, and the AC/DC spin-current pulses consist of an AC pulse followed immediately by a DC pulse, with total pulse time $t_{\mathrm{pl}} = t_{\mathrm{AC}} + t_{\mathrm{DC}}$. In all the cases presented here, simulations were performed on the free layer with uniaxial anisotropy shown in chapters 3 and 4 with $H_{\mathrm{x}} = 0.5M_{\mathrm{s}}$ and $H_{\mathrm{z}} = 0$. Each of the applied spin-currents had a polarization vector $\mathbf{m}_{\mathrm{p}} = \hat{\mathbf{e}}_{\mathrm{x}} + \hat{\mathbf{e}}_{\mathrm{z}}$ to maximize the strength of the ST from the AC and DC spin-current pulses.

The trade-off in strength between AC and DC spin-currents can easily be seen in the energy response of the free layer to each current strategy. Figure 5.1 shows such energy responses as a function of time for AC, DC, and combined AC/DC spin-current pulses. Notice the spin-current strength is strong enough to produce switching when

applied via a DC current pulse. Notice also that while the AC pulse does not produce switching on its own, it produces a much stronger initial response than the DC spin-current. The AC/DC pulse shown in Fig. 5.1 capitalizes on this tradeoff by switching from AC to DC just as the free layer reaches the maximum AC overshoot. In this example, the combined AC/DC current strategy cuts the switching time nearly in half without needing to change the strength of the spin-current or the polarization.

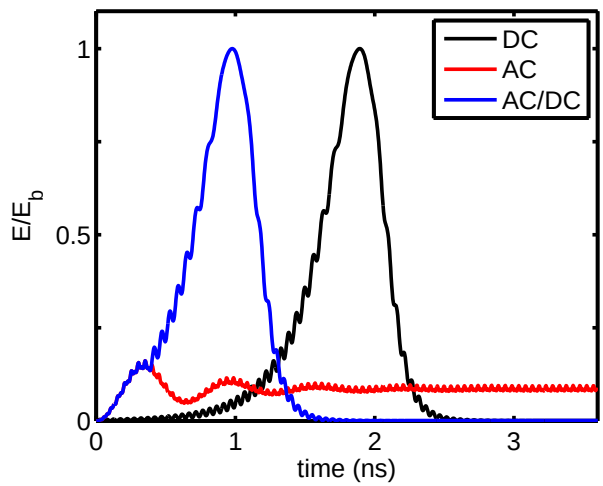

Figure 5.1: Free layer energy E as a function of time for DC (black), AC (red), and AC/DC (blue) spin-current pulses. In all cases $H_\mathrm{x} = 0.5M_\mathrm{s}$, $H_\mathrm{z} = 0M_\mathrm{s}$, $\alpha = 0.015$, $\mathcal{I}_\mathrm{s} = 0.015M_\mathrm{s}$, and $\mathbf{m}_\mathrm{p} = \hat{\mathbf{e}}_\mathrm{x} + \hat{\mathbf{e}}_\mathrm{z}$. For the AC pulse and the AC portion of the AC/DC pulse, $\omega = \Omega_0$.

It is evident from Fig. 5.1 that adding the AC pulse to the beginning of the spin-current pulse dramatically reduced the switching time as well as the JHL. However, this is one specific example. For this to truly be a superior strategy the minimum JHL for the combined AC/DC spin-current strategy must be below that of the purely DC strategy. To show this is indeed the case, Fig. 5.1 plots the minimum JHL calculated over a broad range of spin-current strengths for both a purely DC spin-current strategy and a combined AC/DC strategy. For simplicity, the strength of the AC and DC pulses of the AC/DC spin-current pulse were taken to be equal, $\mathcal{I}_\mathrm{s} = \widetilde{\mathcal{I}}_\mathrm{s} = \overline{\mathcal{I}}_\mathrm{s}$, for each trial. The energy loss due to Joule heating for each attempt was calculated by integrating

the power over the duration of the current pulse $J = \int_0^{t_{\rm pl}} dt R \mathcal{I}_{\rm s}^2(t)$ as in chapters 3 and 4. Expressing the total JHL in terms of the JHL from the AC and DC portions of the spin-current pulse gives

$$J = \int_0^{t_{\rm AC}} dt R \widetilde{\mathcal{I}}_{\rm s}^2 \sin^2(\omega t) + \int_{t_{\rm AC}}^{t_{\rm pl}} dt R \overline{\mathcal{I}}_{\rm s}^2 \,. \tag{5.1}$$

Figure 5.2 shows the parameter set resulting in the least JHL, with switching probability above 99.5%, for each spin-current amplitude $\mathcal{I}_{\rm s}$. Notice the optimal energy loss using this AC/DC method is almost a third of the purely DC method for the same device, and the optimal current is roughly half. Notice also that the critical current appears to be roughly equal between the DC and AC/DC strategies. The experimental results of Ref. [60] showed as much as a 40% reduction in JHL for a free layer with strong easy-plane anisotropy with the spin-current polarized approximately 30° between the easy-axis and the hard axis direction. A smaller reduction in JHL, $7-8\%$, was observed in Ref. [118] using micromagnetic simulations.

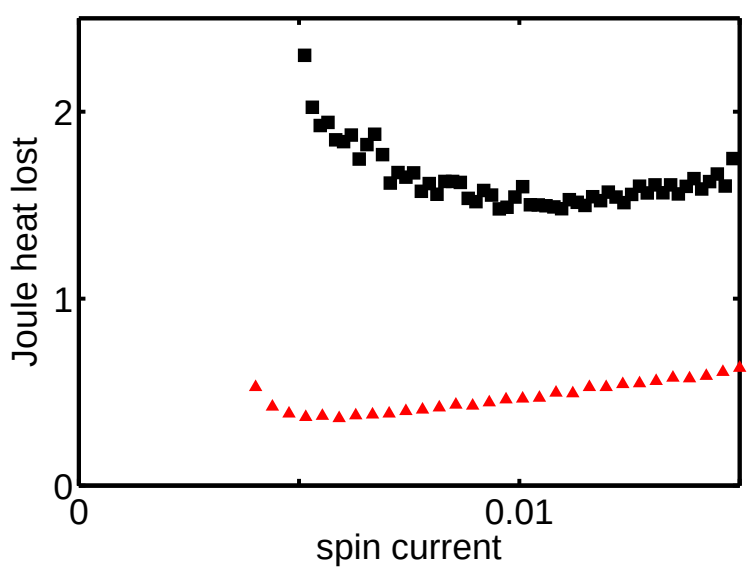

Figure 5.2: Simulated optimal JHL in arbitrary units as a function of spin-current amplitude ($\mathcal{I}_{\rm s}/M_{\rm s}$) for DC (black squares) and AC/DC (red triangles) spin-current strategies. Other parameters are the same as in Fig. 3.2.

5.3 Joule heat minimization

The theoretical descriptions for the free layer response to AC and DC spin-currents found in chapters 3 and 4, respectively, may also be applied to the AC/DC pulses considered in this chapter. Since the AC pulse comes first, the free layer energy at the start of the AC pulse is near the energy minimum; thus the AC trajectory will closely follow the $\mathcal{H} = 0$ trajectory. This means the AC response will not depend strongly on the initial phase between the AC signal and the angle of the magnetization. Since the DC response is also ignorant of the phase in this approximation (and angle φ), no special considerations are needed when applying the φ-averaged AC energy and phase equations of motion or the φ-averaged DC energy equation of motion. A similar independence on the phase of the free layer is seen in Ref. [118] via micromagnetic simulations where AC external fields are applied to excite the free layer prior to a DC spin-current pulse. This phase-independence of the AC/DC spin-current strategies allows us to move directly to the task of determining the optimal protocol that minimizes the JHL during each switch.

Before attempting to optimize the switching protocol with respect to JHL, one must first express the energy dissipated in terms of the AC/DC spin-current parameters. This is done by placing Eqs. (4.13) and (3.19) for the JHL from switching using AC and DC spin-currents, respectively, into Eqn. (5.1), which gives

$$J(\widetilde{\mathcal{I}}_{\mathrm{s}}) = \int_{E_0}^{E_{\mathrm{c}}} dE \frac{R\widetilde{\mathcal{I}}_{\mathrm{s}}^{2}}{2\dot{E}} + \int_{E_{\mathrm{c}}}^{E_{\mathrm{b}}} dE \frac{R\overline{\mathcal{I}}_{\mathrm{s}}^{\;2}}{\dot{E}} \,. \tag{5.2}$$

Here E_{c} is the energy of the free layer when the spin-current is switched from AC to DC, R is a constant proportional to the resistance of the MTJ and $\dot{E}$ is the energy "velocity" of the free layer under the effect of the AC or DC spin-currents, given by Eqs. (5.3) and (5.4), respectively. For the convenience of the reader, recall the φ-averaged AC equations of motion are

$$\begin{aligned} \dot{E} &= -\alpha U(E) - \widetilde{\mathcal{I}}_{\mathrm{s}}\widetilde{V}_{\mathrm{z}}(E)\sin\phi\,; \\ \dot{\phi} &= \Omega(E) - \omega - \widetilde{\mathcal{I}}_{\mathrm{s}}\widetilde{W}_{\mathrm{z}}(E)\cos\phi\,, \end{aligned} \tag{5.3}$$

c.f. Eqs. (4.3), and the DC φ-averaged energy equation of motion is

$$\dot{E} = -\alpha U(E) + \overline{\mathcal{I}}_{\mathrm{s}}\overline{V}_{\mathrm{x}}(E)\,, \tag{5.4}$$

c.f. Eqn. (3.8). Here U and $\overline{V}_{\rm x}$ are given by Eqs. (3.9), $\widetilde{V}_{\rm z}$ is given by Eqn. (4.4), and $\widetilde{W}_{\rm z}$ is given by Eqn. (4.5).

Using $E_{\rm c}$ in place of $t_{\rm AC}$ and $t_{\rm DC}$ acts to eliminate one of the spin-current parameters and is centered on the observation that the total pulse time $t_{\rm pl}$ should be just long enough to produce a switch; thus $t_{\rm DC} = t_{\rm pl} - t_{\rm AC}$ is entirely dependent on $t_{\rm AC}$ and the remaining spin-current parameters. To convert from $E_{\rm c}$ back into the relevant pulse times one may employ the relations

$$t_{\rm AC} = \int_{E_0}^{E_{\rm c}} \frac{dE}{\dot{E}}\,; \qquad t_{\rm DC} = \int_{E_{\rm c}}^{E_{\rm b}} \frac{dE}{\dot{E}}\,, \tag{5.5}$$

where again each of the integrals represents a path integral over the AC or DC energy trajectories.

Equation (5.2) can now be used to determine the optimization equations for AC/DC spin-current strategies by varying Eqn. (5.2) with respect to each of the remaining spin-current parameters. These parameters are: the AC spin-current strength $\widetilde{\mathcal{I}}_{\rm s}$, the AC spin-current frequency ω, the DC spin-current strength $\overline{\mathcal{I}}_{\rm s}$, and the energy $E_{\rm c}$ where the spin-current changes from an AC pulse to a DC pulse. Taking these derivatives, paying careful attention to the dependence of $\phi(E)$ on ω and $\widetilde{\mathcal{I}}_{\rm s}$ gives

$$0 = \frac{R}{2}\int_{E_0}^{E_{\rm c}} dE\,\frac{\widetilde{\mathcal{I}}_{\rm s}}{\dot{E}^2}\left(2\dot{E} + \frac{\widetilde{\mathcal{I}}_{\rm s}\,\widetilde{V}_{\rm z}(E)}{\sin\phi}\right)\,; \tag{5.6a}$$

$$0 = \frac{R}{2}\int_{E_0}^{E_{\rm c}} dE\,\frac{\widetilde{\mathcal{I}}_{\rm s}^2}{\dot{E}^2}\left(\mathcal{F}_\omega(E)\,\widetilde{V}_{\rm z}(E)\cot\phi\right)\,; \tag{5.6b}$$

$$0 = R\int_{E_{\rm c}}^{E_{\rm b}} dE\,\frac{\overline{\mathcal{I}}_{\rm s}}{\dot{E}^2}\left(\overline{\mathcal{I}}_{\rm s}\,\overline{V}_{\rm x}(E) - 2\alpha U(E)\right)\,; \tag{5.6c}$$

$$0 = R\left(\frac{\overline{\mathcal{I}}_{\rm s}^2}{\dot{E}} - \frac{\widetilde{\mathcal{I}}_{\rm s}^2}{2\dot{E}}\right)_{E=E_{\rm c}}\,. \tag{5.6d}$$

Here recall the generalized φ-averaged AC and DC forces are given by Eqs. (4.4) and Eqs. (3.9), respectively; $\mathcal{F}_\omega$ is given by Eqn. (4.9); and $\phi(E)$ is given by the $\mathcal{H} = 0$ trajectory found using Eqn. (4.8). In the following sections I discuss analytical and numerical solutions to Eqs. (5.6).

5.3.1 Optimal AC/DC spin-current protocol: analytic

Upon inspection of Eqs. (5.6) one may immediately notice that, other than the limits of integration, the first two optimization equations, Eqs. (5.6a) and (5.6b), are identical to Eqs. (4.14) for optimizing the JHL of and AC spin-current. One may also note that the third equation, Eqn. (5.6c), is identical to the DC optimization equation, Eqn. (3.20), with E_0 replaced by E_c. This means the energy-dependent solutions for three of the optimization equations are already known and given by

$$\mathcal{I}_\mathrm{opt}(E) = 2\begin{cases} \widetilde{\mathcal{I}}_\mathrm{c}(E)\sin(\vartheta(E)) & : E < E_\mathrm{c} \\ \overline{\mathcal{I}}_\mathrm{c}(E) & : E_\mathrm{c} < E \end{cases}, \tag{5.7}$$

with

$$\widetilde{\mathcal{I}}_\mathrm{c}(E) = \alpha\frac{U(E)}{\widetilde{V}_\mathrm{z}(E)}, \qquad \vartheta(E) = \int_{E_0}^{E} dE'\frac{\Omega(E')}{\dot{E}'}, \qquad \overline{\mathcal{I}}_\mathrm{c}(E) = \alpha\frac{U(E)}{\overline{V}_\mathrm{x}(E)}, \tag{5.8}$$

c.f. Eqs. (4.15) and Eqn. (3.21), respectively. This leaves only the optimal value for E_c that needs to be calculated using Eqn. (5.6d).

One may of course correctly point out there is no guarantee that a solution to Eqn. (5.6d) exists given the specific solutions listed in Eqn. (5.7). This apparent contradiction is mitigated by the fact that the AC and DC protocols given by Eqs. (5.7) are also the optimal protocols of the purely AC and DC spin-current strategies respectively. This means if Eqn. (5.6d) does not have a solution, the optimal AC/DC protocol is to use either a purely AC or purely DC spin-current pulse. It is important here to note that, regardless of the outcome, when calculating E_c the optimal spin-current protocol causes the magnetization to follow the time-revered relaxation trajectory from the energy barrier to the energy minimum in the absence of spin-torque and damping.

For cases where Eqn. (5.6d) has a solution, our intuition tells us the optimal protocol should be such that the AC pulse is used until the efficiency of the DC pulse surpasses it; thus E_c should be the energy where the efficiencies of the AC and DC pulses equal. This efficiency criteria is exactly the physical interpretation of Eqn. (5.6d). Moving the AC terms in Eqn. (5.6d) to the LHS and inverting, keeping the factors of resistance R on each side, gives

$$\frac{2\dot{E}}{R\widetilde{\mathcal{I}}_\mathrm{s}^2(E_\mathrm{c})} = \frac{\dot{E}}{R\overline{\mathcal{I}}_\mathrm{s}^2(E_\mathrm{c})}. \tag{5.9}$$

The terms on each side are clearly the instantaneous efficiencies of the AC and DC spin-current methods, respectively, i.e., the rate of work done increasing the energy of the free layer divided by power dissipated in doing so. An example of this is shown in Fig. 5.3.

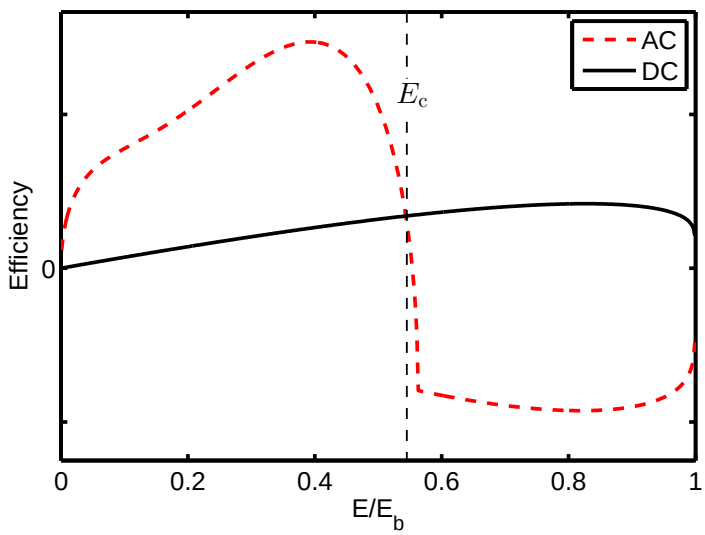

Figure 5.3: Spin-current efficiency calculated via Eqn. (5.9) for AC (red,dashed) and DC(black,solid) spin-currents. Here $H_z = M_s$, $H_x = 0.5M_s$, $\alpha = 0.015$, $\widetilde{\mathcal{I}}_s = \overline{\mathcal{I}}_s = 0.04M_s$, and $\omega = \Omega_0$.

Whether the optimal AC/DC protocol uses a purely AC, DC, or combined AC/DC protocol naturally depends on the spin-current polarization and the free layer anisotropy. From the specific cases simulated and discussed so far in this thesis, we have seen cases where purely DC spin-currents are optimal (such as when $\mathbf{m}_p = \hat{\mathbf{e}}_x$), where purely AC spin-currents are optimal (such as for free layers with strong easy-plane anisotropy and strong ST along the easy-plane direction), and where AC/DC spin-currents are optimal. These, however, are but a small subset of the possible MTJ anisotropy configurations. Figure 5.4 shows E_c calculated numerically for a wide range of spin-current polarization and anisotropy configurations using the AC and DC spin-current protocols given by Eqs. (4.15) and (3.21). As expected, for strong easy-plane anisotropy and for strong spin-polarization along the easy-plane direction, purely AC spin-current protocols are

optimal, while for very weak spin-polarization along the easy-plane direction, purely DC spin-current protocols are optimal. This gives a large range of spin-polarizations and anisotropy configurations where AC/DC spin-currents may show improvement over purely AC or DC ones.

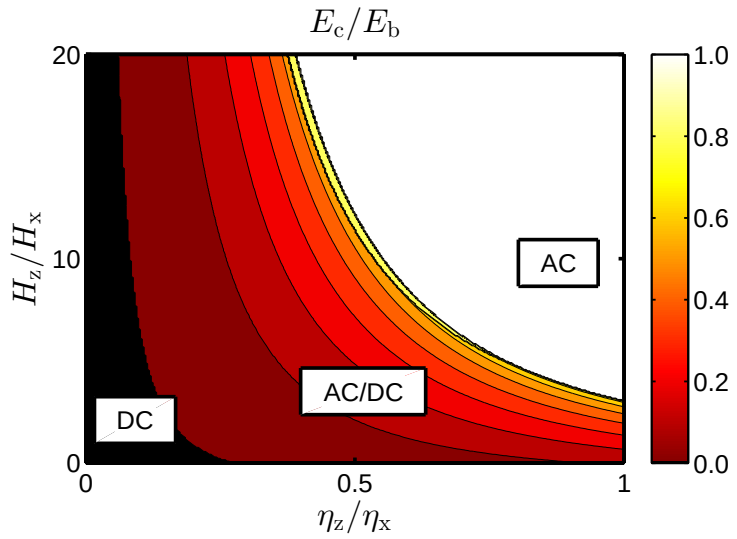

Figure 5.4: Free layer energy E_c (color) where the spin-current should be changed from AC to DC in order to minimize the JHL as a function of the relative anisotropy strengths H_z/H_x and the spin-polarization ratio η_z/η_x. Here white indicates the optimal protocol uses only AC spin-current and black indicates the optimal protocol uses only DC spin-current. Optimal AC and DC spin-current protocols are given by Eqs. (4.15) and (3.21). E_c is calculated using Eqn. (5.9).

5.3.2 Practical solutions

Equations (5.6) can also be used to calculate optimal protocols numerically for any anisotropy and pinned layer configuration, given some assumed form for the energy dependence of each parameter. Figure 5.5 shows such a solution for the uniaxial anisotropy case discussed earlier in this chapter and shown in Fig. 5.2. Note the excellent agreement between the numerical and simulated results.

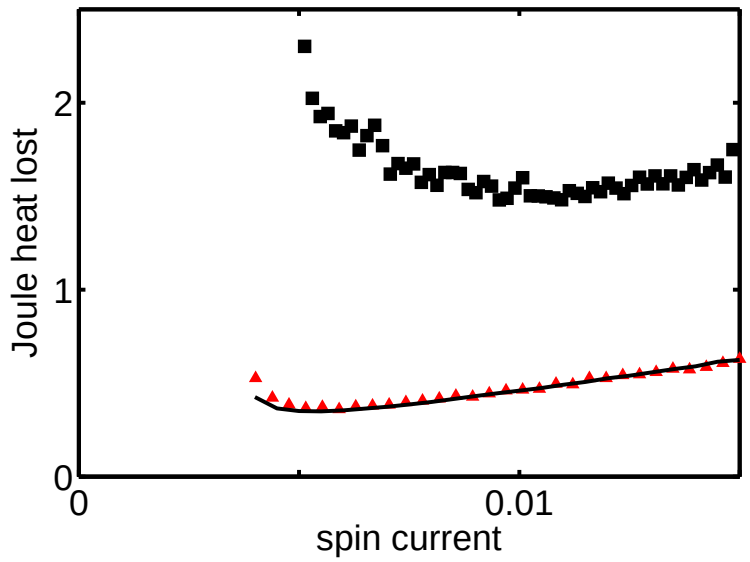

Figure 5.5: Optimal JHL calculated numerically using Eqs. (5.6) as a function of spin-current strength ($\mathcal{I}_\mathrm{s}/M_\mathrm{s}$) along with simulated values for DC (black squares) and AC/DC (red triangles) spin-current strategies, same as in Fig. 5.2.

The AC and DC pulse times, t_AC and t_DC, for these protocols are shown in Fig. 5.6 along with the simulated values. Recall, for these simulations $\overline{\mathcal{I}}_\mathrm{s}$, $\widetilde{\mathcal{I}}_\mathrm{s}$, and ω were held constant for the duration of each pulse and the strengths of the AC and DC spin-currents were taken to be equal, $\overline{\mathcal{I}}_\mathrm{s} = \widetilde{\mathcal{I}}_\mathrm{s}$. The first of these restrictions defines how $\overline{\mathcal{I}}_\mathrm{s}$, $\widetilde{\mathcal{I}}_\mathrm{s}$, and ω behave under integration, while the second combines Eqs. (5.6a) and (5.6c).

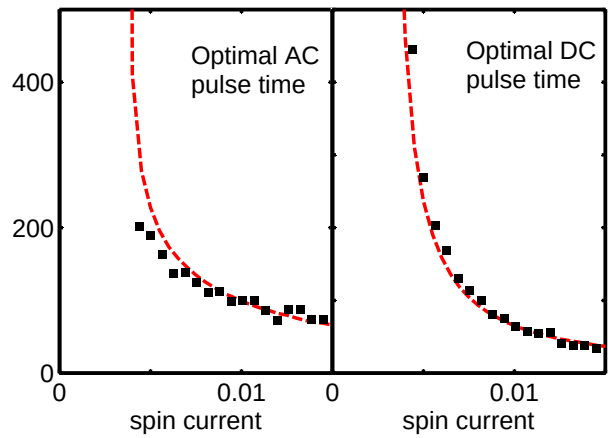

Figure 5.6: Simulated AC (left) and DC (right) pulse times (black squares) in units of $(\gamma M_{\rm s})^{-1}$ that give the minimum JHL as a function of spin-current strength ($\mathcal{I}_{\rm s}/M_{\rm s}$). Red dashed lines represent optimal pulse times calculated numerically using Eqs. (5.6) at each spin-current strength. Same parameters as Fig. 5.5.

For general solutions to Eqs. (5.6) where the parameters are held constant for the duration of each respective pulse, the set of constraints used to confine the AC and DC practical solutions may be employed to limit the range of each optimal value with $E_{\rm b} \to E_{\rm c}$ in the AC case and $E_0 \to E_{\rm c}$ in the DC case. Performing these substitutions constrains on the optimal parameters as follows: the optimal DC spin-current strength must lie in the range

$$\max\left\{\overline{\mathcal{I}}_{\rm min}(E_{\rm c}), \overline{\mathcal{I}}_c'(E_{\rm c})\right\} < \overline{\mathcal{I}}_{\rm opt} < 2\overline{\mathcal{I}}_c'(E_{\rm c})\,. \tag{5.10}$$

Here

$$\begin{aligned} \overline{\mathcal{I}}_c'(E_{\rm c}) &= \max\left\{\overline{\mathcal{I}}_{\rm c}(E), |E_{\rm c} < E < E_{\rm b}\right\}\,; \\ \overline{\mathcal{I}}_{\rm min}(E_{\rm c}) &= 2\min\left\{\overline{\mathcal{I}}_{\rm c}(E)|E_{\rm c} < E < E_{\rm b}\right\}\,, \end{aligned} \tag{5.11}$$

where $\overline{\mathcal{I}}_c'(E_{\rm c})$ is the critical current for a free layer with initial energy $E_{\rm c}$, and $\mathcal{I}_c(E)$ is the local critical current given by Eqn. (3.12). Similarly, the optimal AC spin-current strength must lie in the range

$$\widetilde{\mathcal{I}}_{\rm c}(E_{\rm c}, \omega) < \widetilde{\mathcal{I}}_{\rm opt} < \widetilde{\mathcal{I}}_{\rm max}(E_{\rm c}, \omega)\,, \tag{5.12}$$

where the upper and lower bounds are given by

$$\begin{aligned}\widetilde{\mathcal{I}}_{\mathrm{c}}(E_{\mathrm{c}},\omega) &= \left(\widetilde{\mathcal{I}}_{\mathrm{c}}^{2}(E_{\mathrm{c}}) + \Big(\mathcal{F}_{\Omega}(E_{\mathrm{c}}) - \mathcal{F}_{\omega}(E_{\mathrm{c}},\omega)\Big)^{2}\right)^{1/2} ;\\ \widetilde{\mathcal{I}}_{\max}(E_{\mathrm{c}},\omega) &= \left(2\widetilde{\mathcal{I}}_{\mathrm{c}}(E_{\mathrm{c}},\omega)\left(\widetilde{\mathcal{I}}_{\mathrm{c}}(E_{\mathrm{c}},\omega) + \widetilde{\mathcal{I}}_{\mathrm{c}}(E_{\mathrm{c}})\right)\right)^{1/2} ,\end{aligned} \tag{5.13}$$

and $\widetilde{\mathcal{I}}_{\mathrm{c}}(E)$ is the AC critical current when $\omega = \Omega(E)$, given by Eqn. (4.18). Lastly, the optimal AC signal frequency must lie in the range

$$\omega_2 < \omega_{\mathrm{opt}} < \Omega_0 , \tag{5.14}$$

where $\Omega_0 = \Omega(0)$ is the natural frequency of the free layer and ω_2 is the upper bifurcation frequency.

Chapter 6

Discussion

In this chapter I discuss the results presented in chapters 3, 4, and 5 and present additional material that can be used to address some of the limitations and observations of the approach taken.

The key result of this thesis is that the optimal trajectory in all three cases is the time-reversed purely relaxational trajectory of the free layer magnetization in the absence of spin-torque. This is a direct consequence of the optimal spin-current strength being exactly twice the local critical current needed to perfectly cancel damping. As it turns out, this result is not strongly dependent on the approximations used throughout this thesis to calculate the optimal current protocols but is instead dependent on the exponential dependencies of the power dissipated, $P \propto \mathcal{I}_{\mathrm{s}}^{n_{\mathrm{P}}}$, where n_P has been taken to be 2, i.e., Joule heating, and of the work done, $\dot{E} \propto \mathcal{I}_{\mathrm{s}}^{n_{\mathrm{W}}}$, which has been taken to be 1. I discuss this in more detail in section 6.1.

Another important aspect to the optimization results shown is the dependence on thermal noise. The optimal switching protocols presented here are based on the assumption that thermal effects play a minor role in the switching process. This certainly is not always the case. Clearly, random fluctuation can reduce the effectiveness of certain switching strategies, e.g., AC spin-current strategies shown in chapter 4 were much more sensitive to thermal effects than the DC or AC/DC strategies shown in chapters 3 and 5. In section 6.2, tools for addressing this are presented by deriving Langevin equations of motion along with Fokker-Planck (FP) equations for the time evolution of the probability density for both AC and DC spin-current strategies.

Finally, in section 6.3 I discuss in more detail the φ-averaging procedure employed throughout this thesis and derive criteria for when it is not applicable. This is essential for establishing the validity of the optimal spin-current strategies presented throughout this thesis.

6.1 Optimization

That the energy-dependent optimal spin-current protocols from the previous three chapters cause the magnetization to follow the time-reverse relaxation trajectory should not come as a surprise. This feature is a direct result of the fact that the rate of work done by the spin-current on the free layer is proportional to spin-current, $\dot{E} \propto \mathcal{I}_{\mathrm{s}}$, for currents large enough to overcome damping and that the power dissipated by Joule heating is proportional to the spin-current squared, $P \propto \mathcal{I}_{\mathrm{s}}^2$. For instance, consider the fictitious system with work and power relations

$$\begin{aligned} \dot{E} &= -\alpha U(E,\varphi) + {\mathcal{I}_{\mathrm{s}}}^{n_{\mathrm{W}}} V(E,\varphi)\,, \\ P &\propto {\mathcal{I}_{\mathrm{s}}}^{n_{\mathrm{P}}}\,, \end{aligned} \tag{6.1}$$

where $n_{\mathrm{P}} > n_{\mathrm{W}} > 0$. Treating the free layer as a heat engine, the instantaneous efficiency of the spin-current is

$$Q(E) = \frac{-\alpha U(E,\varphi) + {\mathcal{I}_{\mathrm{s}}}^{n_{\mathrm{W}}} V(E,\varphi)}{{\mathcal{I}_{\mathrm{s}}}^{n_{\mathrm{P}}}}\,. \tag{6.2}$$

For $\mathcal{I}_{\mathrm{s}} \leq \mathcal{I}_{\mathrm{c}}$ the efficiency is $Q \leq 0$, and for $\mathcal{I}_{\mathrm{s}} \to \infty$, $Q \to 0$. This means the maximum value of the efficiency can be found by solving $\partial_{\mathcal{I}_{\mathrm{s}}} Q = 0$, which gives

$$\dot{E} = \left(\frac{n_{\mathrm{W}}}{n_{\mathrm{P}} - n_{\mathrm{W}}}\right) \alpha U(E,\varphi)\,. \tag{6.3}$$

One can easily verify that $n_{\mathrm{W}} = 1$ and $n_{\mathrm{P}} = 2$ produces the desired result. This generic result means, so long as the power dissipated by the spin-current and the rate of work done by the spin-current on the free layer scale with constant exponents, the optimal spin-current pulse strategy will reproduce the time-reversed relaxation trajectory with time re-scaled as $t \to t\, n_{\mathrm{W}} / (n_{\mathrm{P}} - n_{\mathrm{W}})$. This result may have applications in thermally assisted magnetic reversal in perpendicular anisotropy materials where Joule heating from the applied current can weaken the free layer anisotropy, thus degrading the potential barrier during the switch [119].

6.2 Effects of thermal noise during switching

Stochastic effects on the switching process, such as thermal noise, can be included into the energy/angle representation for the LLGS equation presented in chapters 3 and 4 by including the random field $\mathbf{h}$, characterized by Eqn. (2.19), into the effective field. When rewritten in terms of the energy and angle equations of motion as discussed in Sec. 3.3, the resulting stochastic equations of motion with multiplicative noise are

$$\begin{aligned}\dot{E} &= -\alpha U(E,\varphi) + \mathcal{I}_{\mathrm{s}} V(E,\varphi) + \mathbf{g}_E(E,\varphi)\cdot\mathbf{h}(t)\,;\\ \dot{\varphi} &= \Omega(E) + \mathcal{I}_{\mathrm{s}} W(E,\varphi) + \mathbf{g}_\varphi(E,\varphi)\cdot\mathbf{h}(t)\,,\end{aligned} \tag{6.4}$$

where the noise-multiplying vectors are given by

$$\mathbf{g}_E = \mathbf{\Gamma}_{\mathrm{LL}}\,; \qquad \mathbf{g}_\varphi = \Omega(E)\frac{\mathbf{M}\times\mathbf{\Gamma}_{\mathrm{LL}}}{\left|\mathbf{\Gamma}_{\mathrm{LL}}\right|^2}\,. \tag{6.5}$$

Using Eqs. (6.4), a Fokker-Planck equation can be obtained for the probability density $\mathcal{P}(E,\varphi,t)$ that the magnetization will be at the point $\mathbf{M}(E,\varphi)$ at time t using Stratonovich regularization [120]

$$\begin{aligned}\dot{\mathcal{P}} = &-\partial_E\Big[(-\alpha U + \mathcal{I}_{\mathrm{s}} V + k_E)\mathcal{P} - D\partial_E\left(\left|\mathbf{g}_E\right|^2\mathcal{P}\right)\Big]\\ &-\partial_\varphi\Big[(\Omega + W + k_\varphi)\mathcal{P} - D\partial_\varphi\left(\left|\mathbf{g}_\varphi\right|^2\mathcal{P}\right)\Big]\,,\end{aligned} \tag{6.6}$$

where the dependencies on E and φ are understood. Here the orthogonality relation $\mathbf{g}_E\cdot\mathbf{g}_\varphi = 0$ has been used, and the diffusion coefficient $D = \alpha k_{\mathrm{B}}T/\gamma M_{\mathrm{s}}\mathcal{V}$ is determined by the equilibrium correlator of the stochastic magnetic field, Eqn. (2.14). The "false" forces k_E and k_φ are

$$k_E = D(\partial_E - \partial_E \ln\Omega)\left|\mathbf{g}_E\right|^2\,; \qquad k_\varphi = D\partial_\varphi\left|\mathbf{g}_\varphi\right|^2\,, \tag{6.7}$$

calculated using $k_\mu = D\sum_\nu(\partial_\nu\mathbf{g}_\mu)\cdot\mathbf{g}_\nu$ [120, 82], where $\mu,\nu = E,\varphi$. Substituting Eqs. (6.7) into Eqn. (6.6) the Fokker-Planck equation simplifies to

$$\begin{aligned}\dot{\mathcal{P}} = &-\partial_E\Big[(-\alpha U + \mathcal{I}_{\mathrm{s}} V - D_E\partial_E\ln\Omega)\mathcal{P} - D_E\partial_E\mathcal{P}\Big]\\ &-\partial_\varphi\Big[(\Omega + \mathcal{I}_{\mathrm{s}} W)\,\mathcal{P} - D_\varphi\partial_\varphi\mathcal{P}\Big]\,,\end{aligned} \tag{6.8}$$

where the two diffusion coefficients are $D_\mu(E,\varphi) = D\left|\mathbf{g}_\mu\right|^2$.

For DC spin-currents, in the limit where $\dot{E} \ll \dot{\varphi}$ one expects that on the fast time-scale of the precession period P the distribution nearly equilibrates in the angular direction and then evolves slowly along the energy direction. This implies that at long times $t \gg P$ one has

$$\dot{\mathcal{P}} = -\partial_E \Big[(-\alpha U + \mathcal{I}_{\rm s} \overline{V}_{\rm x} - \mathcal{D}_E \partial_E \ln \Omega) \mathcal{P} - \mathcal{D}_E \partial_E \mathcal{P} \Big] , \tag{6.9}$$

where U and $\overline{V}_{\rm x}$ are the φ-averaged generalized forces given by Eqs. (3.9) and $\mathcal{D}$ is given by

$$\mathcal{D}_E = \frac{D}{2\pi} \int_0^{2\pi} |\mathbf{g}_E|^2 \, d\varphi = D \frac{\Omega(E)}{2\pi} \oint \mathbf{\Gamma}_{\rm LL} \cdot d\mathbf{M} = \gamma M_{\rm s} D \, U(E) \, . \tag{6.10}$$

Similarly for AC spin-currents in this regime, the FP equation becomes

$$\begin{aligned} \dot{\mathcal{P}} = & - \partial_E \Big[\Big(-\alpha U + \mathcal{I}_{\rm s} \big(\widetilde{V}_{\rm y} \cos\phi - \widetilde{V}_{\rm z} \sin\phi \big) + \mathcal{D}_E \partial_E \ln \Omega \Big) \mathcal{P} - \mathcal{D}_E \partial_E \mathcal{P} \Big] \\ & - \partial_\phi \Big[\Big(\Omega - \omega + \mathcal{I}_{\rm s} \big(\widetilde{W}_{\rm y} \sin\phi - \widetilde{W}_{\rm z} \cos\phi \big) \Big) \mathcal{P} - \mathcal{D}_\phi \partial_\phi \mathcal{P} \Big] \, , \end{aligned} \tag{6.11}$$

where U is the φ-averaged generalized force given by Eqn. (3.9) and $\widetilde{V}$ and $\widetilde{W}$ are the φ-averaged generalized ST forces given by Eqs. (4.4) and (4.5). Here $\mathcal{P} = \mathcal{P}(E, \phi, t)$ and $\mathcal{D}_\phi$ is given by

$$\mathcal{D}_\phi = \frac{D}{2\pi} \int_0^{2\pi} |\mathbf{g}_\varphi|^2 \, d\varphi = \gamma M_{\rm s}^2 D \frac{\Omega^3(E)}{2\pi} \oint \frac{\mathbf{\Gamma}_{\rm LL} \cdot d\mathbf{M}}{\big| \mathbf{\Gamma}_{\rm LL} \big|^4} \, . \tag{6.12}$$

When $\mathcal{I}_{\rm s} = 0$ notice the equilibrium fluctuation dissipation theorem dictates $D = \alpha k_{\rm B} T / M_{\rm s} \gamma \mathcal{V}$; thus, $\mathcal{D}_E = \alpha k_{\rm B} T U(E) / \mathcal{V}$. As a result of this remarkable relation, the equilibrium stationary solution of the 1D FP Eqn. (6.9) takes the universal form

$$\mathcal{P}(E) = \frac{2\pi}{Z} \exp \left[-\frac{E\mathcal{V} - k_{\rm B} T \ln \Omega(E)}{k_{\rm B} T} \right] = \frac{P(E)}{Z} \exp \left[-\frac{E\mathcal{V}}{k_{\rm B} T} \right] , \tag{6.13}$$

where Z is a normalization factor [92, 95]. The very last term here is, of course, the Boltzmann exponent.

For additional information regarding this and other such FP approaches to ST dynamics in the presence of stochastic noise, see Refs. [81, 94, 83, 121, 92, 97, 122, 98].

6.3 Limitations on φ-averaging technique

The averaging technique used throughout this thesis to eliminate the φ dependence of the free layer dynamics has limitations on when its application is acceptable. For

example, for switching time close to the free layer precessional period this technique cannot be used since the free layer covers a large range of energy over a single precessional period. This approximation can also fail for cases where strong oscillatory spin-torque terms are present. For these cases higher order, φ-dependent, terms must be included in the equations of motion in order to accurately model the dynamics of the free layer.

To deal with these cases, one can treat the φ-averaged equations of motion for energy E and φ as the first terms in a Fourier series for the LLGS equation in terms of the angular variable φ:

$$\begin{aligned} \varepsilon\dot{E} &= \varepsilon f_0(E) + \sum_{n=1}^{\infty} \varepsilon^n \left(f_n(E) e^{in\varphi} + f_{\text{-}n}(E) e^{-n\varphi} \right) \; ; \\ \dot{\varphi} &= g_0(E) + \sum_{n=1}^{\infty} \varepsilon^{n-1} \left(g_n(E) e^{in\varphi} + g_{\text{-}n}(E) e^{-in\varphi} \right) \; . \end{aligned} \tag{6.14}$$

Here ε is an indexing factor used to indicate the assumed relative strengths of each term in the expansion with the understanding that $\varepsilon \ll 1$. Each term in this expansion is calculated using the standard Fourier transformation

$$f_n(E) = \frac{1}{2\pi} \oint d\varphi \, \dot{E} \, e^{-in\varphi} \, , \qquad g_n(E) = \frac{1}{2\pi} \oint d\varphi \, \dot{\varphi} \, e^{-in\varphi} \, . \tag{6.15}$$

The φ-averaged equations of motion given by Eqs. (3.8) and (4.3) are encompassed in the terms f_0 and g_0; thus the remaining terms contain information on the dynamics ignored in this approximation.

So long as the assumed relative strengths for each term in their Fourier expansion, given in powers of the indexing factor ε, are correct, these extra factors can be ignored to good accuracy. Of course, this is not always the case. To quantify the impact of these dropped terms, one may consider solutions to Eqs. (6.14) of the form

$$\begin{aligned} E &= E_0 + \varepsilon E_1 + \varepsilon^2 E_2 + \cdots + \varepsilon^N E_N \, ; \\ \varphi &= \varphi_0 + \varepsilon \varphi_1 + \varepsilon^2 \varphi_2 + \cdots + \varepsilon^N \varphi_N \, . \end{aligned} \tag{6.16}$$

So long as $\varepsilon E_1 \ll E_0$ through the switching process, the approximation remains valid. Expanding each term in Eqs. (6.14) about (E_0, φ_0) and grouping in powers of ε gives

$$\begin{aligned} f_n(E) e^{in\varphi} &= f_n(E_0 + \varepsilon E_1 + \cdots + \varepsilon^N E_N) e^{in\left(\varphi_0 + \varepsilon\varphi_1 + \cdots + \varepsilon^N \varphi_N\right)} \\ &= f_n(E_0) e^{in\varphi_0} + \varepsilon e^{in\varphi_0} \left(in\varphi_1 f_n(E_0) + E_1 f_n'(E_0) \right) + \mathcal{O}\left(\varepsilon^2\right) \, , \end{aligned} \tag{6.17}$$

and

$$\begin{aligned} g_n(E)e^{in\varphi} &= g_n(E_0 + \varepsilon E_1 + \cdots + \varepsilon^N E_N)e^{in\left(\varphi_0 + \varepsilon\varphi_1 + \cdots + \varepsilon^N \varphi_N\right)} \\ &= g_n(E_0)e^{in\varphi_0} + \varepsilon e^{in\varphi_0}\left(in\varphi_1 g_n(E_0) + E_1 g_n'(E_0)\right) + \mathcal{O}\left(\varepsilon^2\right) . \end{aligned} \tag{6.18}$$

Substituting Eqn. (6.16) and Eqs. (6.17) and (6.18) into Eqs. (6.14) the first two terms for the energy equation of motion are

$$\begin{aligned} \varepsilon^1 &: \dot{E}_0 = f_0(E_0) , \\ \varepsilon^2 &: \dot{E}_1 = E_1 f_0'(E_0) + f_1(E_0)e^{i\varphi_0} + f_{\text{-}1}(E_0)e^{-i\varphi_0} , \end{aligned} \tag{6.19}$$

and the first two terms for the angular equation of motion are

$$\begin{aligned} \varepsilon^0 &: \dot{\varphi}_0 = g_0(E_0) , \\ \varepsilon^1 &: \dot{\varphi}_1 = E_1 g_0'(E_0) + g_1(E_0)e^{i\varphi_0} + g_{\text{-}1}(E_0)e^{-i\varphi_0} . \end{aligned} \tag{6.20}$$

The ε^0 term in Eqn. (6.20) and the ε^1 term in Eqn. (6.19) are the φ-averaged equations of motion given by Eqs. (3.8) and (4.3). The differential equations for the remaining terms with higher powers of ε can be solved using the solutions to lower-order terms.

One may notice the equation of motion for E_1 has the form of a forced oscillator. Taking the solution for E_0 and φ_0 as known, E_1 can be shown to oscillate with a magnitude of

$$|E_1|^2 = \frac{|f_1(E)|^2}{g_0^2(E) + {f_0'}^2(E)} , \tag{6.21}$$

where the indexing factor ε has been dropped to allow for direct comparison with E_0. Therefore, for DC spin-currents $g_0(E) = \Omega(E)$ and for AC spin-currents $g_0 = \omega$, so long as $g_0 \gg f_0'$, Eqn. (6.21) simplifies to

$$|E_1| = |f_1(E)| \frac{P(E)}{2\pi} . \tag{6.22}$$

Recall for large energies $\Omega(E) \to 0$; thus E_1 diverges unless either f_0' is large or $|f_1(E)|$ goes to zero equally fast. Figure 6.1 plots E_1 for DC spin-currents polarized equally along the easy-axis and easy-plane directions in free layers with uniaxial and strong easy-plane anisotropy. Notice for the free layer with strong easy-plane anisotropy E_1 is close to E_0

throughout the entire energy range. This means for $\eta_x = \eta_z$ the φ-averaging technique is not applicable for free layers with strong easy-plane anisotropy, as was observed to be the case in Fig. 3.4. Alternatively, for free layers with uniaxial anisotropy, $E_1 \ll E_0$ throughout the energy range; thus the approximation works well as supported by the analytic and simulated results from the previous three chapters.

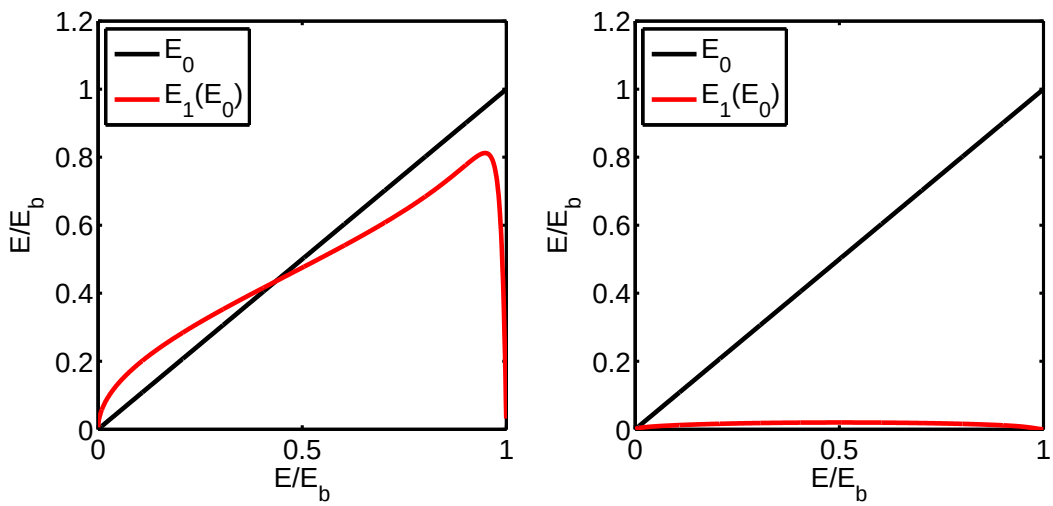

Figure 6.1: E_0 (black) and E_1 (red) calculated numerically using Eqn. (6.21) for DC spin-current with $\eta_x = \eta_z$ and $\mathcal{I}_s = 2\mathcal{I}_c$ for a free layer with strong easy-plane anisotropy, $H_x = 0.033M_s$ and $H_x = M_s$, (left) and for free layer with uniaxial anisotropy, $H_x = 0.5M_s$ (right).

Figure 6.2 plots E_1 for AC spin-currents polarized equally along the easy-axis and easy-plane directions in free layers with uniaxial and strong easy-plane anisotropy. Here both the uniaxial and strong easy-plane free layers have $E_1 \ll E_0$; thus the motion of the free layer is well approximated by the φ-averaged equations of motion as evident by the analytic and simulated results from the previous three chapters. One may notice though that for both free layers shown in Fig. 6.2, E_1 near the energy barrier can be on order of $E_b - E_0$; thus the oscillations of the free layer may exceed the energy barrier, causing the switch happen either earlier or later than expected depending on the phase of the E_1 oscillations.

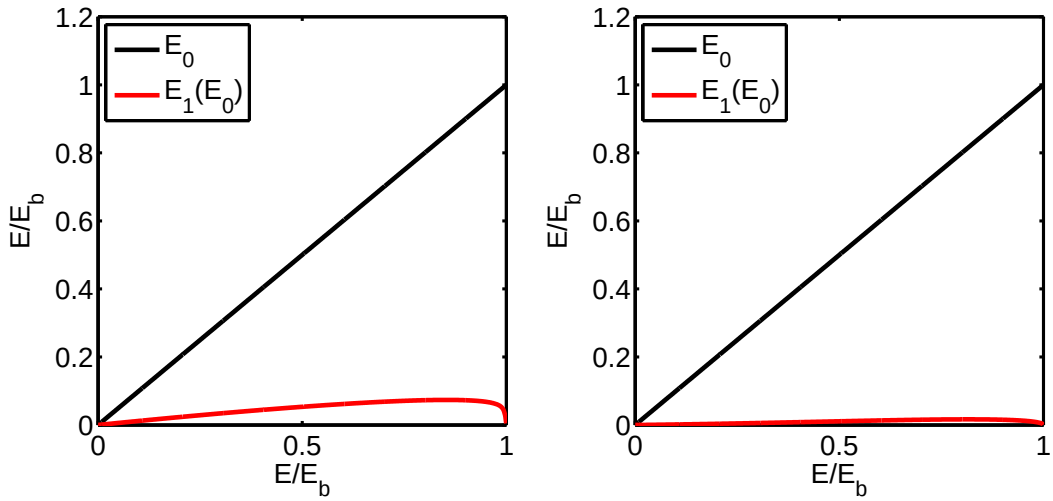

Figure 6.2: E_0 (black) and E_1 (red) calculated numerically using Eqn. (6.21) for AC spin-current with $\eta_x = \eta_z$ and $\mathcal{I}_s = 2\mathcal{I}_c$ for free layer with strong easy-plane anisotropy, $H_x = 0.033M_s$ and $H_x = M_s$, (left) and for free layer with uniaxial anisotropy, $H_x = 0.5M_s$ (right).

Chapter 7

Conclusion

In conclusion, I have explored the dynamics and optimization of spin-torque switching in MTJs. The theoretical descriptions presented here serve as powerful tools for analyzing the effects of spin-current polarization and free layer anisotropy on the switching process.

In terms of the dynamics: for DC spin-currents this analysis accurately reproduces the switching trajectory and behavior of the free layer energy. It also provides a simple means for calculating the critical current in free layers with arbitrary anisotropy. For AC spin-currents this analysis shown how the transient motion of the free layer behaves like a damped harmonic oscillator with the energy and relative phase acting like coordinate and momentum. It also provides a means of calculating the critical current and explains the frequency dependence of the equilibrium energy and transient motion in terms of a critical frequency that corresponds to the upper bifurcation frequency of the free layer.

In terms of minimizing the JHL from switching, the key result is that the optimal energy trajectory of the free layer is exactly the time-reversed relaxation trajectory of the free layer in the absence of ST from the energy barrier to the thermal equilibrium energy. For DC spin-currents, this is achieved by applying a current exactly twice the local critical current needed to exactly cancel the damping. For AC spin-currents, this is achieved by applying an AC signal with frequency that exactly matches the free layer energy-dependent natural frequency in the absence of ST. This causes the free layer to become phase-locked with the AC signal such that it maximizes the strength of the ST. The optimal current strength is then exactly twice the AC local critical current. For combine AC and DC spin-current pulses, the results of Fig. 5.4 clearly show there may

be large gains in efficiency to be found by using AC spin-currents early in the switching process.

References

[1] M. N. Baibich, J. M. Broto, A. Fert, F. Nguyen Van Dau, F. Petroff, P. Eitenne, G. Creuzet, A. Friederich, and J. Chazelas. *Phys. Rev. Lett.*, 61:2472, 1988.

[2] G. Binasch, P. Grnberg, F. Saurenbach, and W. Zinn. *Phys. Rev. B*, 39:4828, 1988.

[3] J. C. Slonczewski. *J. Magn. Magn. Mater.*, 159:L1, 1996.

[4] L. Berger. *Phys. Rev. B*, 54:9353, 1996.

[5] E. B. Myers, D. C. Ralph, J. A. Katine, R. N. Louie, and R. A. Buhrman. *Science*, 285:867, 1999.

[6] M. Tsoi, A. G. M. Jansen, J. Bass, W.-C. Chiang, M. Seck, V. Tsoi, and P. Wyder. *Phys. Rev. Lett.*, 80:4281, 1998.

[7] Y. Tserkovnyak, A. Brataas, and G. E. W. Bauer. *Phys. Rev. Lett.*, 88:117601, 2002.

[8] W. H. Rippard, M. R. Pufall, and S. E. Russek. *Phys. Rev. B*, 74:224409, 2006.

[9] A. V. Nazarov, H. M. Olson, H. Cho, K. Nikolaev, Z. Gao, S. Stokes, and B. B. Pant. *Appl. Phys. Lett.*, 88:162504, 2006.

[10] Q. Mistral, J.-V. Kim, T. Devolder, P. Crozat, C. Chappert, J. A. Katine, M. J. Carey, , and K. Ito. *Appl. Phys. Lett.*, 88:192507, 2006.

[11] V. Tiberkevich, J. V. Kim, and A. N. Slavin. *Appl. Phys. Lett.*, 91:192506, 2007.

[12] C. Boone, J. A. Katine, J. R. Childress, J. Zhu, X. Cheng, and I. N. Krivorotov. *Phys. Rev. B*, 79:140404, 2009.

[13] S. Mizukami, Y. Ando, and T. Miyazaki. *Jpn. J. Appl. Phys.*, 40:580, 2001.

[14] J. V. Kim, V. Tiberkevich, and A. N. Slavin. *Phys. Rev. Lett.*, 100:017207, 2008.

[15] J. C. Slonczewski and J. Z. Sun. *J. Magn. Magn. Mater.*, 310:169, 2007.

[16] A. L. Chudnovskiy, J. Swiebodzinski, and A. Kamenev. *Phys. Rev. Lett.*, 101:066601, 2008.

[17] Y. Tserkovnyak, A. Brataas, and G. E. Bauer. *J. Magn. Magn. Mater.*, 320:1282, 2008.

[18] D. C. Ralph and M. D. Stiles. *J. Magn. Magn. Materials*, 320:1190, 2008.

[19] S. Hernández and R. H. Victora. *Appl. Phys. Lett.*, 97:062506, 2010.

[20] J. C. Sankey, I. N. Krivorotov, S. I. Kiselev, P. M. Braganca, N. C. Emley, R. A. Buhrman, and D. C. Ralph. *Phys. Rev. B*, 72:224427, 2005.

[21] T. J. Silva and W. H. Rippard. *J. Magn. Magn. Mater.*, 320:1260, 2008.

[22] K. V. Thadani, G. Finocchio, Z.-P. Li, O. Ozatay, J. C. Sankey, I. N. Krivorotov, Y.-T. Cui, R. A. Buhrman, and D. C. Ralph. *Phys. Rev. B*, 78:024409, 2008.

[23] V. S. Pribiag, G. Finocchio, B. Williams, D. C. Ralph, and R. A. Buhrman. *Phys. Rev. B*, 80:180411, 2009.

[24] P. M. Braganca, B. A. Gurney, B. A. Wilson, J. A. Katine, S. Maat, and J. R. Childress. *Nanotechnology*, 21:235202, 2010.

[25] S. Bonetti, V. Tiberkevich, G. Consolo, G. Finocchio, P. Muduli, F. Mancoff, A. Slavin, and J. Akerman. *Phys. Rev. Lett.*, 105:217204, 2010.

[26] L. Liu, C.-F. Pai, D. C. Ralph, and R. A. Buhrman. *Phys. Rev. Lett.*, 109:186602, 2012.

[27] L. Fu, Z. X. Cao, S. Hemour, K. Wu, D. Houssameddine, W. Lu, S. Pistorius, Y. S. Gui, and C.-M. Hu. *Appl. Phys. Lett.*, 101:232406, 2012.

[28] G. Tatara and H. Kohno. *Phys. Rev. Lett.*, 92:086601, 2004.

[29] Z. Li and S. Zhang. *Phys. Rev. B*, 70:024417, 2004.

[30] S. S. P. Parkin, M. Hayashi, and L. Thomas. *Science*, 320:190, 2008.

[31] G. Tatara, H. Kohno, and J. Shibata. *Phys. Rep.*, 468:213, 2008.

[32] G. S. D. Beach, M. Tsoi, and J. L. Erskine. *J. Magn. Magn. Mater.*, 320:1272, 2008.

[33] K. M. D. Hals, A. K. Nguyen, and A. Brataas. *Phys. Rev. Lett.*, 102:256601, 2009.

[34] C. Burrowes, A. P. Mihai, D. Ravelosona, J.-V. Kim, C. Chappert, L. Vila, A. Marty, Y. Samson, F. Garcia-Sanchez, L. D. Buda-Prejbeanu, I. Tudosa, E. E. Fullerton, and J.-P. Attan. *Nat. Phys.*, 6:17, 2010.

[35] S. I. Kiselev, J. C. Sankey, I. N. Krivorotov, N. C. Emley, R. J. Schoelkopf, R. A. Buhrman, and D. C. Ralph. *Nature*, 425:380, 2003.

[36] R. Matsumoto, A. Fukushima, K. Yakushiji, S. Yakata, T. Nagahama, H. Kubota, T. Katayama, Y. Suzuki, K. Ando, S. Yuasa, B. G., V. Cros, J. Grollier, and A. Fert. *Phys. Rev. B*, 80:174405, 2009.

[37] S. Tehrani, B. Engel, J. M. Slaughter, E. Chen, M. DeHerrera, M. Durlam, P. Naji, R. Whig, J. Janesky, and J. Calder. *Magnetics, IEEE Transactions on*, 36:2752, 2000.

[38] N. Nishimura, T. Hirai, A. Koganei, T. Ikeda, K. Okano, Y. Sekiguchi, and Y. Osada. *J. Appl. Phys.*, 91:5246, 2002.

[39] W. H. Rippard, M. R. Pufall, S. Kaka, S. E. Russek, and T. J. Silva. *Phys. Rev. Lett.*, 92:027201, 2004.

[40] S. Yakata, H. Kubota, Y. Suzuki, K. Yakushiji, A. Fukushima, S. Yuasa, and K. Ando. *J. Appl. Phys.*, 105:07D131, 2009.

[41] C. Wang, Y.-T. Cui, J. A. Katine, R. A. Buhrman, and D. C. Ralph. *Nat. Phys.*, 7:496, 2011.

[42] M. Johnson and R. H. Silsbee. *Phys. Rev. B*, 37:5326, 1988.

[43] Robert C. O'Handley. *Modern Magnetic Materials: Principles and Applications*. Wiley-Interscience, 1999.

[44] F. J. Jedema, A. T. Filip, and B. J. van Wees. *Nature*, 410:345, 2001.

[45] X. Waintal, E. B. Myers, P. W. Brouwer, and D. C. Ralph. *Phys. Rev. B*, 62:12317, 2000.

[46] J. A. Katine, F. J. Albert, R. A. Buhrman, E. B. Myers, and D. C. Ralph. *Phys. Rev. Lett.*, 84:3149, 2000.

[47] J. Grollier, V. Cros, A. Hamzic, J. M. George, H. Jaffres, A. Fert, G. Faini, J. Ben Youssef, and H. Legall. *Appl. Phys. Lett.*, 78:3663, 2001.

[48] J. Z. Sun. *Phys. Rev. B.*, 62:570, 2000.

[49] S. Mangin, D. Ravelosona, J. A. Katine, M. J. Carey, B. D. Terris, and Eric E. Fullerton. *Nat. Mater.*, 5:210, 2006.

[50] B. Ozyilmaz, A. D. Kent, D. Monsma, J. Z. Sun, M. J. Rooks, and R. H. Koch. *Phys. Rev. Lett.*, 91:067203, 2003.

[51] S. Urazhdin, N. O.Birge, W. P. Pratt, and J. Bass. *Phys. Rev. Lett.*, 91:146803, 2003.

[52] M. Hosomi, H. Yamagishi, T. Yamamoto, K. Bessho, Y. Higo, K. Yamane, H. Yamada, M. Shoji, H. Hachino, C. Fukumoto, H. Nagao, and H. Kano. *IEDM Tech. Dig.*, page 459, 2005.

[53] E. B. Myers, F. J. Albert, J. C. Sankey, E. Bonet, R. A. Buhrman, and D. C. Ralph. *Phys. Rev. Lett.*, 89:196801, 2002.

[54] T. Seki, S. Mitani, K. Yakushiji, and K. Takanashi. *Appl. Phys. Lett.*, 88:172504, 2006.

[55] S. Yuasa and D. D. Djayaprawira. *J. Phys. D: Appl. Phys.*, 40:R337, 2007.

[56] A. A. Tulapurkar, T. Devolder, K. Yagami, P. Crozat, C. Chappert, A. Fukushima, and Y. Suzuki. *Appl. Phys. Lett.*, 85:5358, 2004.

[57] A. D. Kent, B. Özyilmaz, and E. del Barco. *Appl. Phys. Lett.*, 84:3897, 2004.

[58] S. Matsunaga, K. Hiyama, A. Matsumoto, S. Ikeda, H. Hasegawa, K. Miura, J. Hayakawa, T. Endoh, H. Ohno, and T. Hanyu. *Applied Physics Express*, 2:023004, 2009.

[59] G.-F. Zhang, G.-H. Guo, X.-G. Wang, Y.-Z. Nie, and Z.-X. Li. *AIP Advances*, 2:042127, 2012.

[60] Y.-T. Cui, J. C. Sankey, C. Wang, K. V. Thadani, Z.-P. Li, R. A. Buhrman, and D. C. Ralph. *Phys. Rev. B*, 77:214440, 2008.

[61] S.-M. Seo and K.-J. Lee. *Appl. Phys. Lett.*, 101:062408, 2012.

[62] D. Bedau, H. Liu, J.-J. Bouzaglou, A. D. Kent, J. Z. Sun, J. A. Katine, E. E. Fullerton, and S. Mangin. *Appl. Phys. Lett.*, 96:022514, 2010.

[63] D. E. Nikonov, G. I. Bourianoff, G. Rowlands, and I. N. Krivorotov. *J. Appl. Phys.*, 107:113910, 2010.

[64] M. Marins de Castro, R. C. Sousa, S. Bandiera, C. Ducruet, A. Chavent, S. Auffret, C. Papusoi, I. L. Prejbeanu, C. Portemont, L. Vila, U. Ebels, B. Rodmacq, and B. Dieny. *J. Appl. Phys.*, 111:07C912, 2012.

[65] K. L. Wang, J. G. Alzate, and P. K. Amiri. *J. Phys. D: Appl. Phys.*, 46:074003, 2013.

[66] L. D. Landau and E. M. Lifshitz. *Phys. Z. Sowj.*, 8:153, 1935.

[67] A. Misra and R. H. Victora. *Phys. Rev. B*, 73:172414, 2006.

[68] A. Y. Dobin and R. H. Victora. *Phys. Rev. Lett.*, 92:257204, 2004.

[69] A. Y. Dobin and R. H. Victora. *J. Appl. Phys.*, 95:7139, 2004.

[70] M. C. Hickey and J. S. Moodera. *Phys. Rev. Lett.*, 102:137601, 2009.

[71] J. Foros, A. Brataas, Y. Tserkovnyak, and G. E. W. Bauer. *Phys. Rev. Lett.*, 95:016601, 2005.

[72] J. Foros, A. Brataas, Y. Tserkovnyak, and G. E. W. Bauer. *Phys. Rev. B*, 78:140402, 2008.

[73] T. L. Gilbert. *Phys. Rev.*, 100:1243, 1955.

[74] J. C. Sankey, Y.-T. Cui, J. Z. Sun, J. C. Slonczewski, R. A. Buhrman, and D. C. Ralph. *Nat. Phys.*, 4:67, 2008.

[75] S. Zhang, P. M. Levy, and A. Fert. *Phys. Rev. Lett.*, 88:236601, 2002.

[76] H. Kubota, A. Fukushima, K. Yakushiji, T. Nagahama, S. Yuasa, K. Ando, H. Maehara, Y. Nagamine, K. Tsunekawa, D. D. Djayaprawira, N. Watanabe, and Y. Suzuki. *Nat. Phys.*, 4:37, 2008.

[77] I. Theodonis, N. Kioussis, A. Kalitsov, M. Chshiev, and W. H. Butler. *Phys. Rev. Lett.*, 97:237205, 2006.

[78] R. H. Koch, J. A. Katine, and J. Z. Sun. *Phys. Rev. Lett.*, 92:088302, 2004.

[79] S. Petit, C. Baraduc, C. Thirion, U. Ebels, Y. Liu, M. Li, P. Wang, and B. Dieny. *Phys. Rev. Lett.*, 98:077203, 2007.

[80] A. M. Deac, A. Fukushima, H. Kubota, H. Maehara, Y. Suzuki, S. Yuasa, Y. Nagamine, K. Tsunekawa, D. D. Djayaprawira, and N. Watanabe. *Nat. Phys.*, 4:803, 2008.

[81] W. F. Brown. *Phys. Rev.*, 130:1677, 1963.

[82] A. Kamenev. Cambridge University Press, 2011.

[83] J. Swiebodzinski, A. Chudnovskiy, T. Dunn, and A. Kamenev. *Phys. Rev. B.*, 82:144404, 2010.

[84] Makoto Matsumoto and Takuji Nishimura. *ACM Trans. Model. Comput. Simul.*, 8:3, 1998.

[85] G. Marsaglia. *Journal of Statistical Software*, 8:14, 2003.

[86] O. J. Lee, V. S. Pribiag, P. M. Braganca, P. G. Gowtham, D. C. Ralph, and R. A. Buhrman. *Appl. Phys. Lett.*, 95:012506, 2009.

[87] C. Papusoi, B. Delaët, B. Rodmacq, D. Houssameddine, J.-P. Michel, U. Ebels, R. C. Sousa, L. Buda-Prejbeanu, and B. Dieny. *Appl. Phys. Lett.*, 95:072506, 2009.

[88] H. Liu, D. Bedau, D. Backes, J. A. Katine, J. Langer, and A. D. Kent. *Appl. Phys. Lett.*, 97:242510, 2010.

[89] G. E. Rowlands, T. Rahman, J. A. Katine, J. Langer, A. Lyle, H. Zhao, J. G. Alzate, A. A. Kovalev, Y. Tserkovnyak, Z. M. Zeng, H. W. Jiang, K. Galatsis, Y. M. Huai, P. Khalili Amiri, K. L. Wang, I. N. Krivorotov, and J.-P. Wang. *Appl. Phys. Lett.*, 98:102509, 2011.

[90] Y.-W. Liu and Z.-Z. Zhang. *Science China Physics, Mechanics and Astronomy*, 56:184, 2013.

[91] T. Dunn and A. Kamenev. *J. Appl. Phys.*, 112:103906, 2012.

[92] T. Dunn, A. Chudnovskiy, and A. Kamenev. *Dynamics of nano-magnetic oscillators*. 2012.

[93] M. I. Dykman and M. A. Krivoglaz. *JETP*, 50:30, 1979.

[94] D. M. Apalkov and P. B. Visscher. *Phys. Rev. B*, 72:180405(R), 2005.

[95] G. Bertotti. *Magnetic Nanostructures in Modern Technology*. Springer, xviii edition, 2008.

[96] T. Dunn and A. Kamenev. *Appl. Phys. Lett.*, 98:143109, 2011.

[97] T. Taniguchi, Y. Utsumi, M. Marthaler, D. S. Golubev, and H. Imamura. *Phys. Rev. B*, 87:054406, 2013.

[98] D. Pinna, A. D. Kent, and D. L. Stein. *Phys. Rev. B*, 88:104405, 2013.

[99] D. C. Worledge, G. Hu, D. W. Abraham, J. Z. Sun, P. L. Trouilloud, J. Nowak, S. Brown, M. C. Gaidis, E. J. OSullivan, and R. P. Robertazzi. *Appl. Phys. Lett.*, 98:022501, 2011.

[100] T. Taniguchi and H. Imamura. *Appl. Phys. Express*, 6:053002, 2013.

[101] I. N. Krivorotov, N. C. Emley, J. C. Sankey, S. I. Kiselev, D. C. Ralph, and R. A. Buhrman. *Science*, 307:228, 2005.

[102] Y.-T. Cui, G. Finocchio, C. Wang, J. A. Katine, R. A. Buhrman, and D. C. Ralph. *Phys. Rev. Lett.*, 104:097201, 2010.

[103] H. Zhao, A. Lyle, Y. Zhang, P. K. Amiri, G. Rowlands, Z. Zeng, J. Katine, H. Jiang, K. Galatsis, K. L. Wang, I. N. Krivorotov, and J.-P. Wang. *J. Appl. Phys.*, 109:07C720, 2011.

[104] A. Vaysset, C. Papusoi, L. D. Buda-Prejbeanu, S. Bandiera, M. Marins de Castro, Y. Dahmane, J.-C. Toussaint, U. Ebels, S. Auffret, R. Sousa, L. Vila, and B. Dieny. *Appl. Phys. Lett.*, 98:242511, 2011.

[105] A. Mejdoubi, B. Lacoste, G. Prenat, and B. Dieny. *Appl. Phys. Lett.*, 102:152413, 2013.

[106] A. Ruotolo, V. Cros, B. Georges, A. Dussaux, J. Grollier, S. Fusil, C. Deranlot, R. Guillemet, K. Bouzehouane, and A. Fert. *Nat. Nanotechnology*, 4:528, 2009.

[107] B. Georges, J. Grollier, V. Cros, A. Fert, A. Fukushima, H. Kubota, K. Yakushijin, S. Yuasa, and K. Ando. *App. Phys. Expr.*, 2:123003, 2009.

[108] C. Wang, Y.-T. Cui, J. Z. Sun, J. A. Katine, R. A. Buhrman, and D. C. Ralph. *J. Appl. Phys.*, 106:053905, 2009.

[109] X. Cheng, C. T. Boone, J. Zhu, and I. N. Krivorotov. *Phys. Rev. Lett.*, 105:047202, 2010.

[110] J. Zhu, J. A. Katine, G. E. Rowlands, Y.-J. Chen, Z. Duan, J. G. Alzate, P. Upadhyaya, J. Langer, P. K. Amiri, K. L. Wang, , and I. N. Krivorotov. *Phys. Rev. Lett.*, 108:197203, 2012.

[111] W. Skowroǹski, M. Czapkiewicz, M. Frankowski, J. Wrona, T. Stobiecki, G. Reiss, K. Chalapat, G. S. Paraoanu, and S. van Dijken. *Phys. Rev. B*, 87:094419, 2013.

[112] L. Fricke, S. Serrano-Guisan, and H. W. Schumacher. *Physica B*, 407:1153, 2012.

[113] X. Cheng, J. A. Katine, G. E. Rowlands, and I. N. Krivorotov. *Appl. Phys. Lett.*, 103:082402, 2013.

[114] G. Finocchio, G. Siracusano, V. Tiberkevich, I. N. Krivorotov, L. Torres, and B. Azzerboni. *Phys. Rev. B*, 83:134402, 2011.

[115] O. V. Prokopenko, I. N. Krivorotov, E. Bankowski, T. Meitzler, S. Jaroch, V. S. Tiberkevich, and A. N. Slavin. *J. Appl. Phys.*, 111:123904, 2012.

[116] S. H. Florez, J. A. Katine, M. Carey, L. Folks, O. Ozatay, and B. D. Terris. *Phys. Rev. B*, 78:184403, 2008.

[117] L. Xue, C. Wang, Y.-T. Cui, L. Liu, A. Swander, J. Z. Sun, R. A. Buhrman, , and D. C. Ralph. *Phys. Rev. Lett.*, 108:147201, 2012.

[118] M. Carpentieri, M. Ricci, P. Burrascano, L. Torres, and G. Finocchio. *J. Appl. Phys.*, 111:07C909, 2012.

[119] I. L. Prejbeanu, S. Bandiera, J. Alvarez-Hrault, R. C. Sousa, B Dieny, and J.-P. Nozires. *Phys. Rev. B*, 78:140402, 2008.

[120] N.G. van Kampen. *Magnetic Nanostructures in Modern Technology.* North-Holland Personal Library, 2nd edition, 2001.

[121] T. Taniguchi and H. Imamura. *Phys. Rev. B*, 83:054432, 2011.

[122] D. Pinna, A. D. Kent, and D. L. Stein. *ArXiv e-prints*, 2013, 1305.5945.

Appendix A

LLGS equation

A.1 Energy equation

This appendix shows how to represent the standard ferromagnetic energy equation in the form used in Eqn. (2.7). The energy of any free layer is typically written as

$$\begin{aligned} E(\mathbf{M}) &= -\frac{1}{2}H_{\mathrm{k}}M_{\mathrm{s}}\left(\mathbf{m}\cdot\hat{\mathbf{e}}_{\mathrm{x}}\right)^2 + \frac{1}{2}\mathbf{M}\cdot\mathbf{N}\cdot\mathbf{M} - \mathbf{M}\cdot\mathbf{H}_{\mathrm{ext}} \\ &= -\frac{1}{2}H_{\mathrm{k}}M_{\mathrm{s}}m_{\mathrm{x}}^2 + \frac{1}{2}M_{\mathrm{s}}^2\left(N_{\mathrm{xx}}m_{\mathrm{x}}^2 + N_{\mathrm{yy}}m_{\mathrm{y}}^2 + N_{\mathrm{zz}}m_{\mathrm{z}}^2\right) - \mathbf{M}\cdot\mathbf{H}_{\mathrm{ext}}\,, \end{aligned} \tag{A.1}$$

where $m_{\mathrm{i}} = \mathbf{m}\cdot\hat{\mathbf{e}}_{\mathrm{i}}$, $N_{\mathrm{ii}} = \hat{\mathbf{e}}_{\mathrm{i}}\cdot\mathbf{N}\cdot\hat{\mathbf{e}}_{\mathrm{i}}$ are the diagonal elements of the demagnetization matrix, and $\mathbf{H}_{\mathrm{k}}$ is the uniaxial crystaline anisotropy with easy-axis chosen along the $\hat{\mathbf{e}}_{\mathrm{x}}$-axis. Making the substitutions $N_{\mathrm{zz}} = N_{\mathrm{yy}} + H_{\mathrm{z}}$ and $N_{\mathrm{xx}} = N_{\mathrm{yy}} - H'_{\mathrm{x}}$ gives

$$E(\mathbf{m}) = \frac{1}{2}M_{\mathrm{s}}\left[H_{\mathrm{z}}m_{\mathrm{x}}^2 + N_{\mathrm{yy}} - \left(H_{\mathrm{k}} + H'_{\mathrm{x}}\right)m_{\mathrm{z}}^2 - \mathbf{H}_{\mathrm{ext}}\cdot\mathbf{m}\right]\,. \tag{A.2}$$

Letting $H_{\mathrm{x}} = H'_{\mathrm{x}} + H_{\mathrm{k}}$ and dropping the constant energy term $N_{\mathrm{yy}}M_{\mathrm{s}}^2/2$ gives Eqn. (2.7).

A.2 Conservation of M_{s}

The conservation of the magnetization magnitude under via the LLGS Eqn. (2.1) is shown here. Taking the scalar product $\mathbf{M}\cdot\dot{\mathbf{m}}$ gives

$$\mathbf{M}\cdot\dot{\mathbf{M}} = -\gamma\mathbf{M}\cdot\left[\mathbf{M}\times\mathbf{H}_{\mathrm{eff}}\right] + \frac{\alpha}{M_{\mathrm{s}}}\mathbf{M}\cdot\left[\mathbf{M}\times\dot{\mathbf{M}}\right] + \gamma\frac{\mathcal{I}_{\mathrm{s}}}{M_{\mathrm{s}}^2}\mathbf{M}\cdot\left[\mathbf{M}\times\left[\mathbf{m}_{\mathrm{p}}\times\mathbf{M}\right]\right]\,. \tag{A.3}$$

The first two terms vanish upon permutation of the scalar triple product leaving

$$\begin{aligned}\mathbf{M}\cdot\dot{\mathbf{m}} &= \gamma\frac{\mathcal{I}_\mathrm{s}}{M_\mathrm{s}^2}\mathbf{M}\cdot[\mathbf{M}\times[\mathbf{m}_\mathrm{p}\times\mathbf{M}]] = \gamma\frac{\mathcal{I}_\mathrm{s}}{M_\mathrm{s}^2}\mathbf{M}\cdot\left[\mathbf{m}_\mathrm{p}M_\mathrm{s}^2-\mathbf{M}\left(\mathbf{m}_\mathrm{p}\cdot\mathbf{M}\right)\right]\\ &= \gamma\mathcal{I}_\mathrm{s}\left(\mathbf{m}_\mathrm{p}\cdot\mathbf{M}-\mathbf{m}_\mathrm{p}\cdot\mathbf{M}\right)=0\,;\end{aligned} \tag{A.4}$$

thus the LLGS equation preserves M_s.

A.3 Landau-Lifshitz damping

This appendix shows a more detailed derivation of the LLGS equation presented in chapter 2. The full LLGS equation is

$$\dot{\mathbf{M}} = -\gamma\left[\mathbf{M}\times\mathbf{H}_\mathrm{eff}\right]+\frac{\alpha}{M_\mathrm{s}}\left[\mathbf{M}\times\dot{\mathbf{M}}\right]+\gamma\frac{\mathcal{I}_\mathrm{s}}{M_\mathrm{s}}\left[\mathbf{M}\times[\mathbf{m}_\mathrm{p}\times\mathbf{M}]\right]\,. \tag{A.5}$$

Taking the cross product of $\mathbf{M}\times\dot{\mathbf{M}}$ gives

$$\mathbf{M}\times\dot{\mathbf{M}} = -\gamma\mathbf{M}\times[\mathbf{M}\times\mathbf{H}_\mathrm{eff}]-\alpha M_\mathrm{s}\dot{\mathbf{M}}+\gamma\mathcal{I}_\mathrm{s}M_\mathrm{s}\left[\mathbf{M}\times\mathbf{m}_\mathrm{p}\right]\,. \tag{A.6}$$

Substituting this back into Eqn. (A.5) gives

$$\begin{aligned}(1+\alpha^2)\dot{\mathbf{M}} = &-\gamma\left[\mathbf{M}\times\mathbf{H}_\mathrm{eff}\right]-\alpha\frac{\gamma}{M_\mathrm{s}}\mathbf{M}\times[\mathbf{M}\times\mathbf{H}_\mathrm{eff}]+\gamma\frac{\mathcal{I}_\mathrm{s}}{M_\mathrm{s}}\left[\mathbf{M}\times[\mathbf{m}_\mathrm{p}\times\mathbf{M}]\right]\\ &+\gamma\alpha\mathcal{I}_\mathrm{s}\left[\mathbf{M}\times\mathbf{m}_\mathrm{p}\right]\,.\end{aligned} \tag{A.7}$$

Substituting $\gamma' = \gamma/(1+\alpha^2)$ gives the form of the LLGS equation discussed in chapter 2 and used in the numerical simulations throughout this thesis. The second "field like" torque term takes the same form as the effective field, and thus the LL torque can be written as

$$\mathbf{\Gamma}_\mathrm{LL} = -\gamma\left[\mathbf{M}\times\left[\mathbf{H}_\mathrm{eff}-\alpha\,\mathcal{I}_\mathrm{s}\mathbf{m}_\mathrm{p}\right]\right]\,. \tag{A.8}$$

For $\alpha\mathcal{I}_\mathrm{s}\ll H_\mathrm{eff}$ this "field like" term can be ignored.

Appendix B

Energy/angle equations

This appendix puts the energy/angle equations of motion from chapter 3 into a more transparent context. It also provides a more detailed calculation of the approximate values for the effective forces shown in chapter 4.

B.1 Full equations

The energy density of the free layer from Eqn. (2.7) can be expressed in spherical coordinates

$$E = \frac{M_\mathrm{s}}{2}\left(H_\mathrm{x}\sin^2\theta + H_\mathrm{z}\sin^2\theta\cos^2\psi\right) = \frac{H_\mathrm{x}M_\mathrm{s}}{2}\sin^2\theta\left(1 + h\cos^2\psi\right)\,, \tag{B.1}$$

where θ is the polar angle relative to the easy-axis and ψ is the azimuthal angle about the easy-axis measured from the $\hat{\mathbf{e}}_\mathrm{z}$ axis. The effective field in these coordinates is

$$\mathbf{H}_\mathrm{eff} = -H_\mathrm{x}\sin\theta\left(\cos\theta A(\psi)\hat{\theta} - B(\psi)\hat{\psi}\right)\,, \tag{B.2}$$

where the shorthand

$$A(\psi) = 1 + h\cos^2\psi\,; \qquad B(\psi) = h\cos\psi\sin\psi\,, \tag{B.3}$$

is used, with $h = H_\mathrm{z}/H_\mathrm{x}$, and where

$$\sin\theta = \sqrt{\frac{E/E_\mathrm{b}}{A(\psi)}}\,; \qquad \cos\theta = \pm\sqrt{\frac{A(\psi) - E/E_\mathrm{b}}{A(\psi)}}\,, \tag{B.4}$$

from Eqn. (B.1) and $E_\mathrm{b} = M_\mathrm{s}H_\mathrm{x}/2$.

In this notation, the conservative LL torque given by Eqn. (2.5) is

$$\mathbf{\Gamma}_\mathrm{LL} = -\gamma\mathbf{M}\times\mathbf{H}_\mathrm{eff} = \gamma M_\mathrm{s}H_\mathrm{x}\sin\theta\left(B(\psi)\hat{\theta} + A(\psi)\cos\theta\hat{\psi}\right) . \tag{B.5}$$

The infinitesimal magnetic "distance" covered by the magnetization as it precesses about the SW orbit with energy E is

$$\begin{aligned} dM =& M_\mathrm{s}\sqrt{\sin^2\theta d\psi^2 + d\theta^2} = d\psi M_\mathrm{s}\sqrt{\sin^2\theta + \left(\frac{d\theta}{d\psi}\right)^2} \\ =& \frac{|\mathbf{\Gamma}_\mathrm{LL}|}{\gamma H_\mathrm{x}A(\psi)\cos\theta}d\psi\,, \end{aligned} \tag{B.6}$$

with a corresponding integration vector

$$d\mathbf{M} = \frac{\mathbf{\Gamma}_\mathrm{LL}}{|\mathbf{\Gamma}_\mathrm{LL}|}dM = \frac{\mathbf{\Gamma}_\mathrm{LL}}{\gamma H_\mathrm{x}A(\psi)\cos\theta}d\psi\,. \tag{B.7}$$

Using Eqs. (B.5) and (B.7), the angle variable φ can be calculated as

$$\varphi(E,\psi) = \frac{2\pi}{P(E)}\int_0^\psi \frac{d\psi'}{\gamma H_\mathrm{x}A(\psi')\cos\theta}\,. \tag{B.8}$$

From this, the period of the SW orbit with energy E in the absence of ST and damping is

$$P(E) = \oint \frac{\mathbf{\Gamma}_\mathrm{LL}\cdot d\mathbf{M}}{|\mathbf{\Gamma}_\mathrm{LL}|^2} = \oint \frac{d\psi}{\gamma H_\mathrm{x}A(\psi)\cos\theta}\,. \tag{B.9}$$

Note, for SW orbits with $E < E_\mathrm{b}$ and $\theta > \pi/2$ the magnetization precesses in the $-\psi$ direction; thus the negative sign from the $\cos\theta$ term is canceled by the change change in the limits of integration, i.e., $[0, 2\pi] \to [2\pi, 0]$.

The φ-averaged generalized forces are now calculated for SW orbits with $E < E_\mathrm{b}$ (for SW orbits with $E > E_\mathrm{b}$, spherical coordinates relative to the easy-plane axis should be used instead). The generalized damping force acting on the energy, given by Eqn. (3.9), takes the form

$$\begin{aligned} U(E) &= \frac{1}{M_\mathrm{s}P(E)}\oint [d\mathbf{M}\times\mathbf{H}_\mathrm{eff}]\cdot\mathbf{M} \\ &= \frac{2E}{P(E)}\oint \frac{B^2(\psi) + A^2(\psi)\cos^2\theta}{A^2(\psi)\cos\theta}d\psi\,. \end{aligned} \tag{B.10}$$

The generalized DC ST force acting on the energy, given by Eqn. 3.9, can be calculated similarly

$$\begin{aligned}\overline{V}_{\mathrm{x}}(E) &= \frac{\eta_{\mathrm{x}}}{M_{\mathrm{s}}P(E)}\oint[\mathbf{M}\times d\mathbf{M}]\cdot\hat{\mathbf{e}}_{\mathrm{x}} = \frac{2\eta_{\mathrm{x}}E}{H_{\mathrm{x}}P(E)}\oint\frac{d\psi}{A(\psi)}\\ &= \frac{4\pi\eta_{\mathrm{x}}E}{H_{\mathrm{x}}P(E)\sqrt{h+1}}\,,\end{aligned} \tag{B.11}$$

as can the generalized AC ST force acting on the energy, given by Eqn. (4.4),

$$\begin{aligned}\widetilde{V}_{\mathrm{z}}(E) &= \frac{\eta_{\mathrm{z}}}{M_{\mathrm{s}}P(E)}\oint[d\mathbf{M}\times\mathbf{M}]\cdot\hat{\mathbf{e}}_{\mathrm{z}}\cos\varphi\\ &= \frac{\eta_{\mathrm{z}}M_{\mathrm{s}}}{P(E)}\left(1+h-\frac{E}{E_{\mathrm{b}}}\right)\oint d\psi\frac{\sin\theta\cos\psi\cos\varphi}{A(\psi)\cos\theta}\,.\end{aligned} \tag{B.12}$$

The generalized forces acting on the angle φ may now be calculated as well. The generalized precessional force from the LL torque, given by Eqn. (3.1), is

$$\Omega(E) = \frac{2\pi}{P(E)}\,, \tag{B.13}$$

where $P(E)$ is the precessional period given by Eqn. (B.9). Finally, the generalized AC ST force acting on φ, given by Eqn. (4.5), is

$$\begin{aligned}\widetilde{W}_{\mathrm{z}}(E) &= -\frac{2\pi\eta_{\mathrm{z}}\gamma M_{\mathrm{s}}}{P^2(E)}\oint\frac{d\mathbf{M}\cdot\hat{\mathbf{e}}_{\mathrm{z}}}{|\mathbf{\Gamma}_{\mathrm{LL}}|^2}\sin\varphi\\ &= -\frac{2\pi\eta_{\mathrm{z}}M_{\mathrm{s}}}{H_{\mathrm{x}}P^2(E)}\oint\frac{d\psi}{A(\psi)\cos\theta}\frac{\mathbf{\Gamma}_{\mathrm{LL}}\cdot\hat{\mathbf{e}}_{\mathrm{z}}}{|\mathbf{\Gamma}_{\mathrm{LL}}|^2}\sin\varphi\\ &= \frac{2\pi\eta_{\mathrm{z}}}{\gamma H_{\mathrm{x}}^2P^2(E)}\left(\frac{E_{\mathrm{b}}}{E}\right)^{1/2}\oint\frac{d\psi}{\sqrt{A(\psi)}}\frac{\sin\psi\sin\varphi}{B^2(\psi)+A^2(\psi)\cos^2\theta}\,.\end{aligned} \tag{B.14}$$

B.2 Approximations

The energy density for the free layer given by Eqn. (2.7), written in spherical coordinates and expanded to second order in θ for $\theta \ll 1$, gives

$$E \approx E_{\mathrm{b}}\theta^2A(\psi)\,, \tag{B.15}$$

where $A(\psi)$ is given by Eqn. (B.3). Expanding the period to second order in θ and using Eqn. (B.15) gives

$$P(E) \approx \oint\frac{d\psi}{\gamma H_{\mathrm{x}}A(\psi)}\left(1+\frac{\theta^2}{2}\right) = \frac{2\pi}{\gamma H_{\mathrm{x}}\sqrt{1+h}}\left(1+\frac{E}{E_{\mathrm{b}}}\frac{h+2}{4h+4}\right)\,. \tag{B.16}$$

The corresponding frequency is therefore

$$\Omega(E) \approx \frac{2\pi}{\gamma H_{\mathrm{x}}\sqrt{1+h}}\left(1-\frac{E}{E_{\mathrm{b}}}\frac{h+2}{4h+4}\right). \tag{B.17}$$

Ignoring the term of order $\mathcal{O}(\theta^2)$, the angle φ may be expressed as

$$\varphi(\psi) \approx \frac{2\pi}{P(E)}\int_0^{\psi}\frac{d\psi'}{\gamma H_{\mathrm{x}}A(\psi')} = \tan^{-1}\left(\frac{\tan\psi}{\sqrt{1+h}}\right), \tag{B.18}$$

where ψ is the standard polar angle about the easy-axis. This gives

$$\sin\varphi \approx \sqrt{\frac{1}{A(\psi)}}\sin\psi\,; \qquad \cos\varphi \approx \sqrt{\frac{1+h}{A(\psi)}}\cos\psi\,. \tag{B.19}$$

For the φ-averaged generalized forces, the damping force acting on the energy $U(E)$ expanded to second order in θ is given by

$$\begin{aligned} U(E) &\approx \frac{2E}{P(E)}\oint\frac{A^2(\psi)+B^2(\psi)}{A^2(\psi)}d\psi \\ &= \frac{\gamma H_{\mathrm{x}}\sqrt{1+h}}{\pi}E\oint\frac{A^2(\psi)+B^2(\psi)}{A^2(\psi)}d\psi \\ &= \gamma H_{\mathrm{x}}(2+h)E\,. \end{aligned} \tag{B.20}$$

The generalized DC ST force acting on the energy is

$$\overline{V}_{\mathrm{x}}(E) \approx 2\eta_{\mathrm{x}}\gamma E\,. \tag{B.21}$$

The generalized AC ST force acting on the energy expanded to leading order in θ is

$$\begin{aligned} \widetilde{V}_{\mathrm{z}}(E) &\approx \frac{\eta_{\mathrm{z}}M_{\mathrm{s}}(h+1)}{P(E)}\oint\frac{\theta\cos\psi\cos\varphi}{A(\psi)}d\psi \\ &= \frac{\eta_{\mathrm{z}}\gamma H_{\mathrm{x}}M_{\mathrm{s}}\eta_{\mathrm{z}}(1+h)^2}{2\pi}\sqrt{\frac{E}{E_{\mathrm{b}}}}\oint\frac{\cos^2\psi}{A^2(\psi)} \\ &= \eta_{\mathrm{z}}\gamma E_{\mathrm{b}}\sqrt{1+h}\sqrt{\frac{E}{E_{\mathrm{b}}}}\,, \end{aligned} \tag{B.22}$$

Finally, the generalized AC ST force acting on the phase ϕ, expanded to first order in θ^{-1}, is

$$\begin{aligned} \widetilde{W}_{\mathrm{z}}(E) &\approx \frac{2\pi\eta_{\mathrm{z}}}{\gamma H_{\mathrm{x}}^2P^2(E)}\left(\frac{E_{\mathrm{b}}}{E}\right)^{1/2}\oint\frac{d\psi}{\sqrt{A(\psi)}}\frac{\sin\psi\sin\varphi}{B^2(\psi)+A^2(\psi)} \\ &= \frac{\eta_{\mathrm{z}}\gamma(1+h)}{2\pi}\left(\frac{E_{\mathrm{b}}}{E}\right)^{1/2}\oint d\psi\frac{\sin^2\psi}{A(\psi)\left(B^2(\psi)+A^2(\psi)\right)} \\ &= \gamma\left(1+h-\sqrt{1+h}\right)\frac{\eta_{\mathrm{z}}}{h}\sqrt{\frac{E_{\mathrm{b}}}{E}}\,. \end{aligned} \tag{B.23}$$

B.3 Upper and lower critical current

The local critical current $\mathcal{I}_{\rm c}(E)$ is given by Eqn. (3.11). For the lower critical current when $E \ll E_{\rm b}$, the generalized φ-averaged damping and DC ST are

$$U(E) = \gamma H_{\rm x}(2+h)E; \qquad \overline{V}_{\rm x}(E) = 2\eta_{\rm x}\gamma E\,. \tag{B.24}$$

Plugging these into Eqn. (3.11) for the DC critical spin-current, the energy dependence vanishes; thus

$$\mathcal{I}_{\rm c}(0) = \alpha H_{\rm x}\frac{2+h}{2\eta_{\rm x}}\,. \tag{B.25}$$

For the upper critical current when $E \simeq E_{\rm b}$, the generalized φ-averaged damping is given by

$$\begin{aligned} U(E) &= \frac{2E}{P(E)}\oint \frac{B^2(\psi)+A^2(\psi)\cos^2\theta}{A^2(\psi)\cos\theta}d\psi \\ &= \frac{2E}{P(E)}\oint \frac{B^2(\psi)+A^2(\psi)-A(\psi)}{A(\psi)\left(A^2(\psi)-A(\psi)\right)}d\psi \\ &= \frac{8E\sqrt{h}}{P(E)}\,. \end{aligned} \tag{B.26}$$

The φ-averaged DC ST force is

$$\overline{V}_{\rm x} = \frac{4\pi\eta_{\rm x}E}{H_{\rm x}P(E)\sqrt{h+1}}\,, \tag{B.27}$$

c.f. Eqn. (B.11). Plugging these into Eqn. (3.11) gives

$$\mathcal{I}_{\rm c}(E_{\rm b}) = \alpha\frac{2H_{\rm x}\sqrt{h(h+1)}}{\pi\eta_{\rm x}}\,. \tag{B.28}$$

Appendix C

Glossary and acronyms

Care has been taken in this thesis to minimize the use of jargon and acronyms, but this cannot always be achieved. This appendix contains a table of acronyms and their meanings.

C.1 Glossary

- **Critical Current** ($\mathcal{I}_c$) – Minimum spin-current needed to switch the free layer. Defined by Eqn. (3.13) for DC spin-currents and by Eqn. (4.12) for AC spin-currents.
- **Easy-Axis Field** ($\mathbf{H}_x$) – Effective magnetic field along the easy-axis direction resulting from crystaline anisotropy and the demagnetizing field.
- **Easy-Axis Vector** ($\hat{\mathbf{e}}_x$) – Unit vector parallel to the easy-axis direction.
- **Easy-Plane Field** ($\mathbf{H}_z$) – Effective magnetic field normal to the easy-plane resulting from crystaline anisotropy and the demagnetizing field.
- **Easy-Plane Vector** ($\hat{\mathbf{e}}_z$) – Unit vector perpendicular to the easy-plane.
- **Effective Magnetic Field** ($\mathbf{H}_{\text{eff}}$) – Net effective field acting on the free layer. Defined by Eqn. (2.6).
- **Energy Density** (E) – Magnetostatic energy density of the free layer. Defined by Eqn. (2.7).

- **External Field** ($\mathbf{H}_{\text{ext}}$) – Applied external field acting on the free layer.
- **Gilbert Damping Constant** (α) – Phenomenological dimensionless constant proportional to the rate of energy loss by the free layer.
- **Gilbert Damping Torque** ($\mathbf{\Gamma}_{\text{GD}}$) – Dissipative torque acting on the free layer magnetization. Defined by Eqs. (2.8) and by (2.9) when $\alpha \ll 1$.
- **Gyromagnetic Ratio** (γ) – Conversion factor between angular momentum and magnetic moment.
- **Hard-Axis Vector** ($\hat{\mathbf{e}}_{\text{y}}$) – Unit vector parallel to the hard-axis in the easy-plane.
- **Joule Heat Loss** (JHL) – Energy dissipated via Joule heating during the switching process.
- **Local Critical Current** ($\mathcal{I}_{\text{c}}(E)$) – Spin-current needed to exactly cancel effect of damping. Defined by Eqn. (3.11) for DC spin-currents and by Eqn. (4.18) for AC spin-currents.
- **Landau-Lifshitz Torque** ($\mathbf{\Gamma}_{\text{LL}}$) – Conservative torque acting on the free layer magnetization. Defined by Eqs. (2.5).
- **Magnetization Vector** ($\mathbf{M}$) – Vector describing the magnetization of the free layer.
- **Polarization Vector** ($\mathbf{m}_{\text{p}}$) – Unit vector pointing along the direction of the spin-current polarization.
- **Saturation Magnetization** (M_{s}) – Magnitude of the free layer magnetization.
- **Spin-Conductance** ($G_{\sigma,\sigma'}$) – Conductance of electrons with spin σ via the σ' conduction channel.
- **Spin-Current Vector** ($\vec{\mathcal{I}}_{\text{s}}$) – Effective magnetization of the spin-current. Proportional to the current density and the spin-polarization constant.
- **Spin-Current Strength** ($\mathcal{I}_{\text{s}}$) – Effective magnetic moment of the spin-current. Proportional to the current density and the spin-polarization constant. Defined by Eqn. (2.11).

- **Spin-Torque** ($\mathbf{\Gamma}_{\mathrm{ST}}$) – Torque on the free layer resulting from the transfer of angular momentum from a spin-current to the free layer. Defined by Eqn. (2.10).
- **Stochastic Field** ($\mathbf{h}(t)$) – Magnetic field with random strength and Gaussian distribution. Defined by correlator given by Eqn. (2.19).
- **Switching Time** (t_{sw}) – Time required to reverse the magnetization of the free layer for a given current pulse protocol.

C.2 Acronyms

Table C.1: Acronyms

Acronym	Meaning
AC	Alternating Current
DC	Direct Current
JHL	Joule Heat Loss
LHS	Left Hand Side
LLGS	Landau-Lifshitz-Gilbert-Slonczewski Equation
MTJ	Magnetic Tunnel Junction
RHS	Right Hand Side
SAF	Synthetic Antiferromagnet
ST	Spin-Torque
STO	Spin-Torque Oscillator
SV	Spin-Valve
SW	Stoner Wohlfarth